EXPERIMENTAL INVESTIGATION OF PULSED ELECTRICAL DISCHARGE ENERGY DEPOSITION IN SUPERSONIC FLOWS

A Thesis

by

NICHOLAS ADAM GAWLOSKI

Submitted to the Office of Graduate and Professional Studies of
Texas A&M University
in partial fulfillment of the requirements for the degree of

MASTER OF SCIENCE

Chair of Committee,	David Staack
Committee Members,	Waruna Kulatilaka
	Nathan Tichenor
Head of Department,	Andreas A. Polycarpou

May 2017

Major Subject: Mechanical Engineering

ABSTRACT

Energy deposition in the form of a direct current spark discharge in Mach 2.2 flow is experimentally investigated, to measure the conversion efficiency of electrical energy into thermal energy. The energy is impulsively deposited into to the flow. This impulsive deposition occurs much faster than the flow can react, creating a strong blast wave and a high temperature, high pressure region in the flow. The plasma discharge is created between two sharpened tungsten electrodes inclined into the flow, powered by a pulsing high voltage RC circuit. Schlieren imagery was utilized to track the expansion of the blast wave and the expansion of the high temperature, high pressure region created by the spark discharge into a low density region.

To estimate the conversion efficiency of electrical energy into the thermal energy in the flow, a high temperature thermodynamic heating and expansion model was developed to simulate the deposition process. The model consisted of two portions. First, the thermodynamic properties of N_2, O_2, N, O, Ar, were calculated from the NASA PAC database, valid for temperatures 200-20,000K. A high temperature air mixture was then constructed from the five species assuming chemical equilibrium for temperature from 200-20,000K. Second, a heating and expansion model was developed utilizing the high temperature air properties. The energy deposition was modeled as a constant volume heating process to simulate its impulsive nature. The initial volume of the plasma is calculated from direct imaging of the discharge at delays ranging from 80-120ns. The resulting high temperature, high pressure region is then mixed with varying amounts of ambient air to simulate heat transfer. The high temperature region is then expanded

isentropically back to ambient pressure, where the final volume was compared to the experimental Schlieren images to estimate the conversion efficiency.

Three different capacitors were used during experimentation to vary the input electrical energy three orders of magnitude; specifically, the energies were calculated to be: 3.4, 20.8 and 203mJ per pulse. The range of possible efficiencies for the three cases was found to be: 70-90%, 14-30%, and 5-12%. The lower energy case was found to be the most efficient with regards to energy conversion. However, the largest energy case was found to be more effective because it resulted in the region with the highest expanded temperature (4150K) and lowest expanded density (0.017 [kg m^{-3}]) in its final expanded state.

ACKNOWLEDGEMENTS

First I would like to express my sincerest gratitude and appreciation to my graduate advisor, Dr. David Staack. His enthusiasm and expert knowledge in plasma science motivated me to pursue this research. If it were not for Dr. Staack I would have never even become a Mechanical Engineer, and for that I am eternally grateful.

Second, I would like to thank Dr. Rodney Bowersox and all his students and staff at the NAL. I would also like to personally thank Ian Neel, Shanae Smith and Andrew Leidy for all the time they invested helping me operate the SHR wind tunnel.

I would also like to thank my committee members, Dr. Nathan Tichenor and Dr. Waruna Kulatilaka, for their guidance and support throughout this research.

Furthermore, I would like to thank Dr. Kevin Kremeyer and PM&AM Research for the support and assistance they provided throughout my research.

CONTRIBUTORS AND FUNDING SOURCES

Contributors

This work was supervised by a thesis committee consisting of Dr. David Staack [advisor] and Dr. Waruna Kulatilaka of the Department of Mechanical Engineering and Dr. Nathan Tichenor of the Department of Aerospace Engineering

All work for the thesis was completed by Nicholas Gawloski.

Funding Sources

This work was partially supported by Physics Materials and Applied Mathematics Research LLC under NASA SBIR contract NNX14CL13C. Its contents are solely the responsibility of the author and do not necessarily represent the official views of NASA or PM&AM.

NOMENCLATURE

SHR	Supersonic High Reynolds number (1.2)
NAL	National Aerothermochemistry and Hypersonic Laboratory (1.2)
E_{trans}	Translational Kinetic Energy (2.1.1)
E_{rot}	Rotational Energy (2.1.1)
E_{vib}	Vibrational Energy (2.1.1)
E_{ele}	Electronic Energy (2.1.1)
E_{tot}	Total Molecular/Atomic Energy (2.1.1)
T_{gas}	Bulk Gas Temperature (2.1.2)
T_e	Electron Temperature (2.1.2)
T_{ele}	Electronic Temperature of Molecule or Atom (2.1.2)
T_{vib}	Vibrational Temperature of Molecule (2.1.2)
T_{rot}	Rotational Temperature of Molecule (2.1.2)
T_{trans}	Translational Temperature of Molecule or Atom (2.1.2)
V_b	Breakdown Voltage (2.1.2)
C	Capacitor (2.1.2)
n	Refractive Index (2.4)
ICCD	Intensified Charge-Coupled Device (3.1)
L_D	Discharge Gap Length (3.1.1)
Rb	Ballast Resistor (3.1.2)
τ	RC Time Constant (3.1.2)
Rs	Shunt Resistor (3.1.2)

V_A	Voltage across Spark Actuator (3.1.2)
EMI	Electromagnetic Interference (3.2.3)
ρ	Density (3.3.2)
V	Velocity (3.3.2)
A	Cross-Sectional Area (3.3.2)
$\dot{m}$	Mass Flow Rate (3.3.2)
a	Speed of Sound (3.3.2)
γ	Ratio of Specific Heats
T_s	Static Temperature in SHR Test Section (3.3.2)
Ps	Static Pressure in SHR Test Section (3.3.2)
PAC	NASA Glenn computer program for Properties and Coefficients (4.1)
E/n	Reduced Electric Field (4.2.1)
ν	Collision Frequency (4.2.1)
k	Rate Constant (4.2.1)
$\overline{C_p}$	Molar Specific Heat at Constant Pressure (4.2.2)
$\bar{h}$	Molar Enthalpy (4.2.2)
$\overline{s^o}$	Reference Molar Entropy (4.2.2)
$\overline{C_v}$	Molar Specific Heat at Constant Volume (4.2.2)
Ec	Stored Electrical Energy in Capacitor (4.3.2)
E_{in}	Percentage of E_c Converted into Thermal Energy in the Flow (4.3.2)
η	Efficiency of Spark Actuator (4.3.2)
BER	Bubble Expansion Ratio (4.3.2)

TABLE OF CONTENTS

Page

ABSTRACT ii

ACKNOWLEDGEMENTS iv

CONTRIBUTORS AND FUNDING SOURCES v

NOMENCLATURE vi

TABLE OF CONTENTS viii

LIST OF FIGURES x

LIST OF TABLES xiv

1. INTRODUCTION 1

1.1 Background & Motivation 1
1.2 Objective 2
1.3 Thesis Overview 3

2. BACKGROUND AND LITERATURE REVIEW 6

2.1 Plasma 6
2.1.1 Energy Storage Modes 7
2.1.2 Plasma Discharges 11
2.2 Energy Deposition 16
2.2.1 Deposition Techniques 17
2.2.2 Applications of Energy Deposition 18
2.3 Schlieren Imagery 21

3. EXPERIMENTAL SETUP 24

3.1 Experimental Setup 24
3.1.1 Spark Actuator 24
3.1.2 Electrical Circuit & Diagnostics Setup 27
3.2 Imaging Setup 30
3.2.1 Schlieren Hardware Setup 31
3.2.2 Plasma Light Filter 33
3.2.3 ICCD Direct Imaging Setup 35
3.3 National Aerothermochemistry and Hypersonics Laboratory 37
3.3.1 Supersonic High Reynolds Number Wind Tunnel 38

3.3.2 SHR Flow Properties 40
3.3.3 Wind Tunnel Infrastructure 42

4. ENERGY DEPOSITION MODEL 43

4.1 Model Overview 43
4.2 Thermodynamic Properties Model 44
4.2.1 Energy Transfer and Thermal Equilibration 44
4.2.2 NASA Glenn PAC Database 47
4.2.3 Chemical Equilibrium 48
4.2.4 Thermodynamic Properties of High Temperature Air 52
4.3 Thermodynamic Process Model 55
4.3.1 Simplified Process Model 55
4.3.2 Full Thermodynamic Process Model 58

5. RESULTS 63

5.1 Experimental Results 63
5.1.1 Electrical Energy Results 63
5.1.2 Discharge Volume Results 67
5.1.3 Schlieren Images 69
5.2 Thermodynamic Process Model Results 75
5.2.1 Model Results for C=100pF 76
5.2.2 Model Results for C=1,000pF 80
5.2.3 Model Results for C=10,000pF 84
5.2.4 Results Overview 90

6. CONCLUSIONS 92

6.1 Summary of Work Done 92
6.2 Summary of Findings 93
6.3 Concluding Remarks 96
6.4 Future Work 97

REFERENCES 99

APPENDIX 106

A.1. MATLAB code 106
A.1.1. Thermodynamic Properties Code 106
A.1.2. Thermodynamic Properties Code 109
A.2. Schlieren images 116
A.2.1. Images for C=100pF 116
A.2.2. Images for C=1000pF 119
A.2.3. Images for C=10000pF 120

LIST OF FIGURES

Page

Figure 1. Plasma, 4th state of matter. 7

Figure 2. Molecular energy modes. 10

Figure 3. Schematic of electric field plasma generation. 13

Figure 4. Current-voltage characteristic of an electric discharge. 15

Figure 5. RC circuit connected in parallel to air gap. 16

Figure 6. Light ray propagation in a schlieren imaging system. 22

Figure 7. Spark actuator installed inside the SHR tunnel. 24

Figure 8. CAD drawings of spark actuator: front view (top right), side view (top left), isometric view (bottom). 25

Figure 9. Schlieren image with undisturbed regions and discharge region. 26

Figure 10. Spark actuator in operation inside SHR tunnel, with C=1000pF. 27

Figure 11. Circuit schematic powering spark actuator. 28

Figure 12. North Star high voltage probe connection. 29

Figure 13. Current measurement setup. 30

Figure 14. Schlieren setup schematic. 32

Figure 15. Collimating portion of schlieren setup. 32

Figure 16. Knife edge and image capture portion of schlieren setup. 33

Figure 17. Schlieren image with portion obscured by plasma light. 34

Figure 18. Spectrum of plasma emission, LED emission, and filter transmittance. 35

Figure 19. ICCD camera setup, top view. 36

Figure 20. Background image with discharge region as shown in yellow in figure 8 (left); 10,000pF discharge overlaid on background (right). 37

Figure 21. Components of the SHR wind tunnel. 39

Figure 22. Fraction of energy transferred by electrons to energy modes of air. 46

Figure 23. Mole fractions of high temperature air. 51

Figure 24. Molar enthalpy of high temperature air and its five species. 53

Figure 25. Molar entropy of high temperature air and its five species. 53

Figure 26. Molar specific heats of the high temperature air mixture. 54

Figure 27. Specific gas constant of the high temperature air mixture. 54

Figure 28. T vs. v diagram for simplified thermodynamic process model, for C=100pF. 55

Figure 29. Temperature vs specific volume process diagram for entire process model. .58

Figure 30. Diagram of constant volume mixing process. 59

Figure 31. T vs. v diagram, two paths from state 2 to state 4, and approximate real process. 60

Figure 32. Efficiency vs BER with surface of possible solution for C=100pF, *k*=1-1.8. 62

Figure 33. V/I trace with calculated power and energy for C=179pF. 65

Figure 34. V/I trace with calculated power and energy for C=1,081pF. 65

Figure 35. V/I trace with calculated power and energy for C=10,560pF. 66

Figure 36. Plasma discharge for C=10,560pF, 5ns exposure at 100ns from discharge. ..67

Figure 37. Images of plasma discharge for C=10,560pF, 5ns exposure at 100ns from discharge. 68

Figure 38. Images of plasma discharge for C=1,081pF, 5ns exposure at 100ns from discharge. 68

Figure 39. Images of plasma discharge for C=179pF, 5ns exposure at 100ns from discharge. 68

Figure 40. Expanding region area calculation (individual image) for C=179pF, t_{delay}=25μs. 70

Figure 41. Area of expanding region as a function of time, for C=179pF. 71

Figure 42. Time evolution of expanding region (averaged images), for C=179pF.....71

Figure 43. Velocity of affected region for C=100pF.....72

Figure 44. Area of expanding region as a function of time, for C=1,081pF. 73

Figure 45. Area of expanding region as a function of time, for C=10,560pF. 74

Figure 46. Time evolution of expanding region (averaged images), for C=1,081pF(upper) and C=10,560(lower) 74

Figure 47. Surface of thermodynamically allowable solutions, with line of constant volume for C=179pF.....77

Figure 48. Tv process diagram for C=179pF at η_{12}=70%, *k*=1.64.....78

Figure 49. Tv process diagram for C=179pF at η_{12}=90%, *k*=1.02.....78

Figure 50. Tv process diagram for C=179pF at η_{12}=80%, *k*=1.31.....79

Figure 51. Surface of thermodynamically allowable solutions, with line of constant volume for C=1,081pF.....80

Figure 52. Tv process diagram for C=1,081pF at η_{12}=10%, *k*= 5.64.....81

Figure 53. Tv process diagram for C=1,081pF at η_{12}=27.5%, *k*=1.18.....82

Figure 54. Tv process diagram for C=1,081pF at η_{12}=22.5%, *k*=1.76.....83

Figure 55. Surface of thermodynamically allowable solutions, with line of constant volume for C=10,560pF.....85

Figure 56. Tv process diagram for C=10,560pF at η_{12}=12.5%, *k*=1.03.....85

Figure 57. Tv process diagram for C=10,560pF at η_{12}=3%, *k*=28.7.....87

Figure 58. Tv process diagram for C=10,560pF at η=8%, *k*=5.9. 88

Figure 59. Tv process diagram for C=10,560pF at η=9%, *k*=3.55. 88

Figure 60. Tv process diagram for C=10,560pF at η=10%, *k*=2.45. 89

Figure 61. Tv process diagram for C=10,560pF at η=11.5%, *k*=2.0. 89

Figure 62. Surface plot with reduced range of possible efficiencies for C=1,081pF.....91

Figure 63. Surface plot with range of possible efficiencies for C=10,560pF. 91

Figure 64. Range of final expanded temperatures for the three input energies.....95

Figure 65. Range of expansion ratios for the three input energies.....96

LIST OF TABLES

Page

Table 1. Maximum temperature and pressure encountered during calculation. 52

Table 2. Stored electrical energy calculated by method 2 using $V_{b,mean}$ 66

Table 3. Experimental parameters for process model, from experiment. 76

Table 4. State variables for C=179pf at η_{12}=80%, *k*=1.31. 79

Table 5. State variables for C=1081pF at η_{12}=22.5%, *k*=1.76. 83

Table 6. Properties for solutions corresponding to η_{12}=8 - 11.5% for C=10,560pF. 87

Table 7. State variables for C=10,560pF at η_{12}=11.5%, *k*=2.0. 90

Table 8. Summary of experimental data. 94

Table 9. Range of possible efficiencies. 94

Table 10. Effectiveness parameters. 95

1. INTRODUCTION

1.1 Background and Motivation

Aerodynamic efficiency is essential in energy-efficient flight in any regime especially supersonic flight. Minimizing drag is one of the fundamental characteristics of aerodynamic efficiency. The three types of drag that effect all aircraft regardless of the flight regime are viscous skin-friction drag, lift-induced drag, and form drag. Additionally, supersonic and transonic aircraft that produce shockwaves experience wave or compressibility drag as well. High drag significantly impacts the efficiency of the aircraft and therefore it is imperative to find innovative methods of drag reduction.

Over the past half century, about as long as the existence of supersonic aircraft, energy deposition has been recognized as an innovated method for a variety of flow control applications including drag reduction [1, 2, 3, 4, 5, 6]. Energy deposition relates to the rapid introduction of energy from an electrical source into a fluid flow generating a plasma, that is converted into thermal energy in the flow. Energy deposition can be initiated by many sources including: plasma arcs/sparks, laser pulses, microwaves, electron beam, glow discharges and RF discharges [1, 4, 6, 7, 8, 9]. One key feature of energy deposition separating it from conventional flow control methods is the short time scale of deposition, on the order of 10s of nanoseconds depending on the source. This extremely short timescale makes the deposition essentially instantaneous with regards to the flow, which reacts on the order of microseconds. The short time scale of energy deposition makes it a versatile flow control technique with numerous applications including drag reduction, in particular when deposited to create specific low-density

geometries [4, 5, 6]. Flow control applications for energy deposition include: drag reduction, lift enhancement, improved combustion, modification of shock structure, heat mitigation, etc. [1, 10, 11]. When this energy is applied continuously or sufficiently slowly to achieve gradual heating with subsonic expansion, its effects have been shown to be energetically inefficient and is commonly considered to only be useful in controlling slow, subsonic, flow [3].

1.2 Objective

All the energy deposition techniques are initiated with electrical energy, which is then directly deposited into the local flow or converted to another form of energy before being deposited into the local flow. The particular flow control application will determine how and where the local flow energy is converted or directed to the global flow. Therefore, the conversion efficiency of electrical energy from the circuit to the local flow is essential to all energy deposition techniques and their associated applications.

The objective of this research is to measure the conversion efficiency of electrical energy into thermal energy in a supersonic flow field during the energy deposition process. The electrical energy is stored in a DC charging RC circuit and released when breakdown of the air between the electrodes occurs creating a plasma. For this research the capacitances of the RC circuit used were 100pF, 1,000pF and 10,000pF, resulting in the electrical energy spanning three orders of magnitude from 2mJ to 200mJ. The energy deposition is implemented by a spark actuator consisting of two sharpened tungsten electrodes and mounted inside the Supersonic High Reynolds number (SHR) wind tunnel

located at the National Aerothermochemistry and Hypersonics Laboratory (NAL). The steps taken to measure the conversion efficiency of the spark actuator were:

- Design spark actuator and RC circuit to impulsively deposit energy to the flow and mount it inside the SHR wind tunnel.
- Measure the electrical energy stored in the RC circuit, which will be the total energy input used in the efficiency calculations.
- Measure the initial size of the plasma filament formed inside the discharge region.
- Measure the expansion of the blast wave and the high temperature, high pressure 'bubble like' region, created by the discharge to obtain expansion rates and the final expanded size for each input energy.
- Develop a high temperature thermodynamic model to capture the physics of the energy deposition process.
- Compare the model to the experimental measurements of the discharge and expanding regions to quantify the conversion efficiency as the ratio of stored energy in the circuit to the energy added to the gas in the flow.

1.3 Thesis Overview

Chapter 2 provides background relating to the physics of energy deposition. Including on overview of microscale thermodynamics, plasma physics, and schlieren imagery. A review of the energy deposition techniques and application in literature are examined to determine the proper effectiveness parameters.

Chapter 3 provides a detailed description of the experimental setup. Including the design and fabrication of the spark actuator, the design and assembly of the powering RC circuit and its diagnostic equipment, and the implementation of the two imaging setups. The section also includes a description of the SHR wind tunnel and its supporting infrastructure at the NAL.

Chapter 4 describes the two portions of the thermodynamic model implemented in MATLAB used to estimate the efficiency of the spark actuator. The first portion of the model calculates the thermodynamic properties of of N_2, O_2, N, O and Ar from the NASA PAC database. A high temperature air mixture was then constructed from the five species assuming chemical equilibrium for temperatures from 200-20,000K. The second portion of the model is a thermodynamic process model simulating the energy deposition process as a constant volume heating and subsequent expansion.

Chapter 5 provides a detailed description of the experimental and computational results, including:

- The average energy per pulse for each capacitor calculated from the measured capacitance and average breakdown voltage.
- The initial volume of the discharge measured from the direct imaging of the plasma filament.
- The final volume of the expanded region calculated from the schlieren images.
- The thermodynamic properties of the high temperature air mixture calculated from the first portion of the thermodynamic model.

Chapter 6 summarizes the findings of this research and provides concluding remarks concerning the efficiency and effectiveness of the energy deposition process, as well as provides suggestions for future work.

2. BACKGROUND AND LITERATURE REVIEW

2.1 Plasma

Plasma is the fourth state of matter. As more and more energy is added to a solid it eventually transforms into a liquid, as more energy is again added the liquid eventually transforms into a gas. As more and more energy is added the electrons surrounding the atoms and or molecules comprising the gas will be stripped away transforming it into a plasma, figure 1. A plasma is defined as a quasineutral mixture of neutral particles, positively charged ions and negatively charged electrons which exhibits collective behavior." [12]. The term quasineutral mean that the plasma has approximately equal number of ions as electrons i.e., the overall charge of a plasma is approximately zero. The term collective behavior means that the plasma motion depends not only on local conditions (collisions with other particles) but on the state of the plasma in remote regions as well. A plasma has enough charged particles that the motion of a single particle is determined by local conditions and by electromagnetic forces far away in the plasma. The best example of plasma is our Sun, an enormous sphere of plasma fueled by thermonuclear fusion at its core. Plasma is the most common form of matter comprising over 99% of known matter in the universe, since stars, nebulae, and most interstellar hydrogen is in a plasma state. Earth seems to be the exception, as naturally occurring plasmas are rare but can be found, for example during a lightning strike or the Aurora Borealis.

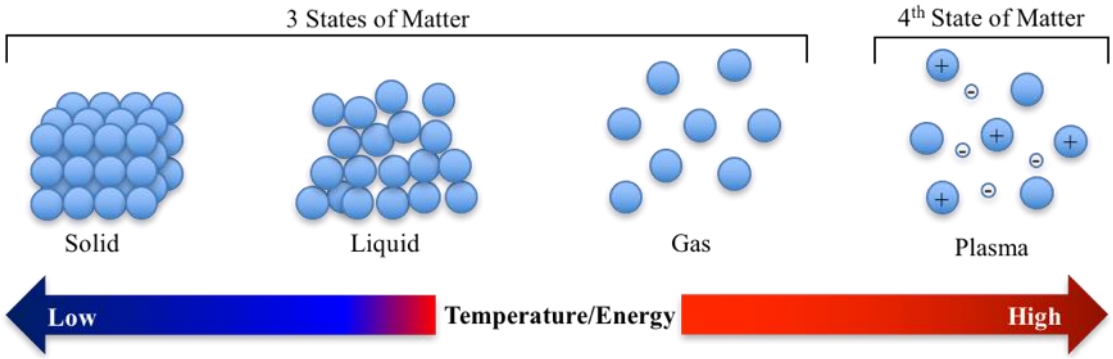

Figure 1. Plasma, 4th state of matter.

2.1.1 Energy Storage Modes

Classical thermodynamics describes a gas on the macroscopic level. The macroscopic description of a gas treats it as a continuous medium (bulk fluid), and not as discrete particles. The macroscopic quantities describe the observable properties of the gas like pressure & temperature and are averaged over all the particles in the system at equilibrium. For the macroscopic description to be valid the gas must be in local equilibrium, that is there must be a sufficient number of collisions between particles. For example, the air in the room (at standard conditions) is considered a continuous medium and its temperature can be measured with a thermometer. The gas temperature measured by the thermometer is a measure of the average energy of the particles comprising the system. Now consider an individual air molecule, it will move undisturbed until it collides with another molecule and these collisions control the motion of the particle. As the air molecules collide together, the fast-moving molecules will eventually collide and transfer energy to the slower moving molecules, driving the system to equilibrium with a single macroscopic temperature. This macroscopic description of a fluid is the basis for

continuum mechanics and is valid when the length scale of a system of interest is much greater than the mean free path of the particles.

Statistical thermodynamics describes a gas on the microscopic level. The microscopic description considers the gas as a collection of discrete particles. Consider again the air in the room, but this time as a collection of atoms and molecules instead of as a continuous medium. The molecules of air are mostly diatomic and can be thought of as a dumbbell with one atom at each end. This molecule has several modes of energy:

1. The molecule is traveling through space, and therefore has translational kinetic energy (E_{trans}) associated with it, equation 2.1:

$$E_{trans} = \frac{1}{2} m\left(v_x + v_y + v_z\right)^2 \quad (2.1)$$

   Where m is the mass of the molecule and v_x, v_y, v_z are the three components of the velocity in the x, y and z-directions respectively. Since the molecule can move in three dimensions (x, y, z) it is said to have 3 thermal degrees of freedom, figure 2a. [13].

2. The molecule can rotate about three orthogonal axes in space and, therefore has rotational energy (E_{rot}) associated with it, figure 2b. The energy comes from its angular velocity and its moment of inertia about each axis. Returning to the dumbbell representation, a diatomic molecule has a very small moment of inertia about its internuclear axis (z-axis) and its contribution to the rotational energy is negligible. Therefore, diatomic molecules are said to have two rotational degrees of freedom, [13].

3. The atoms of the molecule are vibrating with respect to an equilibrium position, and therefore has vibrational energy (E_{vib}). The vibration of a diatomic molecule is still modeled as a dumbbell but has a spring connecting the two atoms and only has one geometric degree of freedom (vibration along the internuclear axis), figure 2c. There are two sources for the vibrational energy. First, the kinetic energy associated with the linear motion of the atoms as they move along the internuclear axis. Second, the potential energy associated with the intermolecular force holding the two atoms together. Even though the molecule only has one geometric degree of freedom it has two thermal degrees of freedom (kinetic and potential contributions), [13].
4. The electrons surrounding each atom are in motion about its nucleus, and therefore has electronic energy (E_{ele}), figure 2d. There are two sources of electronic energy associated with each electron. First, the kinetic energy associated with the motion of the electron as it orbits the nucleus. Second, the potential energy associated with electron's interaction with the electromagnetic field of the nucleus and other electrons [13].

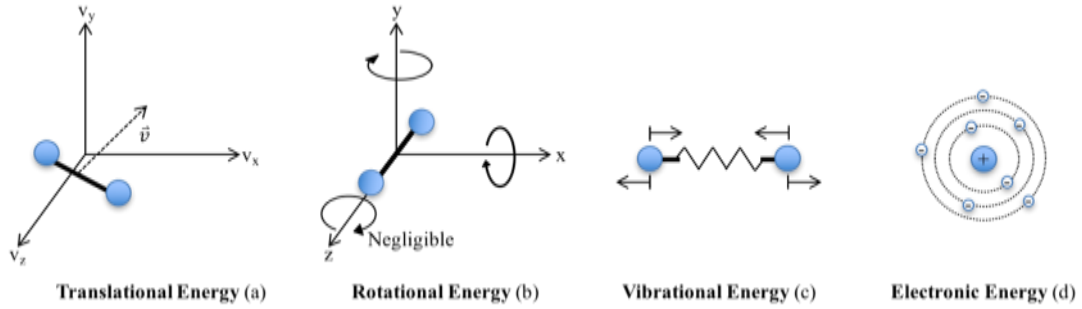

Figure 2. Molecular energy modes.

The total energy of a molecule (E_{tot}) is the summation of all the different energy modes, equation 2.2:

$$E_{tot} = E_{trans} + E_{rot} + E_{vib} + E_{ele} \quad (2.2)$$

However, for a single atom, like argon, only the translational and electronic energy levels are applicable because all three moments of inertia are negligible with regards to the rotational energy.

The dissociation of molecules can be thought of as another energy mode, because large amounts of energy are required to break the molecular bonds. In a spark discharge, multiple dissociation reactions are possible including:

- Electron impact dissociation, occurs when a high-energy electron interacts with a neutral particle.

$$e^- + N_2 \rightarrow N + N + e^-$$

- Heavy particle dissociation occurs when two excited particles interact.

$$N_2^* + N_2^* \rightarrow N + N + N_2$$

These dissociation mechanisms will result in a decrease in the conversion efficiency because a portion of the electrical energy will lead to dissociation rather than thermal energy in the flow. In addition, when the gas temperature reaches a point, the translational energy of the particles is sufficient to thermally dissociate one of the interacting molecules.

$$N_2^T + N_2^T \rightarrow N + N + N_2$$

The dissociation can be thought of as a pseudo phase change in that much more energy is required to raise the gas temperature while the N_2 dissociates, similar to the boiling process of any liquid.

2.1.2 Plasma Discharges

Plasmas fall under several categories according to their temperature, composition, size and electrical characteristics. Based on the relative temperatures of the electrons, ions, and neutrals, plasmas are classified as thermal or non-thermal. A thermal plasma is generated by heat addition. This thermal ionization method will create a bulk plasma but requires a temperature on the order of 10,000 K to create a sufficient number of charged particles through random collisions. A thermal plasma is considered to be in equilibrium, because the average temperature or energy of the free electrons is equal to the average temperature of the bulk gas. That is, the electrons and the heavy particles (ions and neutrals) have the same temperature, $T_e = T_{gas}$. Note, the electron temperature (T_e) is the average kinetic energy of the unbounded electrons in the plasma, not the electronic temperature (T_{ele}) associated with the bounded electrons in an atom/molecule. A thermal or equilibrium plasma typically has a high degree of ionization, the percentage of neutral

particles that are ionized. Applications of thermal plasma are limited due to their extreme temperature but include arc welding and fusion research.

A non-thermal plasma is not in equilibrium because the average temperature of the electrons is not equal to the bulk gas temperature. A typical temperature distribution for a non-thermal plasma is:

$$T_e = T_{ele} \geq T_{vib} \geq T_{rot} = T_{trans} = T_{gas}$$

Where T_e is the electron temperature, T_{ele} is the electronic excitation temperature, T_{vib} is the vibrational temperature, T_{rot} is the rotational temperature, and T_{trans} is the translational temperature of the molecule/atom. This temperature distribution depicts a plasma where the vibrational and electronic energy modes of the molecules are excited much more than the rotational and translational energy modes. Due to this non-equilibrium distribution of energy the plasma remains chemically active (from vibrational excitation), while maintaining a low gas temperature. Non-thermal plasmas promote chemical reactions at a lower operating temperature then a conventional catalyst. A non-thermal or non-equilibrium plasma has a lower degree of ionization compared to a thermal plasma, but is still quasineutral and exhibits collective behavior. Non-thermal plasmas have a wide range of applications including: fluorescent lighting, semiconductor processing (deposition and etching), sterilization, petroleum processing, and others.

A plasma can be created and sustained with the application of a strong electric field without substantial heating to the bulk gas. This is possible because the electric field can directly add energy to the electrons. Consider two electrodes separated by a gas and connected to a power source, figure 3. The electric field initially accelerates a single free

electron, produced by cosmic ray or another external source. The accelerating electron will eventually collide with another particle. If the energy of the electron is less than the ionization energy (energy required to remove the outer most electron from an atom/molecule in its ground state) for a given gas the electron will transfer its energy to one of the varies energy modes of the particle it collides with. If the electric field strength is increased to a point where the energy gained by an electron between collisions is larger than the ionization energy the electron will ionize the next particle it collides with. After the first ionization event two electrons exist between the electrodes, and both will be accelerated to a kinetic energy greater than the ionization energy. These two accelerating electrons will then collide with two other particles and ionize them, removing two more electrons. The acceleration/ionization process will continue and an electron avalanche will form in the discharge gap (space between the electrodes).

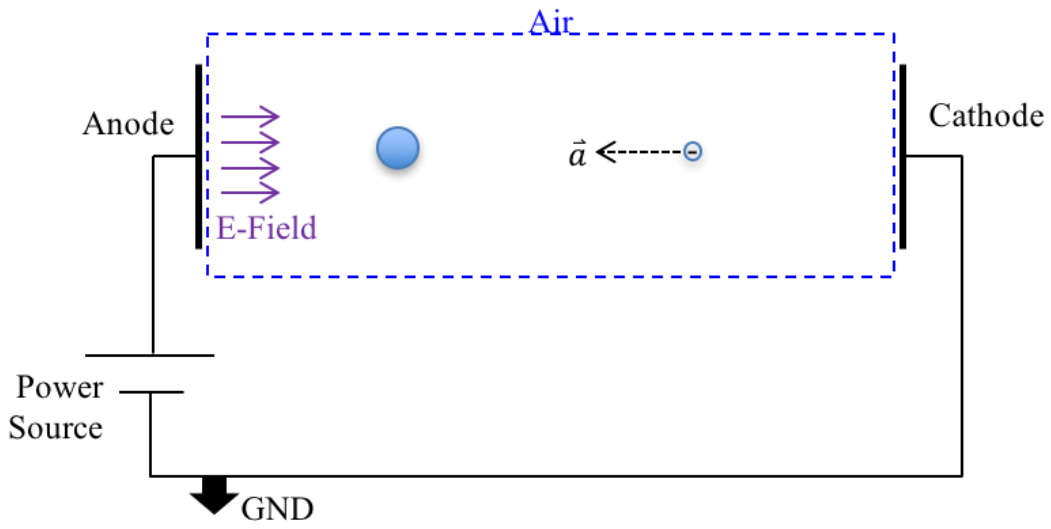

Figure 3. Schematic of electric field plasma generation.

For a given pressure the discharge gap determines the voltage (breakdown voltage) required to initiate the electron avalanche. As the electrons ionize the gas its dielectric strength breaks down forming a conducting medium, plasma. The applied voltage and the electrode spacing determine the electric field in units of [V/m] required to breakdown the gas depending on its composition, [14].

Plasma discharges are classified by their voltage and current characteristics, figure 4. The region from A to E is the dark discharge regime and depicts the ionization process described above. Once breakdown is achieved the required voltage drops significantly due to the transition of the gas from an insulator to a conductor and current begins to flow from anode to cathode and the plasma transitions into a glow discharge, from E to F. As the current is further increased from point F, the normal glow discharge transitions into an abnormal glow discharge, that only occurs if the electrode area is limited and at high pressures. An abnormal glow is not typical. At point H, the temperature of the electrodes become hot enough that the cathode begins to emits electrons thermionically. If sufficient current is supplied to the discharge it will undergo a glow-to-arc transition, from H to I. The arc regime, from I to K, will continue as long as sufficient current can be supplied to the discharge.

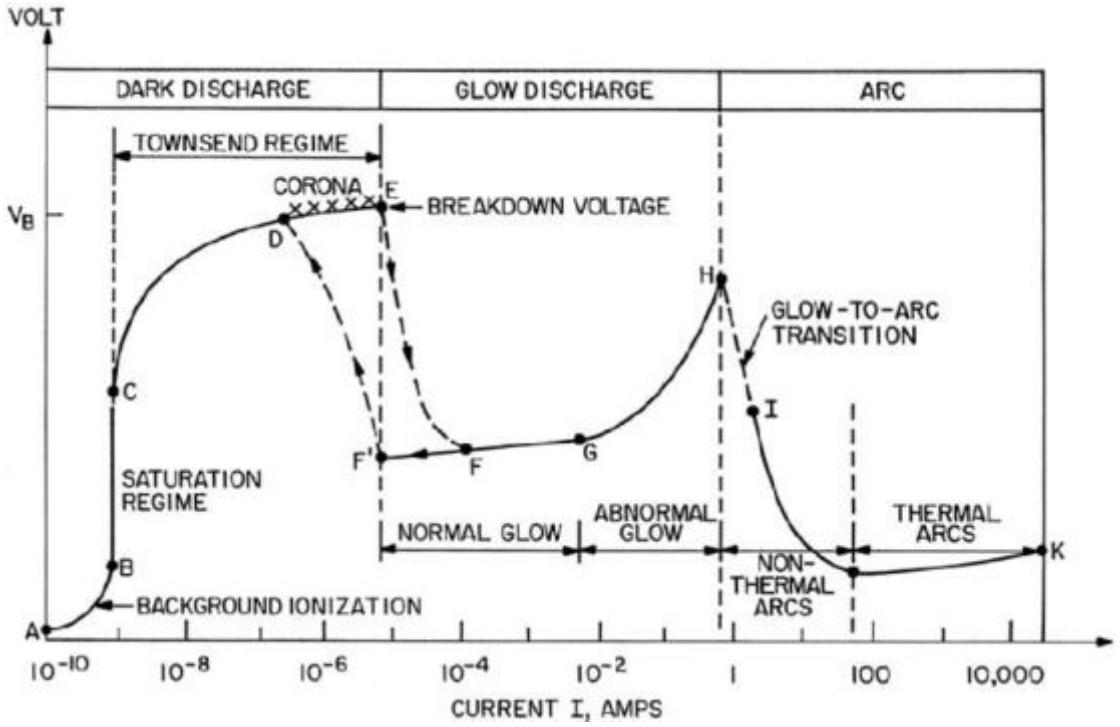

Figure 4. Current-voltage characteristic of an electric discharge.

If the power source driving the discharge cannot sustain the current required by an arc the discharge will extinguish itself. Consider an RC circuit powered by a high voltage DC source connected in parallel with a discharge gap filled with air, figure 5. The capacitor will charge up until the voltage across it reached the breakdown voltage (V_b) of the gap. Once breakdown is achieved the capacitor will discharge across the gap. Since the discharge gap now has a low electrical resistance the current flowing from the capacitor will be large and the discharge transitions to an arc. However, this large current can only be supplied by the capacitor for a very short time, on the order of 10s of nanoseconds, depending on the plasma's electrical resistance. Once the capacitor's output current cannot sustain the arc the discharge extinguishes. This extremely short time scale arc is called a

spark discharge. A Lighting strike during a storm is an example of a spark discharge, albeit on a very large scale. A spark discharge is accompanied by a characteristic cracking sound produced by a blast wave generated by the rapid increase in pressure due to the intensive release of energy in the spark channel, [14].

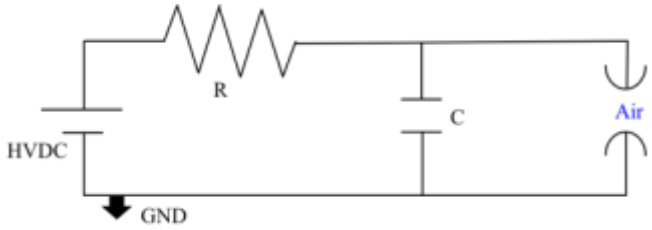

Figure 5. RC circuit connected in parallel to air gap.

2.2 Energy Deposition

The utilization of plasma for flow control has been of interest for many decades. The declassification of the AJAX program, which is a conceptual hypersonic, air-breathing aircraft originally designed by the Leninetz Holding Company in St. Petersburg, Russia [2]. The AJAX aircraft utilized microwave generators to create an ionized airflow ahead of the aircraft. The ionized airflow allowed for the precise control of the aircraft's aerodynamics which was controllable by shifting the focal point of the microwave radiation. The benefits of the ionized airflow included reduction in drag and heat transfer, and an increased lift force leading to an overall increase in the aircraft's lift-to-drag ratio, [16, 17]. The AJAX program drew the attention of researchers and scientists from many countries to the use of plasma for flow control at supersonic and hypersonic velocities. The AJAX program also lead to the creation of bilateral conferences in the fields of aerospace plasma technologies between the United States and Russia beginning in 1997,

which lead to a great wealth of knowledge in the field of energy deposition over the past two decades, with the bulk of the effects having been quickly recognized as predominantly thermal in nature, [3, 18, 19, 20]

2.2.1 Deposition Techniques

Many different energy deposition techniques have been developed over the past few decades, including, but not limited to: plasma arcs/sparks, laser pulses, microwave radiation, and electron beams. The deposition techniques can be categorized into two groups. First, the deposition techniques that require physical contact with the flow. These techniques include the spark and arc discharge because they require an anode and cathode to produce a plasma. This technique is not widely used due to the detrimental effects associated with its physical contact with the flow. However, this technique has been used to deposit energy on a surface, for example the leading edge of an airfoil. Leonov et al. [21, 22] performed a series of experiments to investigate the effect of surface electrical discharge on flow properties at transonic speeds. Electrodes were mounted flush to the floor of a M=0.95 transonic wind tunnel and created a surface plasma in the discharge gap that formed a subsonic heated zone near the surface.

Second, deposition techniques that do not require physical contact with the flow. The two techniques that have been experimentally investigated are deposition by high energy laser pulses, and focused microwave radiation. Both techniques focus down their respective EM radiation until the photon flux reaches a critical value ionizing the air creating a plasma. Experimental laser energy deposition has been performed in supersonic flows by Minucci et al. [8], Yanji et al. [23], Toro et al. [24], Tretyakov et al. [25] and

Adelgren et al. [26, 27, 28]. Minucci et al. used a CO_2 laser to create a directed energy air spike in a hypersonic shock tunnel [8]. Yanji et al. used an Nd:YAG laser at a wavelength of 1064nm and a pulse energy of 100mJ to break down the hypersonic flow in a shock tunnel [23]. Toro et al. performed a series of experiments for a directed energy air spike at M=10, with powers up to 70kW, [24]. Tretyakov et al. performed experiments to measure the drag on a cone-cylinder and hemisphere-cylinder at M=2 in argon in the presence of a high frequency CO_2 laser discharge upstream of the cylinders, [25]. Adelgren et al. examined the effect of pulsed energy deposition on the flow structure of an isolated sphere at M=3.45 using an A Nd:YAG laser at 532nm with a 10ns pulse duration, 10Hz repetition rate and energy levels ranging from 12mJ to 300mJ, [26, 27, 28].

Experimental microwave energy deposition has been performed in supersonic flows by Kolesnichenk et al. [7, 29-34] and Exton et al. [35]. Kolesnichenko et al. examined the effect of a microwave filament discharge on the aerodynamic drag of blunt bodies at M=1.7–2.1 in air, argon, carbon dioxide, and nitrogen. Peak microwave power reached 220kW at a maximum pulse duration of 2μs, [7, 29-34]. Exton et al conducted an experiment with microwave energy deposition at M=6 upstream of a blunt cylinder, with microwave pulses operating at 16.5GHz, a power 475kW and pulse duration of 3.5μs, [35].

2.2.2 Applications of Energy Deposition

The applications for energy deposition in high speed flows are numerous and include drag reduction, heat mitigation, shockwave mitigation, sonic boom alleviation

combustion enhancement, lift/moment enhancement, etc. The two applications that have received the most attention concerning experimental energy deposition are drag reduction and modification of the shock structure. The mechanism of drag reduction by energy deposition is similar to a spike extending from a blunt-nose of a supersonic/hypersonic vehicle. The spike generates a conical oblique shockwave that encompasses the vehicle and begins to turn the flow upstream of the vehicle. Pressure drag on the body can drop by 50% or more because the detached normal shockwave from the blunt nose is no longer present. However, the spike like the first set of deposition techniques, is a physical impingement on the flow and its effectiveness is limited because of cooling requirements and frictional drag of the spike, [3]. Energy deposition using technique 2 (laser or microwave radiation) would create a similar effect as the spike without its detrimental effects. The immediate effect of energy deposition focused upstream of the vehicle is to heat, pressurize, and slow the energized region. When sufficient energy is supplied weak compression waves form around the energized region. The interaction between the energized region and the vehicle causes the blunt nose normal shockwave to weaken and move upstream. This results in a rapid transition of the normal shockwave into an oblique shockwave and coalesces with the compression waves emanating from the energized region. The transition of the normal shockwave results in a large decrease in the pressure drag encountered by the vehicle, [3, 1]. To reduce drag in an energy-efficient fashion that improves at higher speeds, Kremeyer deposited energy impulsively along a body's stagnation line [4, 5, 6].

Experimental energy deposition in high speed flows for drag reduction has been performed by Tretyakov et al. [25] and Adelgren et al. [26, 27, 28] using a laser, Kolesnichenko et al. [7, 29-34] using microwave radiation, and Leonov et al. [21, 22] using surface electrical discharges. Tretyakov et al. measured a drag reduction of up to 45% of the baseline at M=2 by laser energy deposition, [25]. Adelgren et al. used single laser pulses to generate a thermal spot upstream of the isolated sphere's bow shock. Schlieren images were used to visualize the interaction between the bow shock and the thermal spot. The interaction caused the shock to lens forward resulting in a decrease in pressure on the surface of the sphere reducing drag. Once the thermal spot passes through the bow shock, a compression wave forms and the surface pressure recovers to its undisturbed value, [26, 27, 28]. Kolesnichenko et al. used schlieren visualization to view the lensing of the bow shock due to the interaction with the thermal spot generated by the microwave pulse. Surface pressure measurements displayed the initial drop in stagnation pressure associated with the expansion fan generated by the interaction of the thermal spot with the bow shock. Stagnation pressure measurements indicate a significant momentary drag reduction, [7, 29-34]. Leonov et al. used a flat plate force balance to evaluate the effect of surface discharges on skin friction drag at M=0.95. A frictional drag reduction of 15% to 20% was measured with respect to the baseline. [21, 22].

All the energy deposition techniques reviewed above are similar in that they create a high temperature, low density region upstream or on the surface of an aerodynamic body, [1, 3, 5, 9]. It is these thermal effects that are the primary mechanism for drag reduction and not effects from the plasma, which only acts to transfer the electrical energy into

thermal energy, [9]. Steady energy deposition upstream on an aerodynamic body reduces ρ in the drag force (D), equation 2.3.

$$D = C_d \frac{1}{2} \rho U_\infty^2 \quad (2.3)$$

Where C_d is the drag coefficient and U_∞ is the free stream velocity, [36]. Therefore, for this research the final expanded temperature and the final expanded density of the effected region created by the spark actuator, will be used to evaluate the effectiveness of the energy deposition process.

2.3 Schlieren Imagery

The expansion rate and final size of the high temperature, high pressure region are critical measurements required to quantify the discharge efficiency. However, the high temperature, high pressure region is just an amorphous bubble of hot air, that is indistinguishable from the surrounding air to the human eye or any camera operating at any wavelength. Therefore, schlieren imagery, which allows the visualization of phenomena in transparent media, was utilized to measure the rate of expansion and the final size of the discharge region.

Humans have no way to discern the phase difference in a ray of light, they see only amplitude, color and contrast. This is exactly what the schlieren method accomplishes, it translates the phase difference into amplitude and sometimes color differences, visible to the human eye. Light travels at it maximum speed of $c_o=3x10^8$[m/s] when propagating through a vacuum, however, it slows upon interactions with matter. The ratio of the light ray's velocity difference is termed the refractive index (n), equation 2.4:

$$n = \frac{c_o}{c} \quad (2.4)$$

Where c is the velocity of the light ray in the given medium. For air the refractive index is related to the density by equation 2.5:

$$n - 1 = k\rho \quad (2.5)$$

Where k is the Gladstone-Dale coefficient, k=0.23 [$cm^3\ g^{-1}$] for air at standard conditions, and the term (n-1) collectively is referred to as the refractivity of the medium. The refractive index is only weakly dependent on the density and therefore a precise, sensitive optic system is required to detect the variations [37].

The schlieren imaging method works because optical inhomogeneities refract or bend light rays in proportion to their gradients of the refractive index [8, Settles]. Take, for example, an undisturbed light ray (from the extended light source) propagating in the positive z-direction towards a region with varying density (S) and therefore varying refractive index, figure 6.

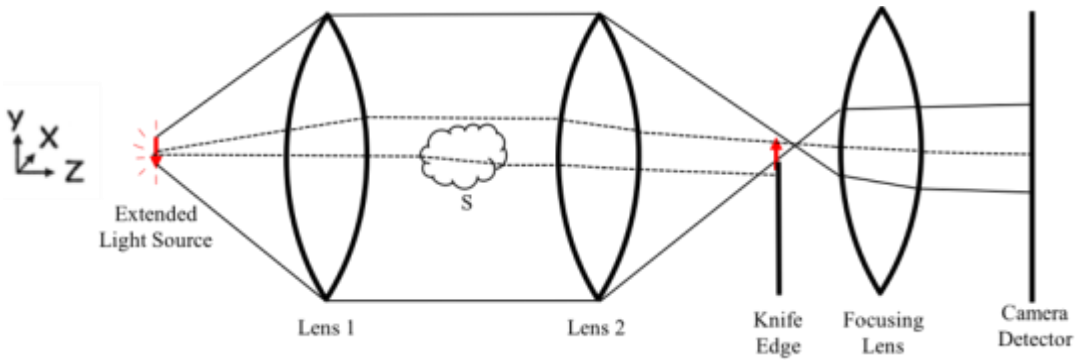

Figure 6. Light ray propagation in a schlieren imaging system.

The resulting ray curvature is given by equation 2.6.

$$\frac{\partial^2 x}{\partial z^2} = \frac{1}{n}\frac{\partial n}{\partial x} \quad , \quad \frac{\partial^2 y}{\partial z^2} = \frac{1}{n}\frac{\partial n}{\partial y} \qquad (2.6)$$

Integrating the above equations once yields the components of the ray deflection in the x and y directions. For a two-dimensional schlieren setup with length L along the optical axis (z-axis), the ray deflection ε_x & ε_y are given by equations 2.7.

$$\varepsilon_x = \frac{L}{n_o}\frac{\partial n}{\partial x} \quad , \quad \varepsilon_y = \frac{L}{n_o}\frac{\partial n}{\partial y} \qquad (2.7)$$

Where n_o is the refractive index of the surrounding gas [37].

Equations 2.6 gives a mathematical basis for the schlieren imaging method. The gradient of the refractive index causes the light ray to deflect. Combining equation 2.5 with equation 2.6 shows the relationship between the ray deflection and the gas density, equation 2.8.

$$\varepsilon_x = \frac{L\,k}{\rho_o k + 1}\frac{\partial \rho}{\partial x} \quad , \quad \varepsilon_y = \frac{L\,k}{\rho_o k + 1}\frac{\partial \rho}{\partial y} \qquad (2.8)$$

Where ρ_o is the density of the surrounding gas, and shows the light ray is always bent towards the region of higher density. Equation 2.8 shows the illumination level in the schlieren image responds to the first spatial derivative of the density. This sensitivity is what distinguishes a schlieren systems from a shadowgraph imaging systems. A shadowgraph is similar to a schlieren image but is only sensitive to the second spatial derivative of the density. Since the schlieren system is more sensitive it was used to measure the expansion and final size of the high temperature, high pressure region created from the energy deposition process.

3. EXPERIMENTAL SETUP

3.1 Experimental Setup

To measure the conversion efficiency of electrical energy into thermal energy in a supersonic flow a spark actuator was designed and manufactured. The spark actuator is powered by a DC charging RC circuit, that had its voltage and current characteristics measured to allow calculation of the energy of the spark actuator. The energy deposition process was imaged utilizing a schlieren and direct imaging approach, using an Intensified CCD (ICCD) camera. The spark actuator was installed inside the SHR wind tunnel, located at the NAL.

3.1.1 Spark Actuator

The spark actuator is the energy deposition device responsible for the conversion of electrical energy into usable flow energy. The spark actuator consists of two sharpened tungsten electrodes sheathed in alumina tubes that are inclined through a machined MACOR insert which protrudes the electrodes into the flow causing minimal disturbance, figure 7, 8.

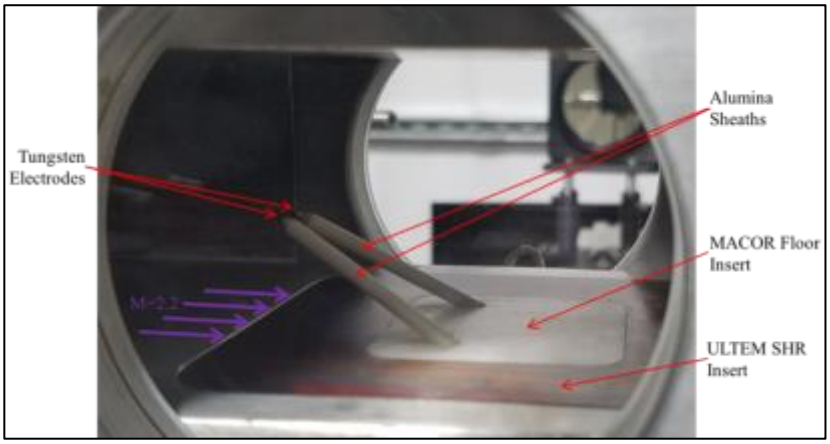

Figure 7. Spark actuator installed inside the SHR tunnel.

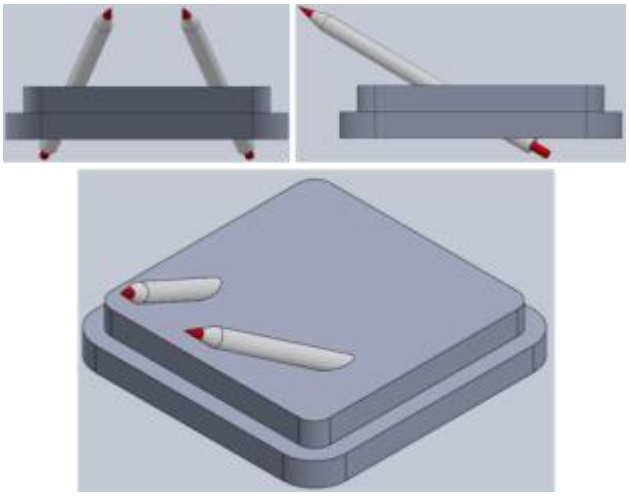

Figure 8. CAD drawings of spark actuator: front view (top right), side view (top left), isometric view (bottom).

The electrodes are 1/16in OD pure tungsten welding rods that were sharpened to a fine point by precision diamond grinding. The electrodes were then sheathed up to their sharpened tips inside 1/8in OD alumina tubes (McMaster-Carr part #8746K11) to electrically insulate them from each other. A MACOR insert (McMaster-Carr part #8489K237) was machined to SHR test section insert dimensions, which allowed its inclusion into an existing ULTEM floor insert. The MACOR insert had two 1/8in diameter holes drilled at 60° normal to the top surface, creating a sealable passageway for the alumina sheaths, inclining the electrodes 30° relative to the incoming flow.

The two electrodes are separated by a distance or discharge gap (L_d) of 0.3in (7.62mm) from each other. This region between the electrodes spanning the discharge gap is the discharge region where the spark forms. The discharge region is centered vertically in the test section with a 1.0in (25.4 mm) clearance above and below, thereby maximizing its electrical insulation from the SHR tunnel. The 30° inclination of the electrodes was

designed to create a region of flow directly behind the discharge region with minimal disturbances for clear schlieren images of the energy deposition expansion (expansion region), figure 9.

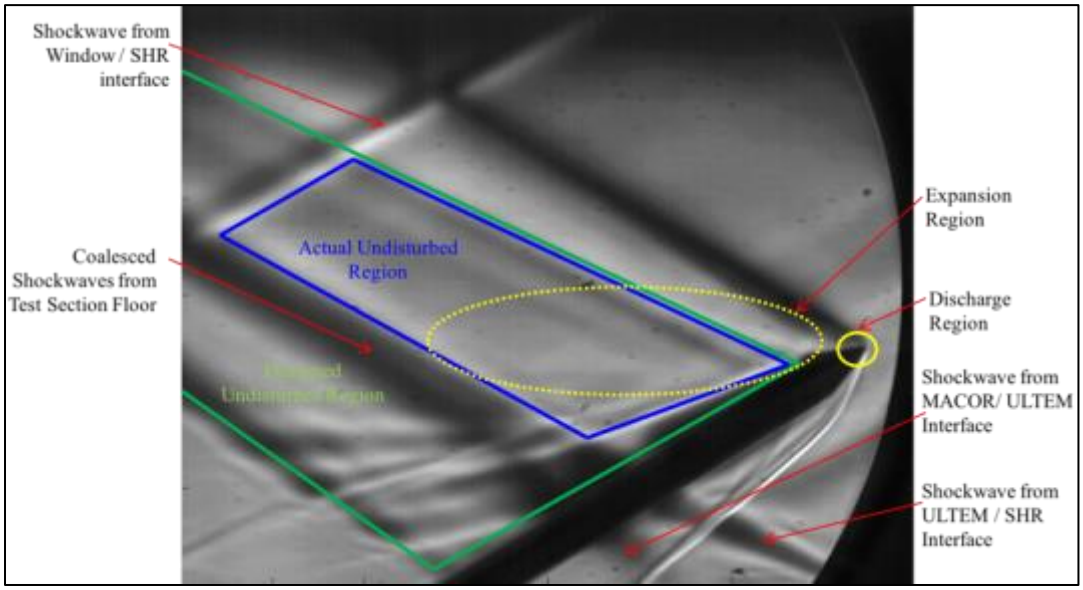

Figure 9. Schlieren image with undisturbed regions and discharge region.

The actual undisturbed region was smaller than designed due to shockwave interference. The lower boundary of the undisturbed region was affected by two shockwaves from the test section floor. The first shockwave was from the interface between the ULTEM floor insert and the SHR tunnel. The second shockwave was from the interface between the MACOR insert and the ULTEM floor insert. These two shockwaves coalesced further downstream limiting the undisturbed region. The upper boundary of the undisturbed region was limited by a shockwave emanating from the interface between a top mounted window and the SHR tunnel. Figure 10 shows the spark actuator in operation, with C=1000pF.

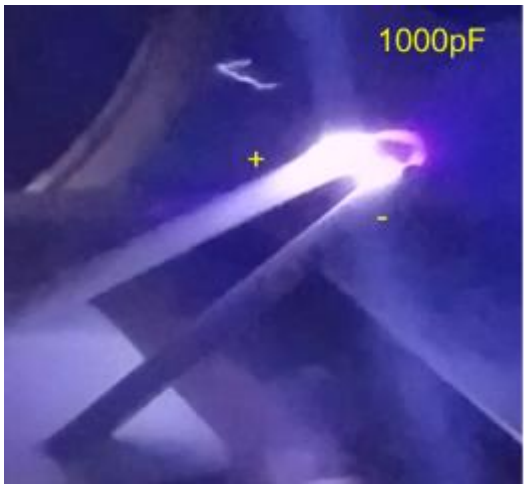

Figure 10. Spark actuator in operation inside SHR tunnel, with C=1000pF.

3.1.2 Electrical Circuit & Diagnostics Setup

The external electrical circuit powering the spark actuator is a DC charging RC circuit, figure 11. The circuit is powered by a Glassman KL030P090 high voltage power supply. The Glassman power supply has a maximum output of 2700W with a maximum voltage of +30kVDC and a maximum output current of 90mA. The ballast resistor (R_b) has two function, first it is in series with the spark actuator to protect the power supply during discharge. The resistor prevents the plasma from drawing too much current too fast from the power supply. Second, the ballast resistor along with the capacitor (C) set the RC time constant (τ) equal to the product of the capacitance and the ballast resistance, which dictates the charging rate of the capacitor thereby limiting the discharge frequency of the spark actuator. The ballast resistors used during the entire experiment were ten 10MΩ (Vishay Part # ROX30010M0FNF5) in parallel resulting in an equivalent resistance of 1MΩ. The capacitor is the charge storage device in the circuit and its capacitance dictates the energy per pulse because the discharge gap length is held constant.

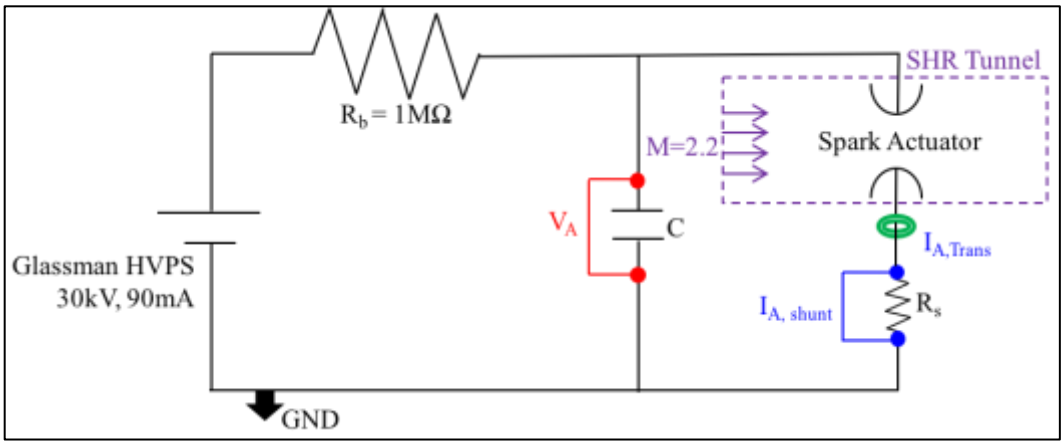

Figure 11. Circuit schematic powering spark actuator.

The circuit operates by charging the capacitor through the ballast resistor from the potential difference created by the power supply. The capacitor will continue to charge until the voltage across the capacitor is equal to the charging voltage, or the voltage across the capacitor reaches the local breakdown voltage of the discharge gap. Once the capacitor reaches the local breakdown voltage of the discharge gap the capacitor will discharge across the spark actuator and through the shunt resistor R_s to the ground plane completing the circuit. The current from the power supply is not large enough to sustain a continuous arc discharge and therefore, once the current from the capacitor drops below the threshold to sustain the discharge the gap reverts to an insulator and the capacitor begins to charge again restarting the cycle.

The voltage and current were measured to characterize the spark actuator. The voltage across the capacitor is equal to the voltage across the spark actuator (V_A) as they share a common anode and cathode (ground connection); the resistance of R_s is negligible. The voltage across the capacitor is measured by a North Star PVM-4 1000:1 high voltage probe, capable of voltage measurements up to 40kV, figure 12. The North Star probe was

routed to a LeCroy Waverunner 204MXi oscilloscope to visualize and save the voltage waveforms. The current through the spark actuator was measured using two different methods. First, the voltage drop across the shunt resistor was measured by a LeCroy PPE6KV voltage probe routed to the same oscilloscope, figure 13. Second, a Pearson 5046 current transformer indirectly measures the current through the spark actuator, figure 13.

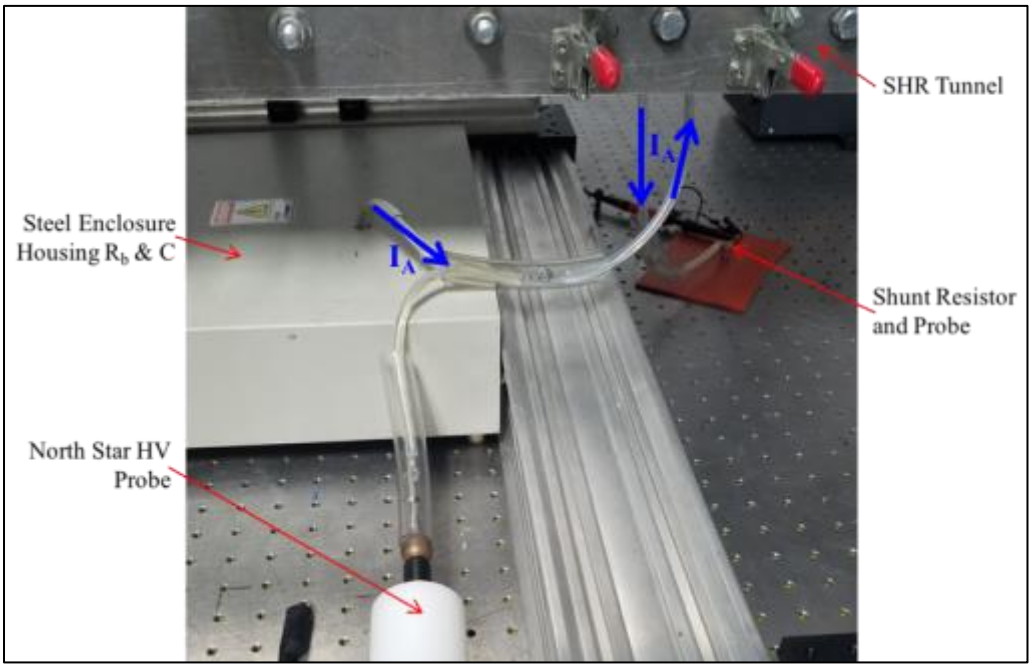

Figure 12. North Star high voltage probe connection.

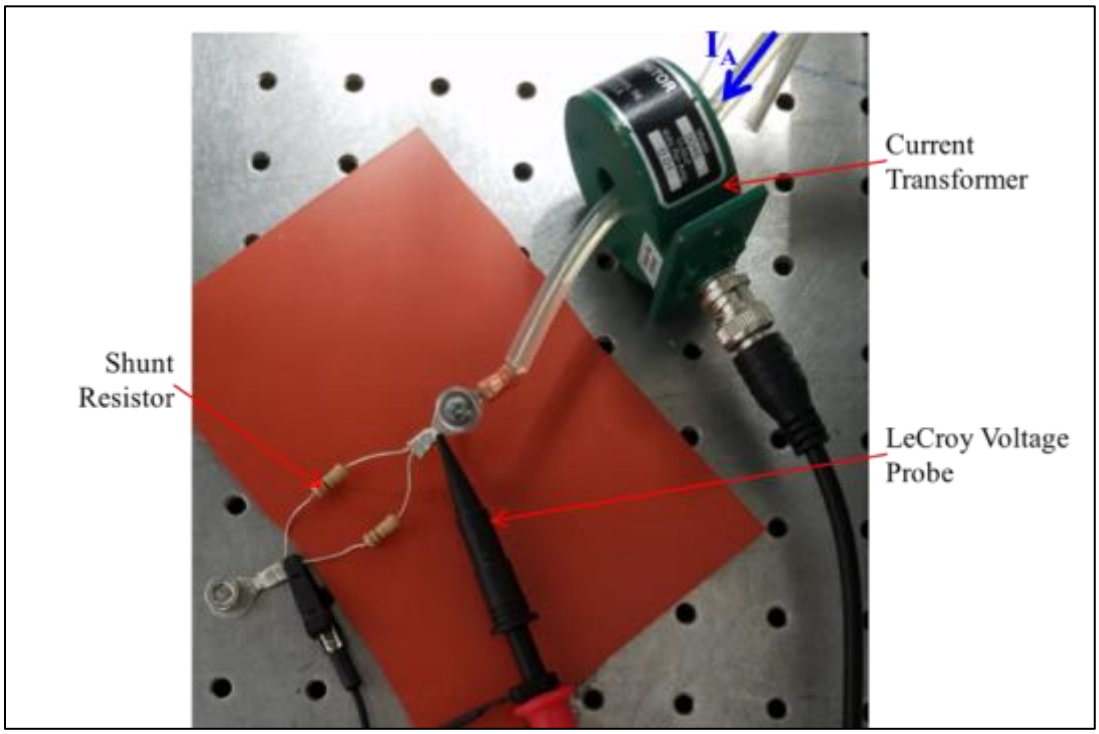

Figure 13. Current measurement setup.

3.2 Imaging Setup

A schlieren imaging system was used to measure the time evolution of the energy deposition process. The gas expanding from the discharge region will have lower density than the surrounding gas because of the high temperature associated with the energy deposition. This low density expanding region will have a large density gradient across its interface with the surrounding gas, which can be imaged using the schlieren system. From the time resolved schlieren images, the final expanded volume and expansion ratio for each energy input was measured.

3.2.1 Schlieren Hardware Setup

An experimental schlieren setup consists of a collimated light beam, a focusing element, a knife edge and a camera, figure 14. To create a collimated light beam, a light source is passed through a horizontal slit and focused on a 6in parabolic collimating mirror, figure 15. The light source used was a HPLS-36DD18B pulsed LED light, that is capable of 100ns–1000ns pulses with 1% duty cycle at 18 Amps. The collimated light beam is passed through the discharge region inside the SHR test section. A second 6in parabolic mirror was used as the focusing element. The horizontal knife edge was placed at the focal point of the second parabolic mirror. A 2in diameter 60mm focal length lens then focused the light beam into the camera, figure 16. The camera used was a Cooke PCO 1600, that captures a 14 bit image with a minimum exposure of 500ns. The PCO camera has a minimum internal delay of 5.3μs. Because a horizontal knife edge was used at the focal point, only density gradients in the vertical direction (y) are visible. If a vertical slit and knife edge had been used instead of horizontal ones, density gradients in the horizontal direction (x) would be visible.

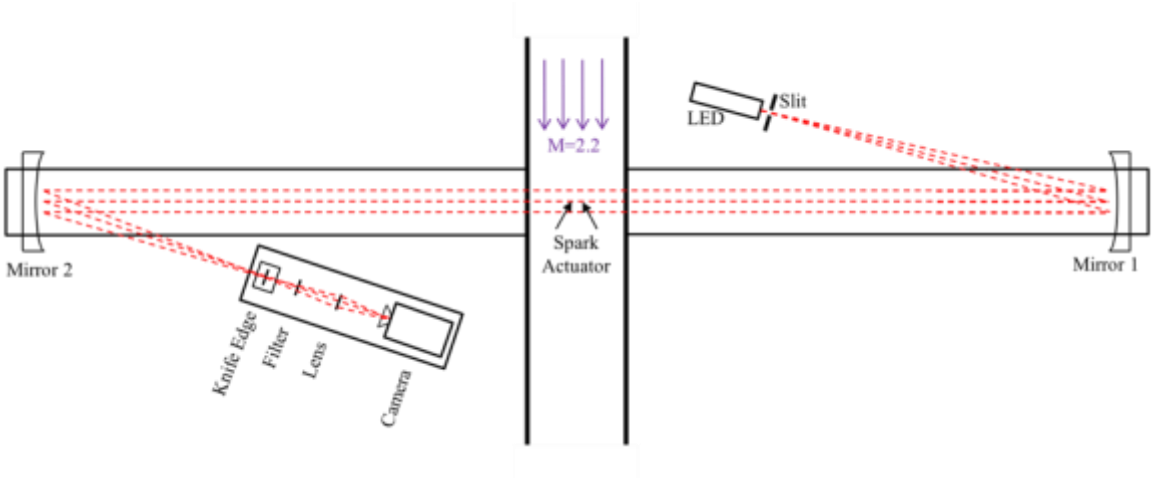

Figure 14. Schlieren setup schematic.

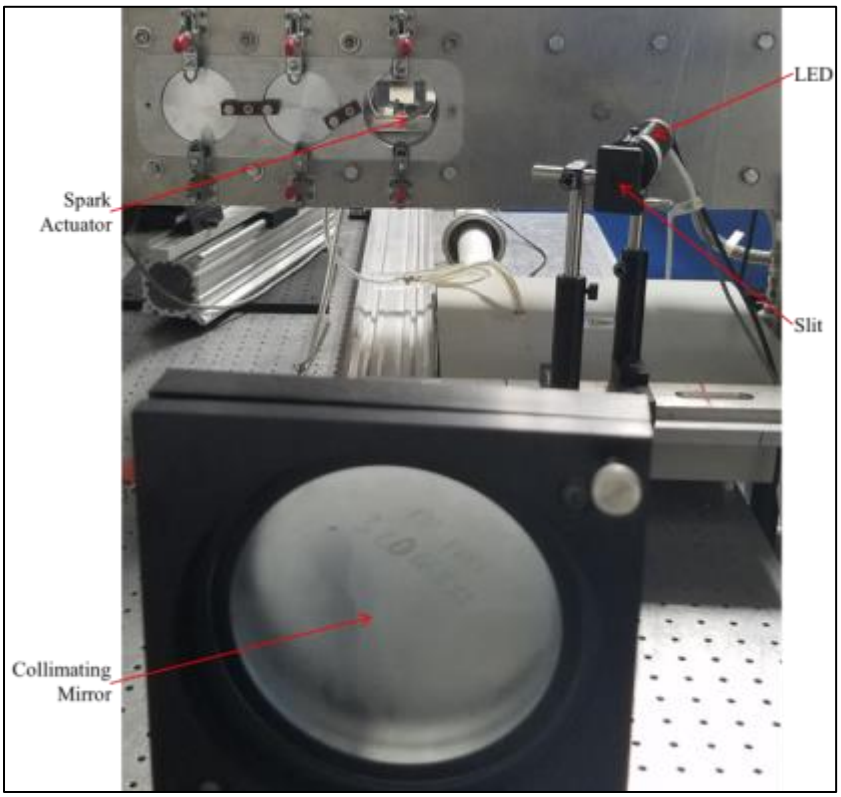

Figure 15. Collimating portion of schlieren setup.

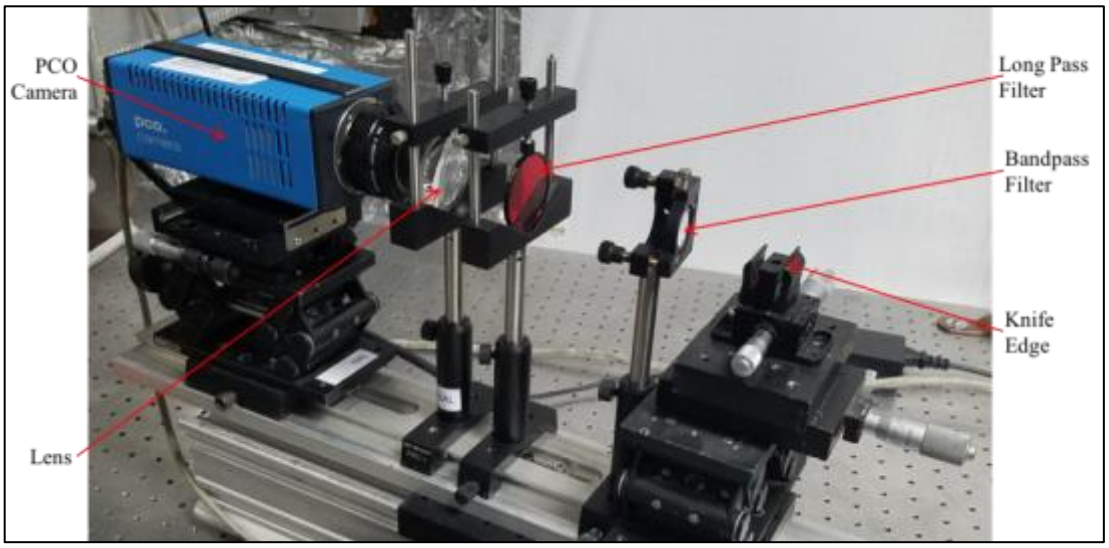

Figure 16. Knife edge and image capture portion of schlieren setup.

3.2.2 Plasma Light Filter

While operating the spark actuator at higher energies (>100pF) and imaging at delays less than 15μs a portion of the schlieren image became over exposed from the light emitted by the plasma, figure 17. To protect the camera and image the higher energy cases, a filter was to limit the plasma light reaching the camera. To determine what type of filter was needed, spectra of the plasma were taken, orange curve figure 16.

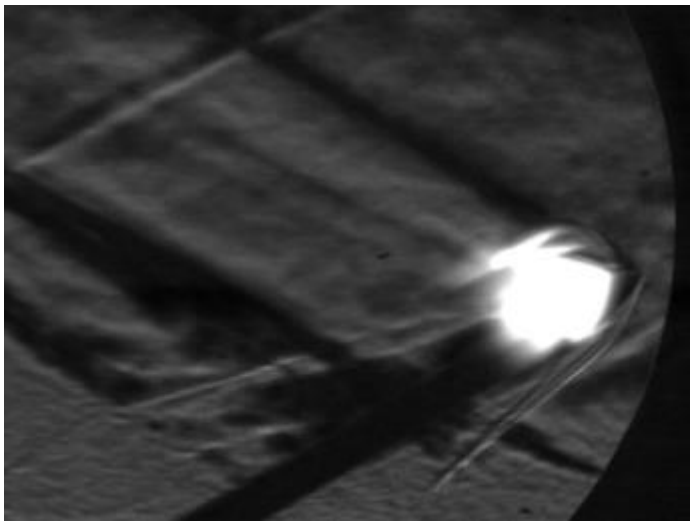

Figure 17. Schlieren image with portion obscured by plasma light.

The light source uses a LED operating at 632.8nm, purple curve figure 18. First, a 610nm long pass filter was placed in the beam path. This filter helped to protect the camera as the images were no longer overexposed but the discharge and beginning of the expansion regions were still obscured by the plasma light. Next, a 1in diameter bandpass filter was placed in the beam path. The bandpass filter has a central wavelength of 632.8±2nm with a FWHM of 10±2nm, green curve figure 18. The bandpass filter greatly reduced the intensity of the plasma light but still obscured most of the images for the highest energy case (10,000pF). At the end of experimental testing it was discovered that the bandpass filter was too small to block all the plasma light. The plasma light was reflected by the second parabolic mirror but was not focused down to the same focal point as the LED light. As a result, a portion of the plasma light passed around the 1in bandpass filter but hit the following 2in lens and was focused into the camera creating the plasma glare seen in images for the higher energy cases.

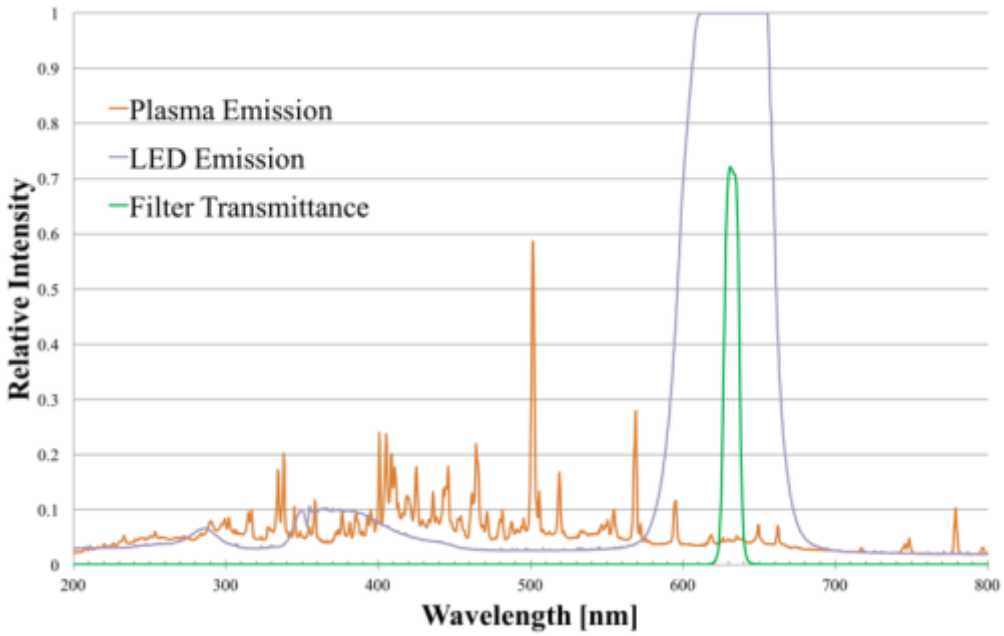

Figure 18. Spectrum of plasma emission, LED emission, and filter transmittance.

3.2.3 ICCD Direct Imaging Setup

To measure the initial volume of the plasma filament, which corresponds to the volume affected by the energy deposition. The plasma filament exists as long as current is flowing through the discharge region from anode to cathode and lasts for approximately 500ns. While current is flowing through the discharge region some of the molecules/atoms are electrically excited and emit light as they relax back to a lower energy state. The emitted light is what makes the filament visible to the human eye and allows the plasma to be directly imaged.

Since the plasma filament only emits light for ~500ns, a camera with a small internal delay and small exposure was required. The camera used to image the filament was a Stanford Computer Optics 4-Picos High Speed ICCD camera. The 4-Picos camera has an internal delay of 80ns and a minimum exposure of 0.2ns, allowing it to directly

image the plasma filament near its maximum brightness. The 4-Picos camera was mounted above the SHR tunnel and angled down for a clear line-of-sight to the discharge region, figure 19.

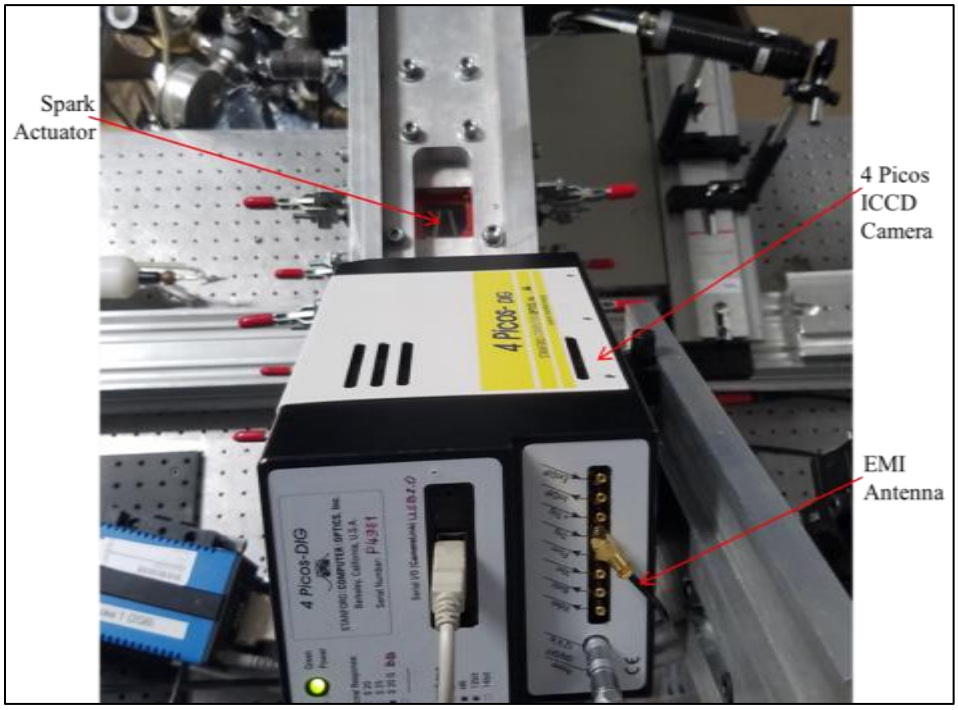

Figure 19. ICCD camera setup, top view.

To sync the 4-Picos shutter with the plasma discharge an antenna (6in bare wire) was attached to the –Trig input. The antenna was used to pick up the Electromagnetic Interference (EMI) produced by the spark actuator during discharge. Electromagnetic waves travel at the speed of light (if propagating through a vacuum) and therefore are the fastest method to trigger the camera. The 4-Picos camera's exposure was set to 5ns to image the plasma. A 5ns exposure was long enough to allow sufficient light to reach the camera detector, but short enough to minimize the dynamical effects and background noise. A background image with a 10,000pF discharge overlaid is shown in figure 20.

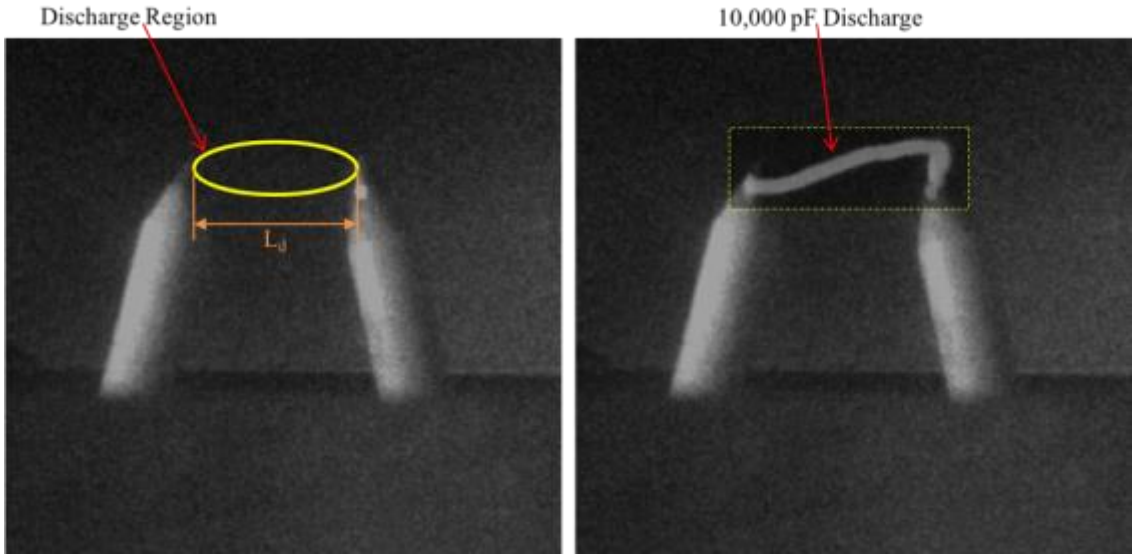

Figure 20. Background image with discharge region as shown in yellow in figure 8 (left); 10,000pF discharge overlaid on background (right).

3.3 National Aerothermochemistry and Hypersonics Laboratory

The National Aerothermochemistry and Hypersonic Laboratory is located at the Wind Tunnel Complex at Easterwood Airport and houses many supersonic wind tunnels including the NASA Langley Mach 6 Quiet Tunnel, the Actively Controlled Expansion Hypersonic Tunnel and the Supersonic High-Reynolds Number Tunnel (SHR). The SHR tunnel and was initially developed for fundamental turbulent boundary layer research but has since been used on numerous projects spanning multiple disciplines. The SHR tunnel was originally designed in 2005 by Isaac Ekoto and Kan Kobayashi under the mentorship of Dr. Rodney Bowersox, the director of the NAL and the department head of the Aerospace Engineering Department at Texas A&M University. The tunnel has been modified multiple times since 2010 by PM&AM Research and continues to be upgraded

to facilitate the many energy-deposition-based flow-control programs the company has executed at Texas A&M University.

3.3.1 Supersonic High Reynolds Number Wind Tunnel

The SHR tunnel is a blow down style wind tunnel consisting of a settling chamber, converging-diverging nozzle, test section, converging-diverging diffuser, and muffler, figure 21. The heated compressed air first passes through the settling chamber, which produces a smooth uniform flow heading into the nozzle. The properties of the flow in the settling chamber represent the stagnation or total conditions of the flow. The settling chamber consists of many types of meshes with varying sized holes with diameters ranging from 4.8mm to 88.9μm that straighten and smooth the air, reducing turbulence. The settling chamber's exit was designed to have the inviscid core of the flow pass straight through the square exit, so that boundary layer growth does not begin until the inlet of the nozzle. The nozzle is a finite radius, half-nozzle where the shape contour is only on the upper portion of the nozzle and the bottom portion is flat. As the air passes through the converging portion of the nozzle it is accelerated from stagnation conditions to sonic conditions at the throat (location with minimal cross-sectional area). The flow then enters the converging portion of the nozzle and continues to accelerate from sonic conditions to the design Mach number at the exit of the nozzle (M=2.2), [38, 39].

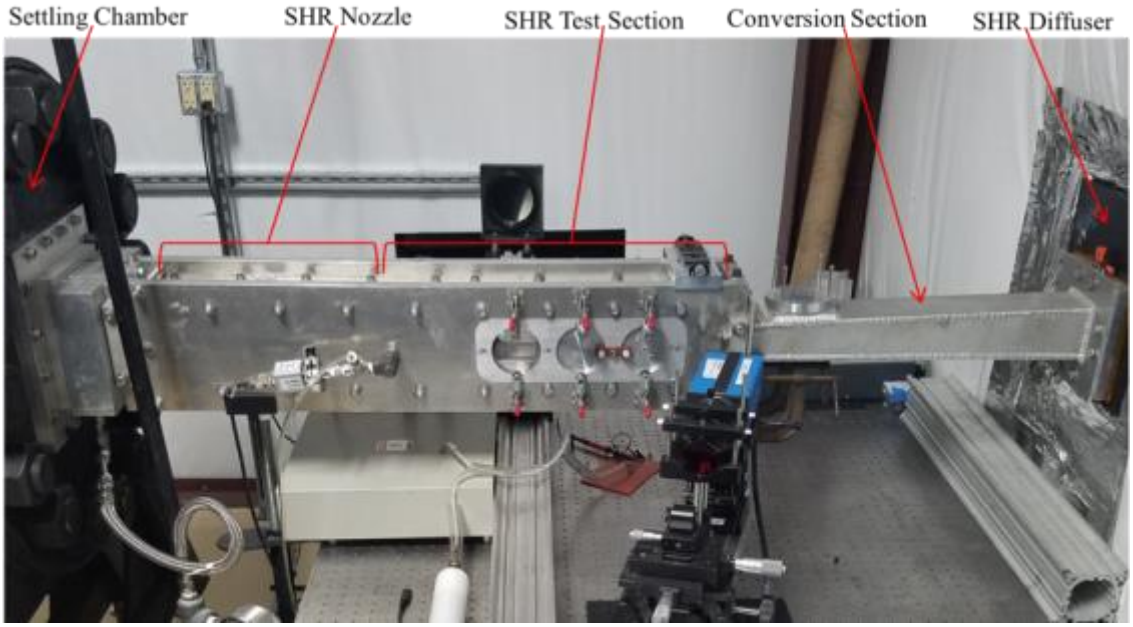

Figure 21. Components of the SHR wind tunnel.

At the exit of the nozzle, the fluid is flowing at Mach 2.2 and enters the test section where the spark actuator is located. The test section has a rectangular cross-section 4.0in wide by 2.0in tall and is 21.5in long. After the test section, the SHR tunnel has a 2.0ft long conversion section that brings the cross-section from 4in x 2in to 3in x 3in at the beginning of the diffuser. The diffuser has a similar converging-diverging contour as the nozzle. Ideally the diffuser decelerates the supersonic flow through the converging section of the diffuser until the flow reaches sonic velocity at the throat, and then continues to decelerate the now subsonic flow through the diverging section of the diffuser to reduce the overall pressure differential needed to operate the tunnel. In practice a normal shockwave forms inside the diffuser which transitions the flow from supersonic to subsonic velocities. The

subsonic flow then exits the diffuser and enters the muffler to reduce the noise produced by the SHR tunnel to an acceptable level, [39].

3.3.2 SHR Flow Properties

In supersonic flows both the density and velocity change as the cross-sectional area changes, in order to conserve mass. Because of this variation in density and velocity, decreasing the cross-sectional area causes the velocity to decrease and the pressure to increase when the flow is compressible (high subsonic and supersonic). Similarly, increasing the area causes the velocity to increase and the pressure to decrease. This change in properties is exactly the opposite of the change that occurs in incompressible (low subsonic) flows. A great analogy is to relate subsonic flow to water flowing in a river and relate supersonic flow to traffic flow. As water flows down a river its velocity will increase as the river narrows and its velocity will decrease as the river widens, because the water is incompressible and mass must be conserved. As traffic flows down a highway the velocity will increase and density will decrease as the road widens and the velocity will decrease and density will increase as the road narrows, because traffic is a compressible medium, when considering the vehicles and air in-between them.

Equation 3.1 gives the conservation of mass equation for a given cross-section of the SHR tunnel.

$$\rho\, V\, A = \dot{m} \quad (3.1)$$

Where ρ is the gas density, V is the velocity of the flow, and $\dot{m}$ is the mass flow rate through the given cross-sectional area A. Because the tunnel has one inlet and one outlet

the mass flow rate is constant through the entire tunnel. The Mach number is defined as the ratio of the flow velocity to the local speed of sound (a), given by equation 3.2:

$$M = \frac{V}{a} = \frac{V}{\sqrt{\gamma R T_s}} \quad (3.2)$$

Where γ is the ratio of specific heats (γ=1.4 for air, no energy deposition), R is the specific gas constant (R=287 [J Kg^{-1} K^{-1}] for air, no energy deposition), and T_s is the static temperature.

The flow properties of the discharge region of the spark actuator are equal to the static flow properties in the test section, because the test section has constant cross-sectional area. The static pressure (P_s) in the test section is given by the isentropic relation given by equation 3.3, [40].

$$\frac{P_o}{P_s} = \left(1 + \frac{\gamma - 1}{2} M^2\right)^{\frac{\gamma}{\gamma - 1}} \quad (3.3)$$

Where P_o is the stagnation pressure measured in the settling chamber, and held constant for all experiments run; P_o=35psi (241kPa). This stagnation pressure at M=2.2 yields P_s=3.3psi (22.8kPa), compared to the measured value of 3.38psi (23.3kPa). The static temperature (T_s) in the test section is given by the isentropic relation given by equation 3.4, [40].

$$\frac{T_o}{T_s} = 1 + \frac{\gamma - 1}{2} M^2 \quad (3.4)$$

For all experiments run, the stagnation temperature was held at T_o=310K as measured in the settling chamber. This stagnation temperature yields T_s=158 K through equation 3.4, and the static temperature was not measured experimentally in the test section.

3.3.3 Wind Tunnel Infrastructure

The SHR tunnel is supplied compressed air by two CompAir Reavell 5442 compressors that discharge at 17.3MPa. The compressed air is then passed through a Domnick Hunter HDL-500 High Pressure Heatless Regenerative Air Dryer that removes moisture, oil, and other particulates produced by the compressors. The air dryers are necessary because any water will quickly condense because of the large drop in static temperature as the air expands through the nozzle. The compressed air is stored in an A.D. Smith high pressure storage vessel with an internal volume of 23.3m^3 and a maximum operating pressure of 19.3MPa. The dried, compressed air is then heated by a Chromalox 535kW circulation heater to avoid oxygen liquefaction. The heated, dried, compressed air is then regulated down to the desired stagnation pressure and piped to the settling chamber of the SHR tunnel [39]. The mass flow rate through the SHR tunnel is 1.36 [kg s^{-1}]. With this small mass flow rate the SHR tunnel can operate continuously for 25-30 minutes. The variable run time exist because as the pressure in the supply tank drops below 1,000psi the settling chamber pressure is difficult to hold constant and the tunnel will unstart once the tank pressure drops below 600-700psi.

4. ENERGY DEPOSITION MODEL

4.1 Model Overview

To quantify the conversion efficiency of energy from the circuit into the local flow a constant volume heating and expansion model was developed. The volume of the plasma discharge was calculated from the ICCD images. The stored capacitive energy was added to the internal energy of the volume of air contained within the plasma volume to model the impulsive energy deposition process. The now high temperature, high pressure volume of air expands to ambient pressure, where the final volume was calculated and compared to the experimental schlieren images. The description of the model is split into two portions, the thermodynamic properties section and the thermodynamic process section. The thermodynamic properties section calculates the properties of a high temperature air mixture by:

A. Import NASA data for N_2, O_2, N, O and Ar from the Glenn computer Properties and Coefficients (PAC) database valid for temperatures between 200-20,000K.
B. Calculate the equilibrium composition by minimization of the Gibbs function.
C. Calculate the mixture properties by weighting the individual species properties with the calculated equilibrium composition.

The thermodynamic process section models the energy deposition process with four distinct states connected by three thermodynamic processes:

- **State 1:** The static condition of SHR test section.
    - Constant volume energy addition to State 2, increasing the temperature and pressure of the air in the discharge gap.

- **State 2:** High Temperature High Pressure Region.
    - High temperature high pressure region is mixed with varying amounts of ambient air to State 3, simulating heat transfer to the surrounding.
- **State 3:** Mixed High Pressure Region
    - High pressure region is expanded to ambient pressure to State 4, resulting in a low density high temperature region.
- **State 4:** Final High Temperature, Low Density Region.
    - The efficiency of the energy deposition process was estimated by comparing the final expanded volume to the volume calculated from the schlieren images.

All calculations for the energy deposition model were performed with MATLAB, and all code used is available in Appendix A.

4.2 Thermodynamic Properties Model

4.2.1 Energy Transfer and Thermal Equilibration

The actuator's spark discharge transfers the stored electrical energy into the flow via electrons accelerated between the electrodes. These electrons collide with the ions and neutral particles in the plasma transferring their kinetic energy into any of the various energy modes of the particle. The energy however, is not equally distributed between the different modes. The kinetic energy gained by an electron in the discharge gap is characterized by the discharge's reduced electric field (E/n), equation 4.1.

$$\frac{E}{n} = \frac{V_b/L_d}{n_o} \quad (4.1)$$

Where E is the electric field strength given by V_b over distance L_d and n_o is the number density of neutral particles. The reduced electric field is a measure of the mean energy of electrons in a plasma, because an increase in the electric field strength is equivalent to a decrease in the density of the gas.

The electric field strength in the discharge gap of the spark actuator is approximately 8,000 [V cm^{-1}]. This electric field is calculated at breakdown and therefore, is the maximum electric field strength achieved by the spark actuator as it will decrease during the energy deposition process as the voltage across the actuator decreases. The number density of the gas is found from the ideal gas relation using the T_s and P_s, and calculated to be 1.1 x 10^{19} [cm^{-3}]. Therefore, the reduced electric field of the discharge gap, for any capacitor used, is $7x10^{-16}$ [V cm^2]. Using this reduced electric field the fraction of energy transferred by electrons to various energy modes of air is shown in figure 22, [14]. The modified plot from Riazer shows that the majority of the electron's energy excites the vibrational energy modes of N_2, and electronic energy modes of N_2 leading to a non-equilibrium plasma with a temperature distribution of: $T_e > T_{ele} \geq T_{vib} > T_{rot} = T_{trans,\ gas}$. However, in order to increase the overall bulk temperature of the gas the various excited energy modes must be transferred to the translational energy modes of the air particles. The vibrational energy of the air molecules is transferred to the translational energy modes by collisions. The rotational temperature is assumed equal to the gas temperature because the excited rotational modes in a gas are equilibrated after a small

number of collisions, but equilibration of the excited vibrational modes requires approximately 1000 collisions, [41].

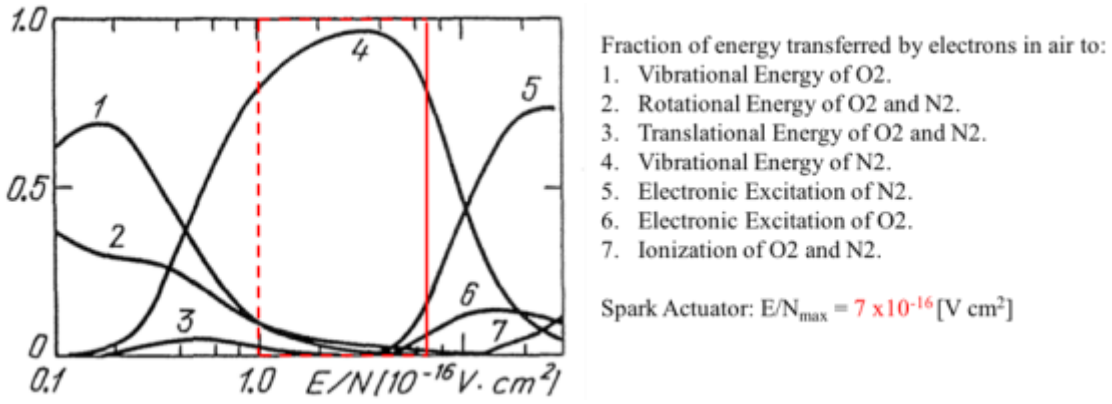

Figure 22. Fraction of energy transferred by electrons to energy modes of air.

Therefore, to model the bulk temperature increase, as an impulsive increase (constant volume) the excited vibrational modes must equilibrate faster than the bulk flow will react. For this equilibration to occurs the collision frequency must be on the order of gigahertz. The collision frequency (ν) is a measure of the average number of collisions per second for a specific type of collision, and is given by equation 4.2 for vibrational to translational collisions (elastic collisions).

$$\upsilon_{elastic} = n_o k = n_o \langle V\sigma \rangle_{elastic} \quad (4.2)$$

Where k is the rate constant equal to the average product of the velocity and collisional cross-section for a vibrational to translational energy transfer ($\sigma_{elastic}$). The thermal equilibrium rate coefficient for internal energy transfer in an N_2-N_2 elastic collision is $1x10^{-16}[m^3\ s^{-1}]$, [41]. Using this rate coefficient, the collision frequency was found to be 1.1GHz. Therefore, thermal equilibration (~1000 collisions) will take less than 1μs.

Similarly, the electrically excited particles will be quenched by collisions, transferring its electrical energy to another mode, or by photon emission, which is responsible for the plasma light production.

4.2.2 NASA Glenn PAC Database

Due to the high temperatures achieved in the discharge region and the non-equilibrium nature of the spark actuator, accurate thermodynamic properties of air at high temperatures (on the order of 10^4K) were required for the energy deposition model.

High temperature thermodynamic properties of an air mixture are not readily available because the composition of the air mixture is also a function of the bulk temperature. Therefore, thermodynamic properties of the constituent species of air from the NASA Glenn computer program for Properties and Coefficients (PAC), [42]. The PAC database contains the library of thermodynamic data used with the NASA Glenn computer program CEA (Chemical Equilibrium with Applications), which calculates chemical equilibrium compositions and properties of complex mixtures. The library contains data for over 2,000 solid, liquid, and gaseous chemical species for temperatures ranging from 200 to 20,000 K. The data is expressed as least-squares coefficients of a seven-term polynomial for the molar specific heat at constant pressure ($\overline{C_p}$) for a given species, equation 4.3:

$$\left.\overline{C_p}(T)\right/_{R_u} = a_1T^{-2} + a_2T^{-1} + a_3 + a_4T + a_5T^2 + a_6T^3 + a_7T^4 \quad (4.3)$$

Where R_u is the universal gas constant, and a_1–a_7 are the coefficients given in the PAC database. The equations for the curve fits of the molar enthalpy ($\bar{h}$) and reference molar

entropy ($\overline{s^o}$, calculated at P^o=101.3kPa) of the given species are obtained by integrating $\overline{C_p}$(T) and $\overline{C_p}$(T)/T , respectively, with respect to the temperature, equations 4.4 & 4.5:

$$\bar{h}(T)\Big/_{R_u T} = -a_1 T^{-2} + \frac{a_2 \ln(T)}{T} + a_3 + \frac{a_4 \mathrm{T}}{2} + \frac{a_5 \mathrm{T}^2}{3} + \frac{a_6 \mathrm{T}^3}{4} + \frac{a_7 \mathrm{T}^4}{5} + \frac{b_1}{T} \quad (4.4)$$

$$\overline{s^o}(T)\Big/_{R_u} = \frac{-a_1 T^{-2}}{2} - a_2 T^{-1} + a_3 \ln(T) + a_4 \mathrm{T} + \frac{a_5 \mathrm{T}^2}{2} + \frac{a_6 \mathrm{T}^3}{3} + \frac{a_7 \mathrm{T}^4}{4} + b_2 \quad (4.5)$$

Where b_1 and b_2 are the integration constant for the $\bar{h}$ and $\overline{s^o}$, respectively, given in the PAC database for the given species.

The PAC database was compiled from a variety of sources, over the past 50 years. The data for the species included in the model (N_2, N, O_2, O, and Ar) was originally obtained from publications by Gurvich, [43]. Experimental observations were used to determine the allowable electronic, vibrational and rotational states. The states that were possible and contributed to the total energy of the molecule were included in the Gurvich model, for the given species. The model for O_2 includes 7 electronic states and all relevant vibrational and rotational levels. The model for N_2 includes 15 electronic states with energies less than 12.4eV, and all relevant vibrational and rotational levels. The models for the three atomic species (O, N, Ar) only included electronic states. The respective models included five electronic states for O, five electronic states for N, and 13 electronic states for Ar.

4.2.3 Chemical Equilibrium

The species included for the energy deposition model were N_2, N, O_2, O, and Ar. The air mixture was assumed to have an initial mole fractions (at T=200K) of:

$$X_{N_2} = 0.78\,,\ X_{O_2} = 0.21\,,\ X_{Ar} = 0.01\,,\ X_N = 0.0\,,\ X_O = 0.0$$

The mole fractions at temperatures greater than 200K were calculated assuming chemical equilibrium at every temperature step for the following global reaction.

$$0.78N_2 + 0.21O_2 + 0.01Ar \rightarrow aN_2 + bO_2 + cN + dO + eAr$$

Where a, b, c, d, e, are the mole of each species at temperature T. The mole fractions of the air mixture at temperature T are then given by, equations 4.6 - 4.10:

$$X_{N_2} = \frac{a}{a+b+c+d+e}, X_{O_2} = \frac{b}{a+b+c+d+e}, X_N = \frac{c}{a+b+c+d+e}$$

$$X_o = \frac{d}{a+b+c+d+e}, X_{Ar} = \frac{e}{a+b+c+d+e} \quad (4.6-4.10)$$

Therefore, the chemical equilibrium calculation results in 5 unknowns (a, b, c, d, e) for each temperature step. The first three equations required to close the system of equations are the atom balances for N, O, and Ar, equations 4.11 - 4.12:

$$N: \ 2(0.78) = 2a + c \ (4.11), \qquad O: \ 2(0.21) = 2b + d \ (4.12),$$

$$Ar: \ 0.01 = e \ (4.13)$$

The remaining two equations required to close the system come from the minimization of the Gibbs free energy for the two following subtractions:

$$N_2 \rightleftharpoons 2N \quad , \quad O_2 \rightleftharpoons 2O$$

The minimization of the Gibbs free energy is calculated in terms of the equilibrium constant (K_p) for each sub reaction, given by equation 4.14 [44]:

$$K_p = \exp\left(\frac{-\Delta\overline{g_T}}{R_u T}\right) = \frac{P}{P^o} \sum_{i=1}^{species} X_i^{(\upsilon_i'' - \upsilon_i')} \quad (4.14)$$

Where X_i is the mole fraction of the i^{th} species, ν_i'' is the moles of products of the i^{th} species, ν_i' is the moles of reactants of the i^{th} species, P is the mixture pressure, P^o is a

reference pressure equal to 101.3kPa, and $\Delta\overline{g_T}$ is the Gibbs function change, given by equation 4.15:

$$\Delta\overline{g_T} = \sum_{i=1}^{species} (v_i'' - v_i')\overline{g_{T,i}} = \sum_{i=1}^{species} (v_i'' - v_i')\left(\overline{h_i} - T\overline{s_i^o}\right) \quad (4.15)$$

Where $\overline{h_i}$ is the molar enthalpy of the i[th] species and $\overline{s_i^o}$ is the molar entropy of the i[th] species, for the given sub reaction. Combining equations 4.14 and 4.15 for the 2 given sub reactions yields the final two equations to close the system, equations 4.16 & 4.17.

$$\frac{P}{P_o}\left(\frac{X_N^2}{X_{N_2}}\right) = exp\left(\frac{\left(\overline{h_{N_2}} - T\overline{s_{N_2}^o}\right) - 2\left(\overline{h_N} - T\overline{s_N^o}\right)}{R_u T}\right) \quad (4.16)$$

$$\frac{P}{P_o}\left(\frac{X_O^2}{X_{O_2}}\right) = exp\left(\frac{\left(\overline{h_{O_2}} - T\overline{s_{O_2}^o}\right) - 2\left(\overline{h_O} - T\overline{s_O^o}\right)}{R_u T}\right) \quad (4.17)$$

Solving the system of equations (4.11-4.13, 4.16-4.17) using the $\overline{h}$ and $\overline{s^o}$ calculated from the PAC database (equations 4.4-4.5) yields the moles of each product (a, b, c, d, e), which are used to find the mole fractions (equations 4.6-4.10), figure 21.

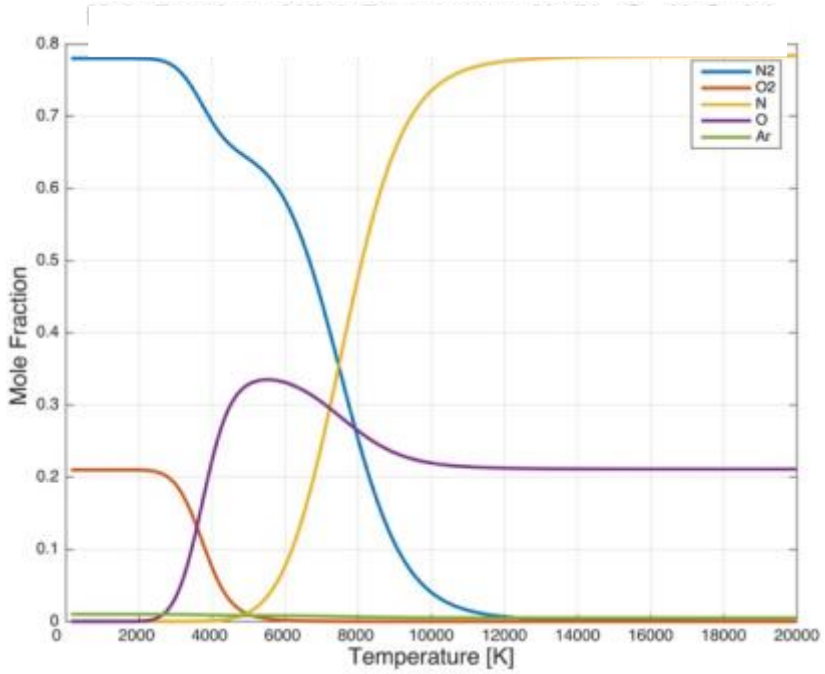

Figure 23. Mole fractions of high temperature air.

The pressure used in the equilibrium mole fraction calculation was found using the ideal gas relationship, and is used in all subsequent sections of the model. The ideal gas relation, in one of its many forms, is given in equation 4.18:

$$Pv = R_{mix}T \quad (4.18)$$

Where P is the pressure, v is the specific volume, R_{mix} is the specific gas constant of the air mixture, and T is the temperature. To insure the validity of the ideal gas model for use in this model, the maximum pressure for the system was calculated and compared to the critical values for O_2 and N_2. The maximum temperatures encountered in this model and their corresponding pressures are listed in table 1. The maximum pressure encountered is large and of the same order as the critical pressure (of N_2 and O_2), but the temperature is two orders of magnitude greater than the critical temperature. The compressibility factor

is between Z=1-1.01, therefore, the high temperature air mixture was assumed to behave as an ideal gas.

Table 1. Maximum temperature and pressure encountered during calculation.

C [pf]	T_{max} [K]	P_{max} [MPa]
100	1817	0.273
1000	3168	0.487
10000	8099	1.901

4.2.4 Thermodynamic Properties of High Temperature Air

The molar enthalpy and entropy of the high temperature air mixture were calculated from the PAC database and the mole fractions for T=200-20,000K, figure 24, 25. The molar specific heat at constant pressure for the high temperature air mixture was calculated from the derivative of $\bar{h}_{mix}$ and directly from the PAC data then weighted using the mole fractions, figure 26. The specific heat was calculated from the derivative of the mixture enthalpy to capture the effects of the changing mixture composition at higher temperatures (dissociation of O_2 and N_2). The molar specific heat at constant volume $\overline{C_v}$, was calculated by subtracting R_U from $\overline{C_p}$, figure 26. Because the composition of the air mixture varies with increasing temperature R_{mix} will also vary with increasing temperature ($R_{mix}(T)$). The specific gas constant was calculated from the mole fractions and the atomic/molecular weights of the species, figure 27. Using $R_{mix}(T)$, the thermodynamic properties of the high temperature air mixture were converted from a molar basis to mass basis, for use in the process portion of the model.

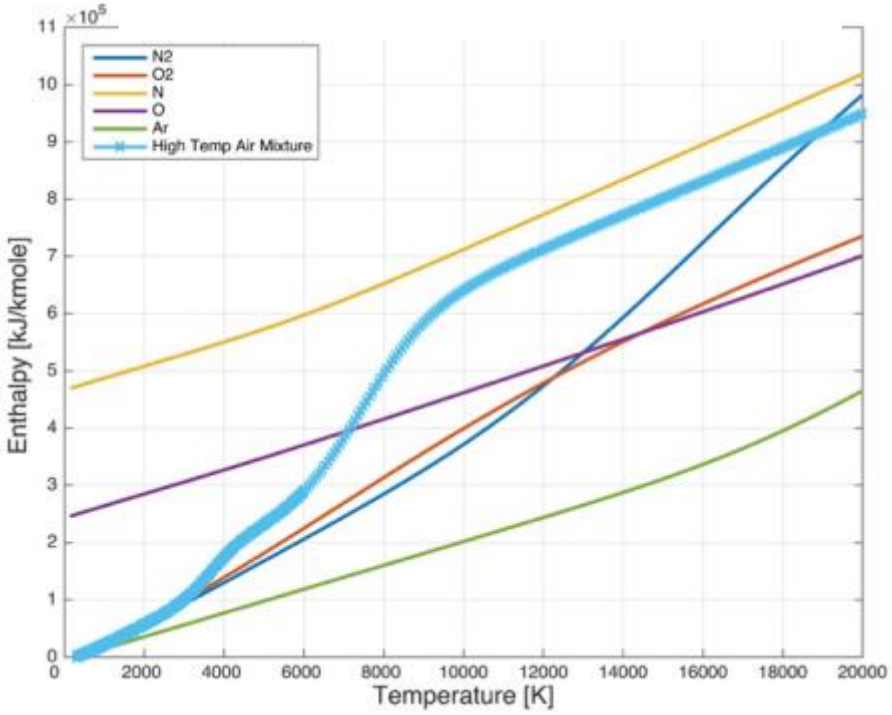

Figure 24. Molar enthalpy of high temperature air and its five species.

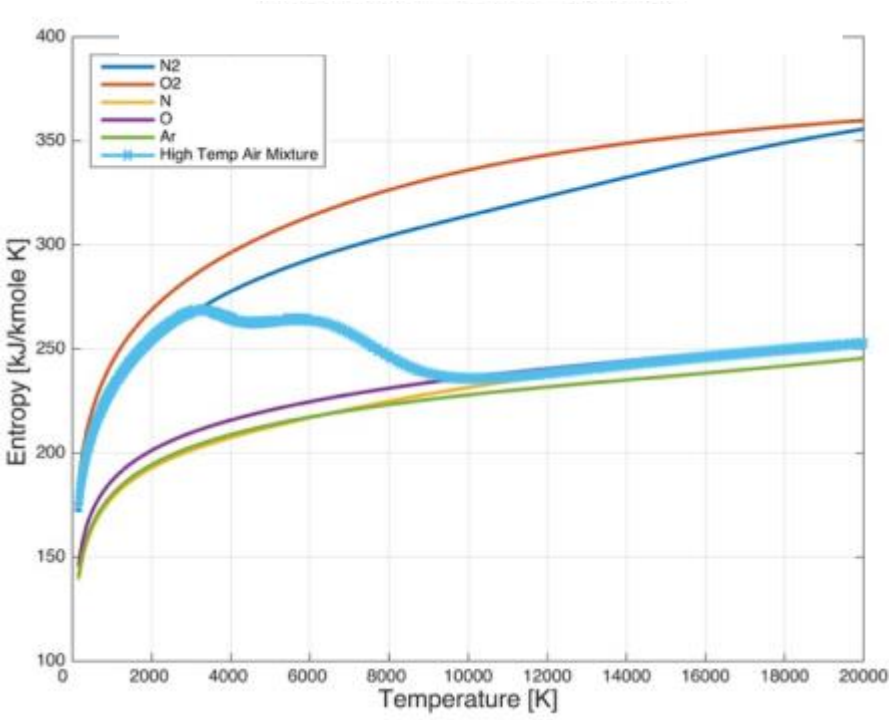

Figure 25. Molar entropy of high temperature air and its five species.

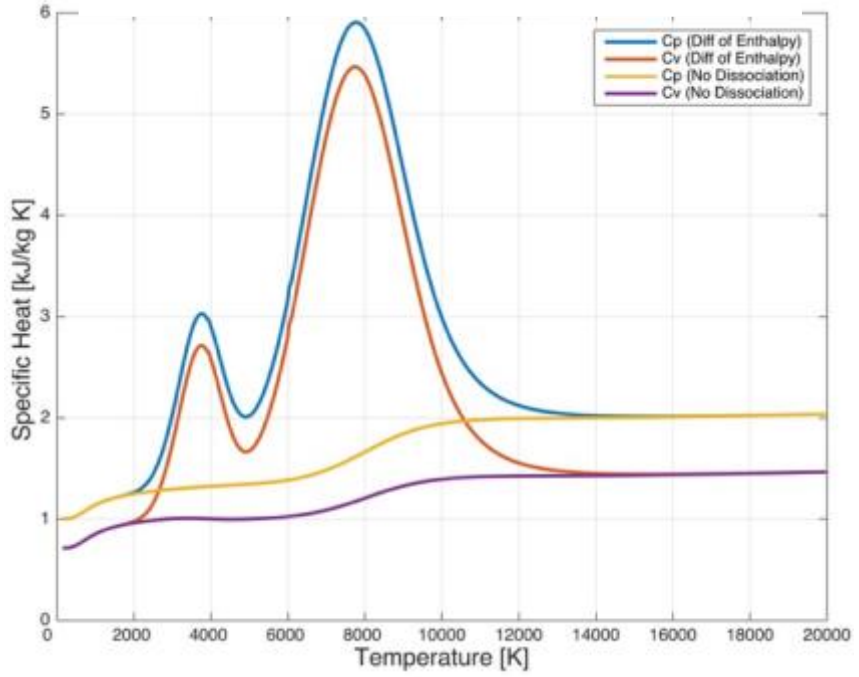

Figure 26. Molar specific heats of the high temperature air mixture.

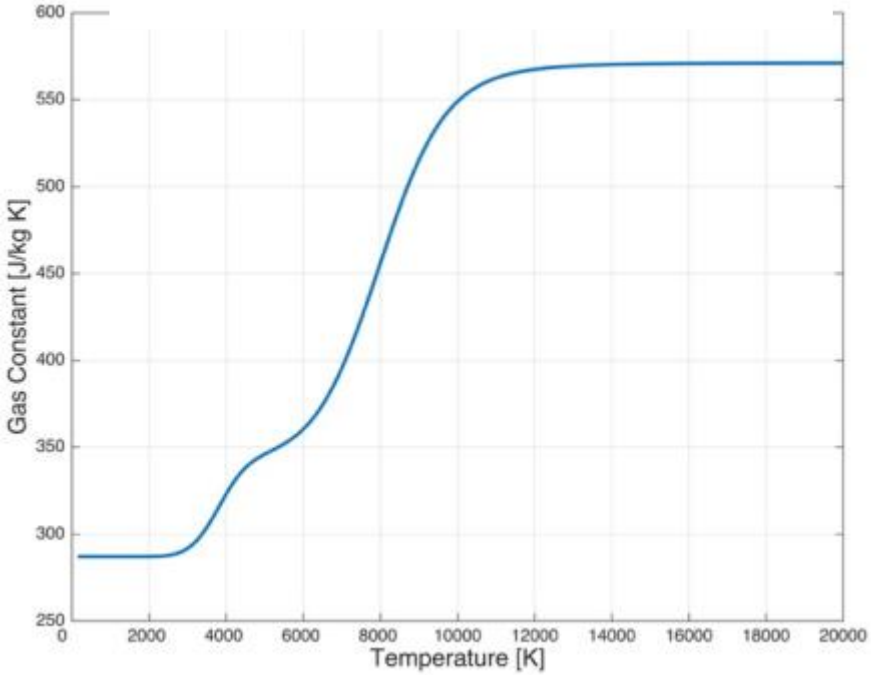

Figure 27. Specific gas constant of the high temperature air mixture.

4.3 Thermodynamic Process Model

4.3.1 Simplified Process Model

The thermodynamic process portion of the model utilizes the thermodynamic properties calculated above to estimate the efficiency of the spark actuator. The simplest version of the process model consists of only three states, not four. State 1 corresponds to the static condition of SHR test section, with an initial volume of air equal to the discharge volume. The electrical energy was deposited at constant volume from state 1 to 2. State 2 corresponds to the high temperature, high pressure volume of air. The volume is then isentropically expanded back to the static pressure of the SHR test section. The T vs. *v* process diagram for the simplified model is shown in figure 28.

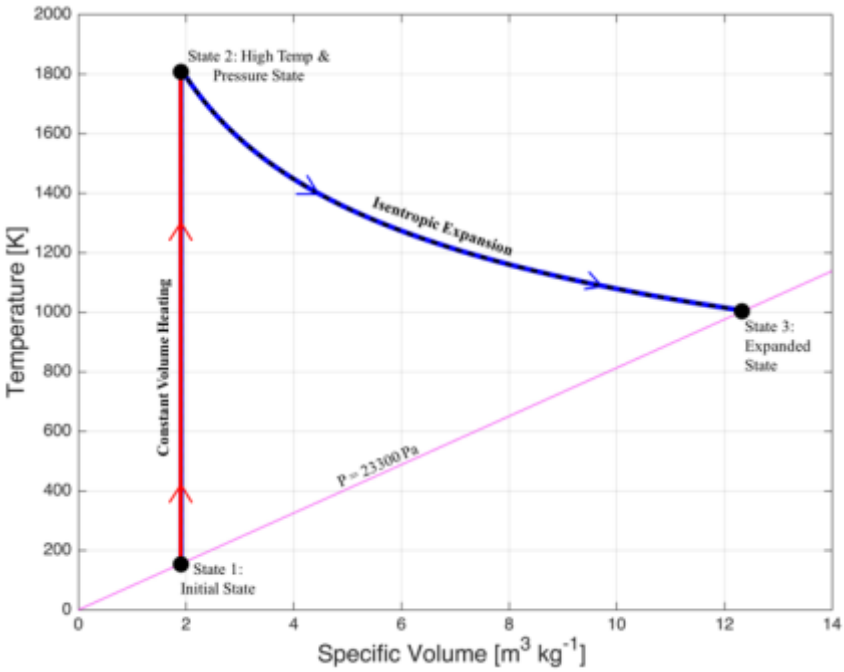

Figure 28. T vs. v diagram for simplified thermodynamic process model, for C=100pF.

The transition from state 1 to 2 models the energy deposition as a constant volume heating process. The constant volume heating assumption was utilized in this portion of the model because of the impulsive nature of the energy addition by the spark actuator. As indicated by the collision frequency, the plasma will equilibrate before the bulk flow can react, creating a large pressure and temperature gradient between the effected volume and the surrounding air. Therefore, the energy added to the given volume of air by the spark actuator was assumed to be added instantaneously. This was accomplished in the model by adding the specific capacitive energy to the total internal energy of the given volume, equation 4.19, first law for a closed adiabatic system.

$$u_2(T_2) = u_1(T_1) + \frac{E_{in}}{m_1} \quad (4.19)$$

Where u_1 and u_2 are the specific internal energy for their respective states, E_{in} is the stored capacitive energy, and m_1 is the mass of the given discharge volume, which is constant during energy addition. The molar internal energy ($\bar{u}$), for use in this portion of the model, was calculated from the definition of enthalpy, equation 4.20:

$$\bar{u}(T) = \bar{h}(T) - pv = \bar{h}(T) - R_u T \quad (4.20)$$

Where $\bar{h}$ is the molar specific enthalpy calculated from the PAC data, and $\bar{u}$ is the molar specific internal energy. The internal energy reduces to a function of temperature only because the enthalpy is a function of temperature only and the ideal gas relation was assumed. The internal energy was calculated for the same temperature range as the PAC data, 200–20,000 K.

With u_2 known the temperature of state 2 was found by interpolation of the specific internal energy data calculated by equation 4.20. Since assuming constant volume energy addition the specific volume of state 2 is equal to the specific volume of state 1 (v_1=v_2). State 2 is completely defined once T_2 and v_2 are calculated.

The transition from state 2 to 3 represents the expansion of the high temperature high pressure volume back to ambient pressure. The expansion process is governed by the second law of thermodynamics, equation 4.21:

$$s(T_3, P_3) - s(T_2, P_2) = \frac{q}{T} + s_{gen} \quad (4.21)$$

Where q is the rate of heat transfer to the surroundings, s_{gen} is the entropy generated during the real process and s is the actual entropy at temperature T and pressure P, calculated from s^o by equation 4.22 and assuming the ideal gas relation.

$$s(T, P) = s^o(T) - R_{mix}(\mathrm{T}) \ln\left(\frac{P}{P^o}\right) \quad (4.22)$$

However, for the simplified version of the model, the expansion was assumed to be isentropic, q and s_{gen} equal zero, simplifying equation 4.21 to equation 4.23:

$$s^o(T_3) = s^o(T_2) + R_{mix}(\mathrm{T}) \ln\left(\frac{P_3}{P_2}\right) \quad (4.23)$$

The temperature of state 3 was then found by interpolation of the $s^o(T)$ function. However, R_{mix} is dependent on the temperature and therefore equation 4.23 and the interpolation were computed and iterated until convergence of T_3 was achieved. With T_3 calculated, state 3 was fully defined since P_3 is equal to P_1, the ambient test section pressure. The final expanded volume was then calculated by multiplying v_4 by m_1, since the mass was constant throughout the simplified model.

4.3.2 Full Thermodynamic Process Model

In order to more accurately model the physical process of the energy deposition and subsequent expansion, an intermediate state, between state 2 and 3, was added to the model, to estimate the heat transfer and associated irreversibilities from the high temperature region to the surroundings. From state 2 of the simplified model, the high temperature high pressure region is mixed with a given amount of ambient air to reach the new state 3. The mixed hot region is then isentropically expanded to ambient pressure, state 4. The temperature vs. specific volume process diagram for the full heating expansion model with four states is shown in figure 29.

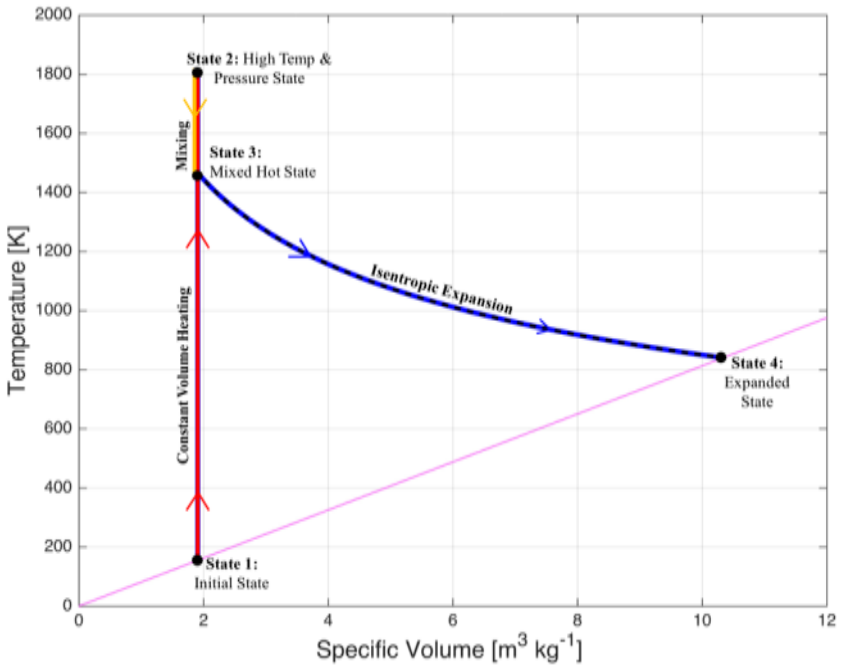

Figure 29. Temperature vs specific volume process diagram for entire process model.

The transition from state 1 to 2 is still modeled as a constant volume heating process for the full model as it was in the simplified model, because the process is a good

approximation of the energy deposition process. The transition from state 2 to the new state 3 models the mixing as a closed system constant volume process as shown in figure 30. The mixing is assumed to occur with no heat transfer or work to/from the system (closed system) and therefore the energy balance of the mixing process is given by equation 4.24:

$$u_3 = \frac{m_2 u_2 + m_a u_a}{m_3} \quad (4.24)$$

Where u_3 is the internal energy of the mixed hot state, m_a and u_a are the mass and internal energy of the ambient gas that are being mixed, respectively. From the continuity equation m_3 is equal to the sum of m_2 and m_a. The thermodynamic properties of the ambient air mixed with the high temperature region are the same as state 1 and therefore all three states (1, 2, and 3) have the same specific volume. The transition from state 3 to 4 represents the expansion of the mixed hot state to ambient pressure, and is modeled the same as it was in the simplified process model.

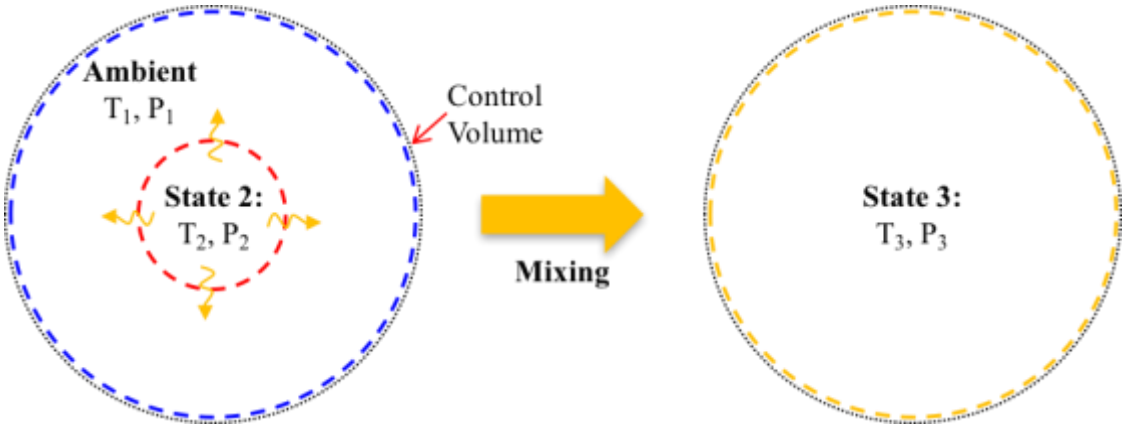

Figure 30. Diagram of constant volume mixing process.

The full thermodynamic process model performs the mixing before the expansion (state 3a) as opposed to expansion then mixing (state 3b) because the former is less efficient, figure 31. The less efficient representation of heat transfer method was chosen because it represents the worst-case scenario and will result in a conservative estimation of the spark actuator's efficiency. An approximation of the real heating and expansion processes of the spark actuator is included, green curve figure 31.

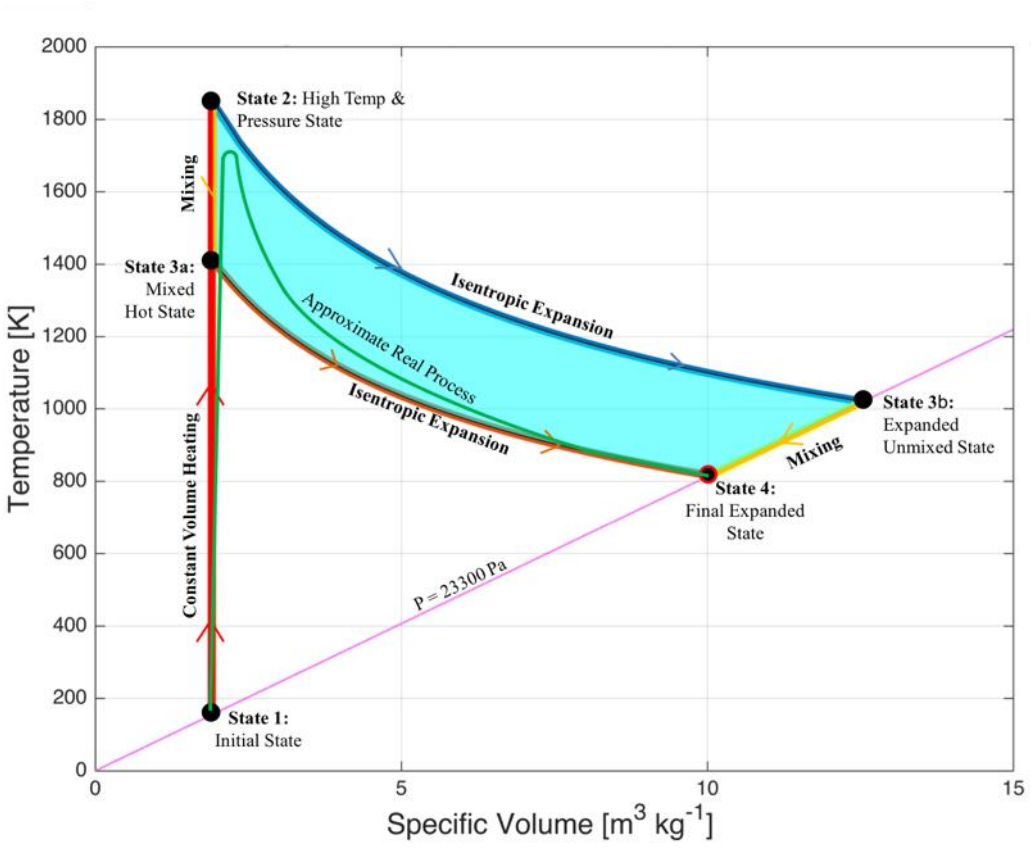

Figure 31. T vs. v diagram, two paths from state 2 to state 4, and approximate real process.

To compare the full process model to the experimental images a set of all possible solutions were produced by varying two parameters:

1. The percentage of electrical energy that is transferred to the flow (η_{12}).
2. The amount of ambient air mixed with the state 2.

The percentage of capacitor's energy (E_c) that is transferred to the flow was termed the efficiency of the spark actuator because it is the fraction of electrical energy (E_{in}) that is transferred into thermal energy in the flow. The amount of ambient air mixed with the high temperature high pressure region (m_a) is defined as the mixing factor (k), equation 4.25:

$$m_a = (k-1)m_2 \quad (4.25)$$

Where m_2 is the mass of the high temperature high pressure region. Combining equation 4.25 with the continuity equation results in the simple relation for m_3 in terms of k, equation 4.26:

$$m_3 = k\, m_2 \quad (4.26)$$

Therefore, k=1 represents the case where no ambient air is mixed with the heated region and the results of the full model will equal the simplified model. A mixing factor of 2 represents the case where equal amounts of heated air and ambient air are mixed. The efficiency was varied from 0% to 100% and the mixing factor was varied from 1 to an upper bound defined from the experimental results presented in section 5 to create a surface of solution. Because the mixing factor is arbitrary and cannot be directly compared to the experimental images a bubble expansion ratio (BER) was defined to allow easier comparison to the experimental results, equation 4.27:

$$BER = \frac{\nu_4}{\nu_3} \quad (4.27)$$

Where v_3 and v_4 are the specific volumes of the mixed state and the expanded state, respectively. The experimental results place an upper and lower bound on the BER, narrowing the range of possible efficiencies of the spark actuator. Thousands of solutions were calculated using the model by varying the efficiency and mixing factor. For each efficiency, only a single mixing factor matched the experimental results, but a large range was used because the specific mixing factor was not known. It was easier to implement the model thousands of times than solve the inverse problem, working backwards from state 4 to state 1. The surface of thermodynamically possible solutions for C=100pF is shown in figure 32. From the experimental results this surface was reduced.

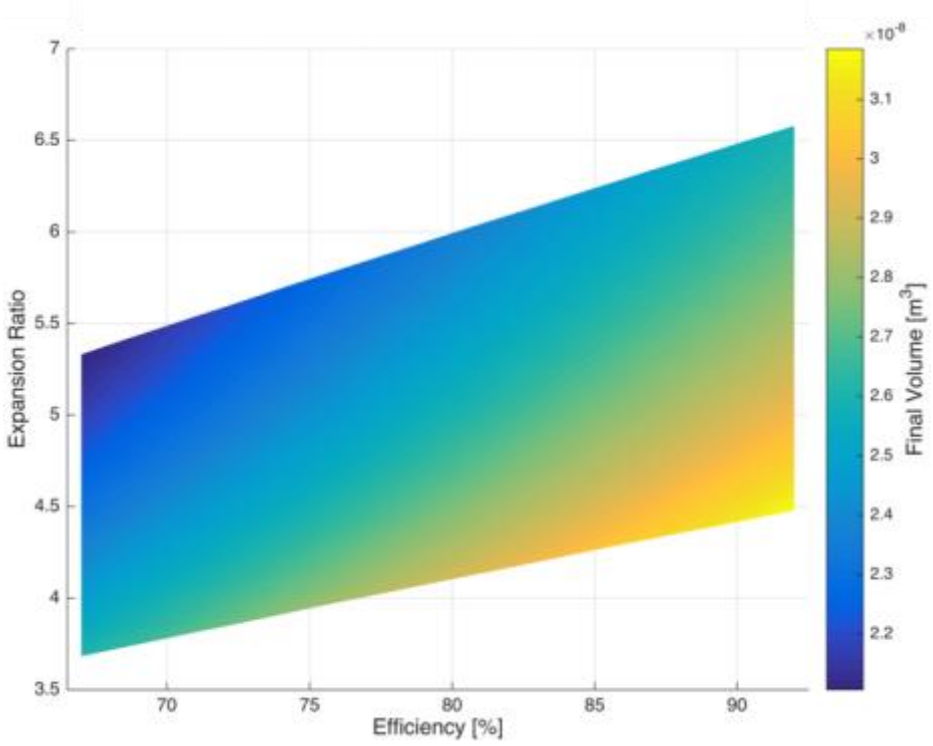

Figure 32. Efficiency vs BER with surface of possible solution for C=100pF, *k*=1-1.8.

5. RESULTS

5.1 Experimental Results

5.1.1 Electrical Energy Results

The electrical energy stored in the capacitor by the RC circuit was calculated two different ways:

1. Integration of the instantaneous power with respect to time, equation 5.1. The instantaneous power was calculated by the product of the instantaneous voltage (V(t)) and current (I(t)) of the spark actuator.

$$E_c = \int V(t)I(t)dt \quad (5.1)$$

2. Calculation of the total stored energy in the capacitor at breakdown, equation 5.2:

$$E_c = \frac{1}{2}CV_b^2 \quad (5.2)$$

Where C is the total capacitance of the circuit common to the anode.

The instantaneous current through the spark actuator, used in method 1, is difficult to measure accurately and two methods were required to the measure the current from the three capacitors. First, it was calculated by measuring the voltage drop across a shunt resistor and dividing by the resistance of the shunt. This current measurement method worked well for the 100 and 1,000pF cases but the 10,000pF case over powered the shunt resistor used in this experiment. Second, the instantaneous current was measured by a current transformer. This measurement method was only used on the 10,000pF case.

The breakdown voltage was calculated as the maximum instantaneous voltage for every voltage trace recorded, and is independent of the capacitor in the circuit. As shown in section 2.1.2 the breakdown voltage is only dependent on the gas pressure and the discharge gap length, both of which were held constant for the experiments. A total of 64 voltage traces were recorded during all the experiments ran. The mean breakdown voltage across the spark actuator was found to be 6,200±400V. The large interval of the mean voltage is typical of a spark discharge because small variations in the static pressure are present in the tunnel between discharges and the actual discharge length varies each event.

To accurately calculate the energy, the total system capacitance is required. The total capacitance of the circuit includes the capacitor, and all conductive material common to the capacitor including voltage probes. The total capacitance of the circuit was measured using a Amprobe meter, and found to be C=179pF, C=1,081pF and C=10,560pF, for the nominal 100pF, 1000pF, and 10000pF cases respectively.

The average stored electrical energy using method 1 for the 100pF case was found to be 8.0mJ. A single representative voltage/current trace calculating the voltage for the 100pF case using method 1 is shown in figure 33. The average stored electrical energy using method 1 for the 1,000pF case was found to be 28.6mJ. A single representative voltage/current trace calculating the voltage for the 1,000pF case using method 1 is shown in figure 34. The average stored electrical energy using method 1 for the 10,000pF case, with the current measured by the transformer, was found to be 144mJ. A single representative voltage/current trace calculating the voltage for the 10,000pF case using method 1 is shown in figure 33.

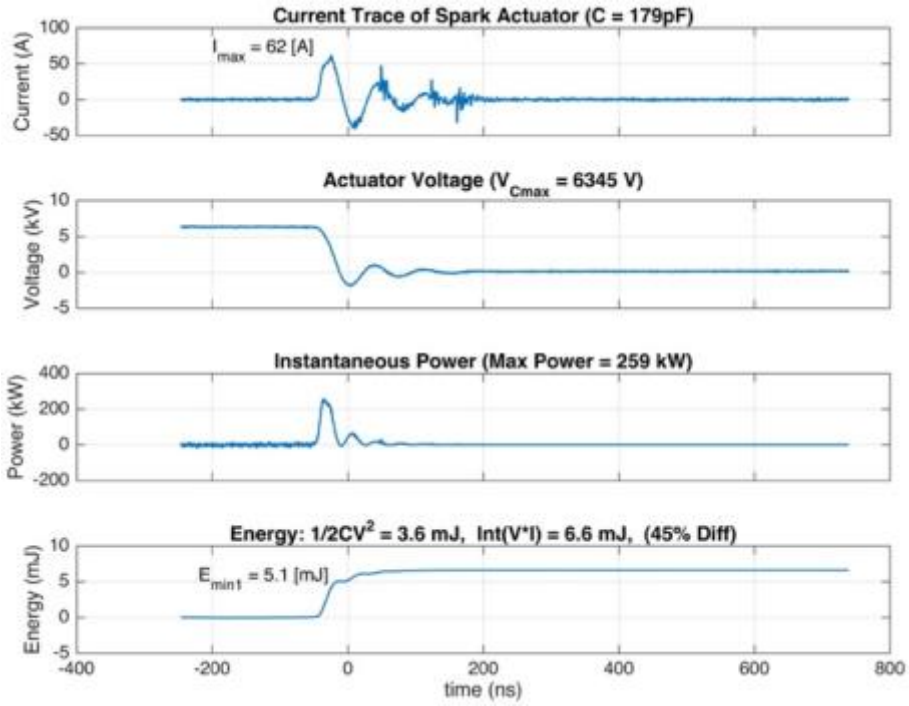

Figure 33. V/I trace with calculated power and energy for C=179pF.

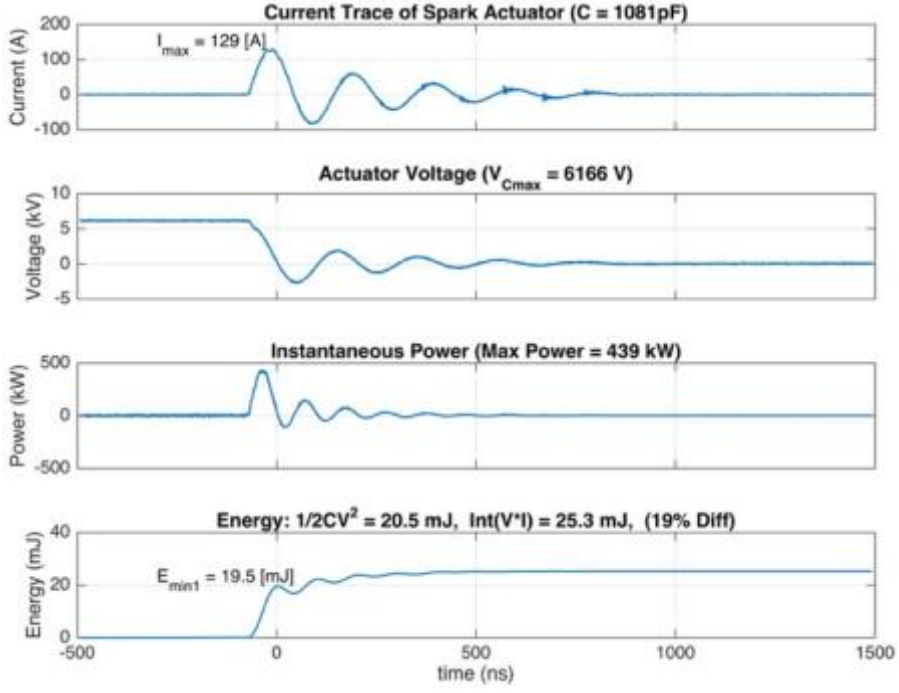

Figure 34. V/I trace with calculated power and energy for C=1,081pF.

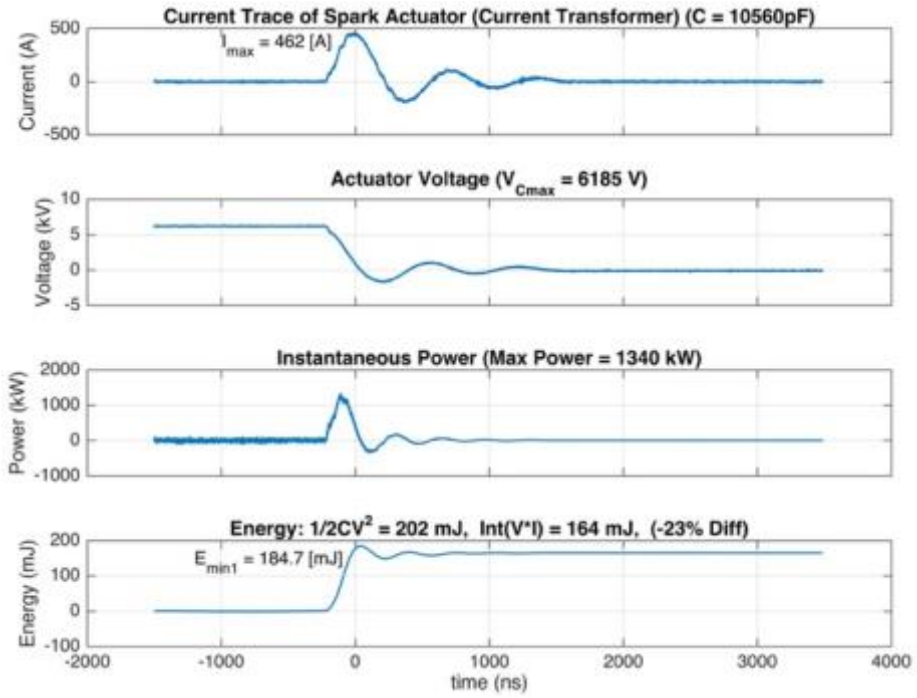

Figure 35. V/I trace with calculated power and energy for C=10,560pF.

Since the instantaneous current was difficult to measure accurately and reliably and two different current measurement techniques were required, method 2 was used to calculate the stored electrical energy for use in the thermodynamic model. The average energy for each capacitor was calculated from equation 5.2 using $V_{b,mean}$ and the total circuit capacitances, table 2:

Table 2. Stored electrical energy calculated by method 2 using $V_{b,mean}$

Nominal Capacitance		100 pF	1000 pF	10000 pF
Total Capacitance		179 pF	1081 pF	10,560 pF
$V_{b,mean}$	6200 V	3.4 mJ	20.8 mJ	203 mJ
$V_{b,m} - 2\sigma$	5800 V	3.0 mJ	18.0 mJ	176 mJ
$V_{b,m} + 2\sigma$	6600 V	3.9 mJ	23.7 mJ	232 mJ

5.1.2 Discharge Volume Results

The discharge volume used in the constant volume heating portion of the model is equal to the plasma filament volume. The plasma filament volume was calculated from the ICCD direct imaging of the discharge, and calibrated to 576 pixels per inch. Figure 36 is a representative image of a plasma discharge with C=10,000pF, and includes two separate filaments. For size reference the inner electrode spacing is 7.6mm. The volume of each filament was calculated assuming a sweeping cylinder shape using the measured diameter and length of each filament. The volume of each filament was summed up to find the total discharge volume for a given image. The discharge in figure 36 has two filaments with a volume of 0.65 and 0.87mm^3 giving a total discharge volume of 1.52mm^3.

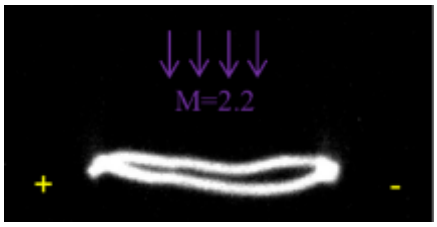

Figure 36. Plasma discharge for C=10,560pF, 5ns exposure at 100ns from discharge.

The discharge volume was calculated and averaged across twenty images for each capacitance. The images for C=10,560pF had one or two distinct filaments, figure 37. The average discharge volume for C=10,560pF was calculated to be 1.69mm^3. The plasma discharge for C=1,081pF had between one and three distinct filaments, figure 38. The average discharge volume for C=1,081pF was calculated to be 3.21mm^3. The images for C=179pF indicated a more diffuse spark discharge rather than a discharge with distinct filaments, figure 39, as seen in the 1,081 and 10,560pF images. Therefore, the discharge

volume was calculated as a single sweeping cylinder with a single effective diameter and length. The average discharge volume for C=179pF was calculated to be 3.96mm^3. The C=10,560pF case not only deposited more energy but did so in a smaller volume giving it the highest energy density of 120.1 [mJ/mm^3]. The C=1081pF case had an energy density of 6.5 [mJ/mm^3] and the C=179pF case had an energy density of 0.86 [mJ/mm^3].

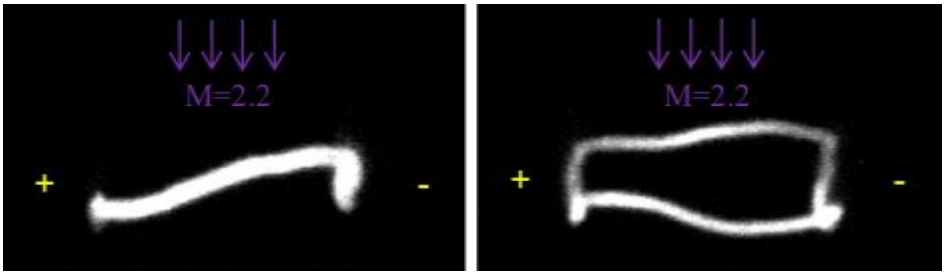

Figure 37. Images of plasma discharge for C=10,560pF, 5ns exposure at 100ns from discharge.

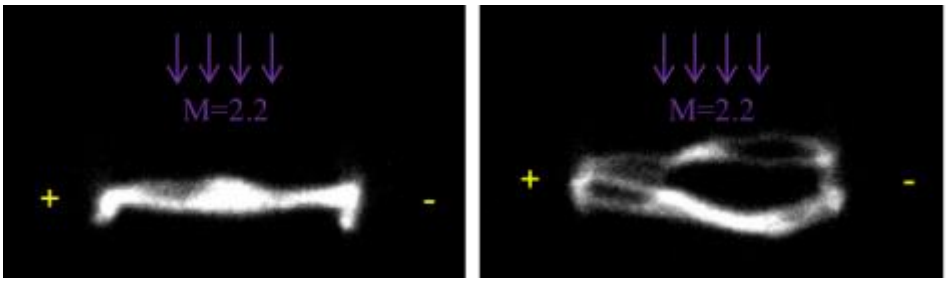

Figure 38. Images of plasma discharge for C=1,081pF, 5ns exposure at 100ns from discharge.

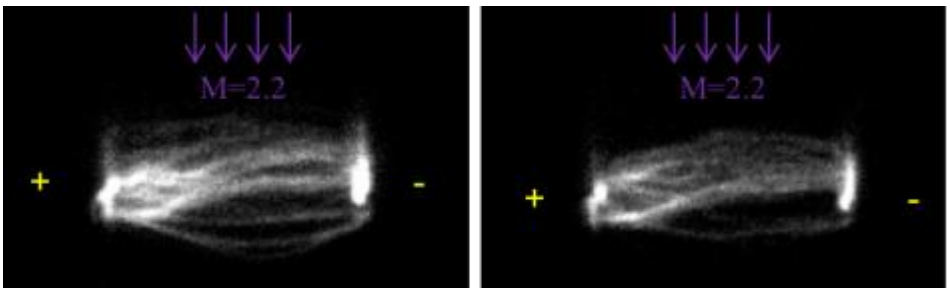

Figure 39. Images of plasma discharge for C=179pF, 5ns exposure at 100ns from discharge.

5.1.3 Schlieren Images

The time evolution of the expanding high temperature high pressure region was imaged using the schlieren setup. From these images the volume of the expanding region volume was measured as a function of time since discharge. The schlieren images only give a side view of the expanding region and therefore only the cross-sectional area of the expanding region can be measured. However, the filament length is much greater than the diameter and will expand much more in the radial direction than it will in the cross-flow direction.

Due to the statistical nature of the plasma discharge not every event will appear the same in the schlieren images. Therefore, approximately 500 images were acquired for every time delay (5.6, 10, 15, 20, 25, 30, 35, 40, 45, 50, 55μs) and for every capacitor (179, 1,081, and 10,560pF). The cross-sectional area of the expanding region was calculated using the ImageJ software. The area, in square pixels, was measured by tracing around the amorphous region, figure 40. The area was then converted using the schlieren image calibration equal to 771 pixels per inch. The area of the expanding region was measured for each individual image taken. The areas measured were averaged for each time delay resulting in an average expanded volume as a function of time since discharge. A series of averaged images were also created but are used only for display purposes, because the area measured in the average image is always larger than the individual images. The expanding region appears larger in the averaged image because the region is

not in the same location for the same delay time due to the jitter of the triggering system (±100ns) and discharge location.

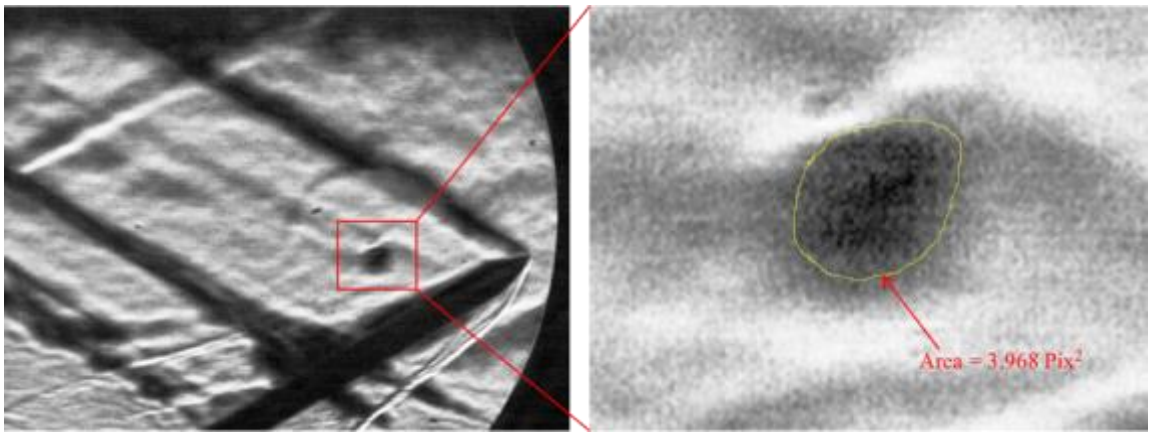

Figure 40. Expanding region area calculation (individual image) for C=179pF, t_{delay}=25μs.

The expanding region for C=179pF reaches a steady final size at t=25-30μs. The averaged final expanded cross-sectional area for C=179pF was found to be 3.4mm^2, figure 41. The expanded region is not visible after 45μs because it leaves the undisturbed region and collides with the coalescing floor shock. A time evolving series of averaged images (display only) for C=179pF is shown in figure 42. The error bars figure 41, 43, 44 are based on the standard deviation of the multiple images analyzed for the particular delay and capacitance.

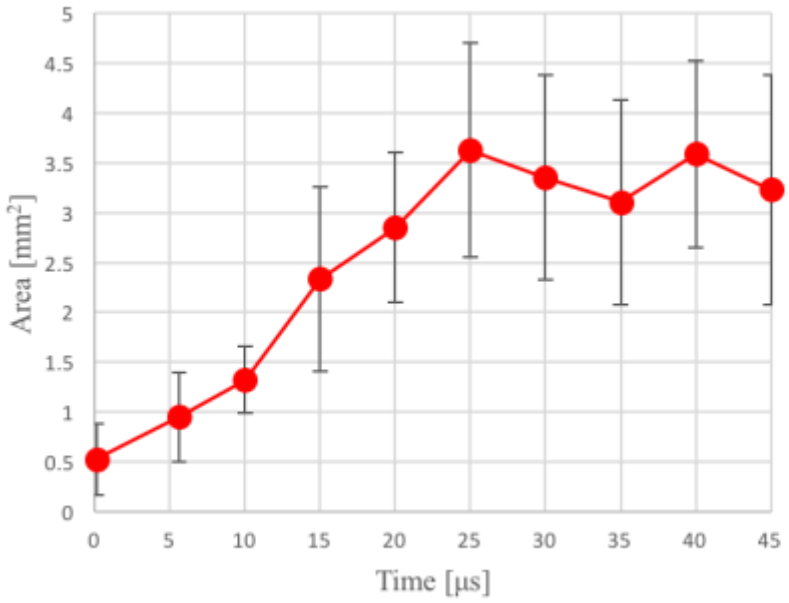

Delay [µs]	Area [mm²]
0.1	0.53
5.6	0.95
10	1.26
15	2.34
20	2.85
25	3.63
30	3.35
35	3.11
40	3.59
45	3.23
50	Not Visible
55	Not Visible

Figure 41. Area of expanding region as a function of time, for C=179pF.

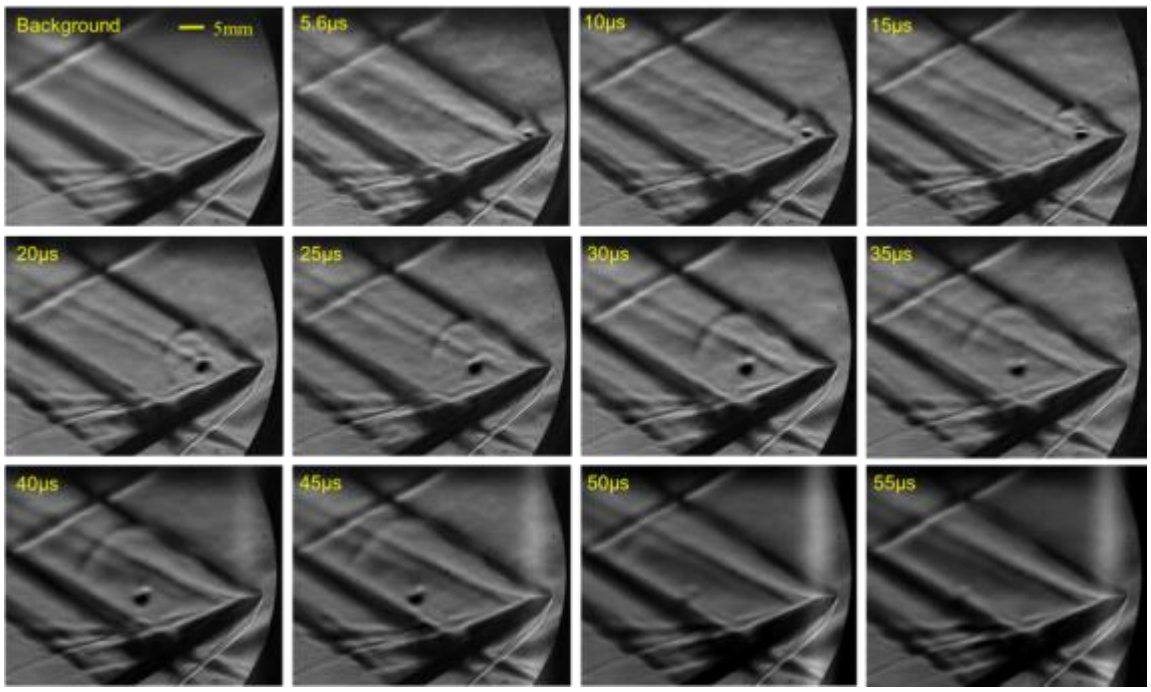

Figure 42. Time evolution of expanding region (averaged images), for C=179pF.

Along with the size and expansion rate of the effected region the flow velocity was calculated from the schlieren images. The flow velocity, the velocity the effected region travels downstream, was calculated by dividing the distance the region traveled downstream by the time delay. The distance was measured from the discharge location to the center of the effected region. The average velocity of the effected region was found to be 600 [m/s] for C=100pF, figure 43. Using the static test-section temperature the speed of sound is approximately 252 [m/s]. The SHR tunnel operates at M=2.2 resulting in a theoretical flow velocity of 554 [m/s]. The difference in the measured velocity and the theoretical velocity is most likely due to variations in the static temperature or Mach number in the test-section.

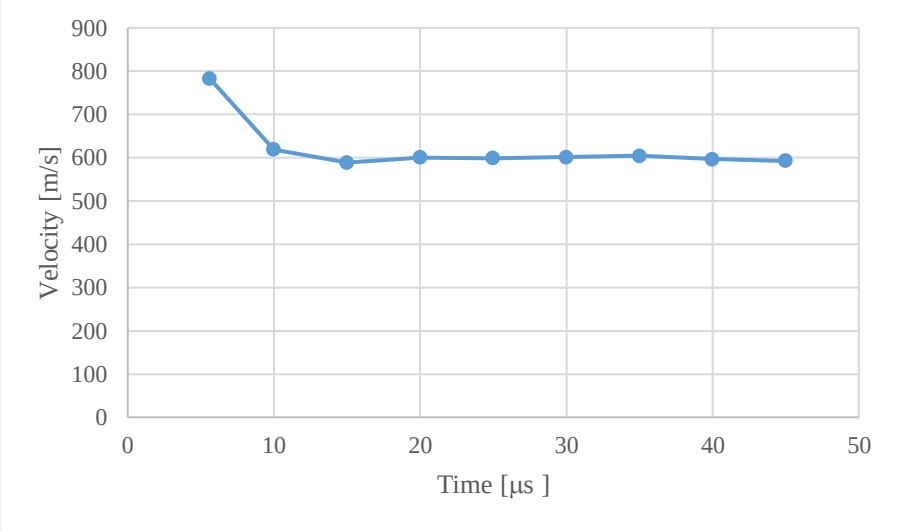

Figure 43. Velocity of affected region for C=100pF.

The expanding region for C=1,081pF and 10,560pF is not as well defined as the C=179pF for a combination of reasons. The images taken at early delays were obscured by the plasma light. The expanding region departed the undisturbed region of the test-section for images with delays greater than 35μs. The averaged final expanded cross-sectional area for C=1,081pF was estimated to be 5mm^2, figure 44. The averaged final expanded cross-sectional area for C=10,560pF was estimated to be 14mm^2, figure 45. A time evolving series of averaged images for both C=1,081pF and 10,560pF is shown in figure 46. Additional images for all three input energies are available in Appendix B.

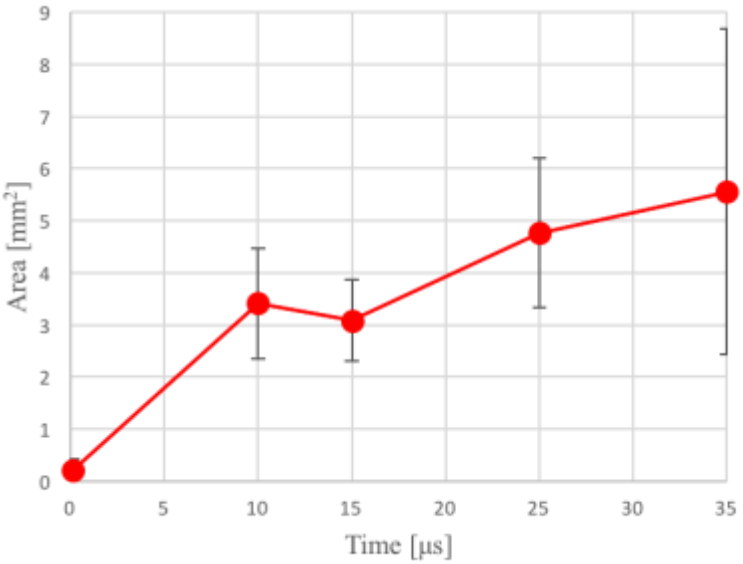

Delay [μs]	Area [mm^2]
0.1	0.21
5.6	Not Visible
10	3.41
15	3.08
20	Not Visible
25	4.76
30	Not Visible
35	5.56
40	Not Visible
45	Not Visible
50	Not Visible
55	Not Visible

Figure 44. Area of expanding region as a function of time, for C=1,081pF.

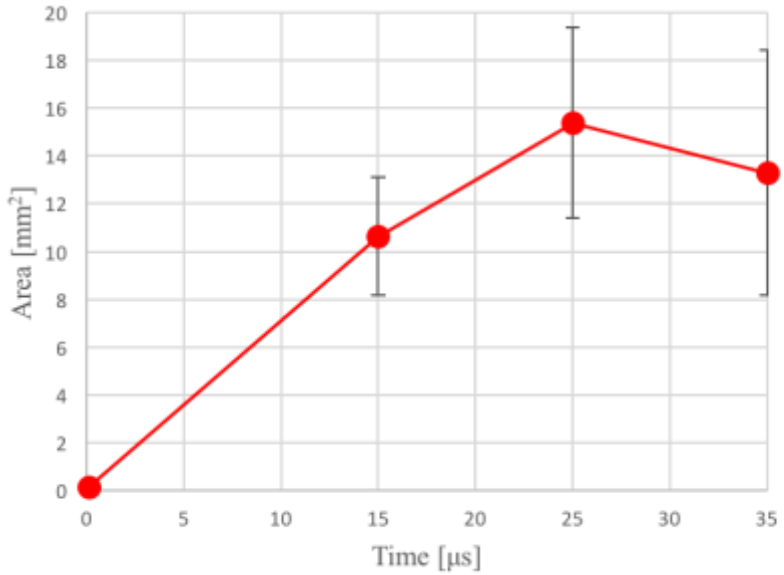

Delay [us]	Area [mm^2]
0.1	0.14
5.6	Not Visible
10	Not Visible
15	10.64
20	Not Visible
25	15.38
30	Not Visible
35	13.29
40	Not Visible
45	Not Visible
50	Not Visible
55	Not Visible

Figure 45. Area of expanding region as a function of time, for C=10,560pF.

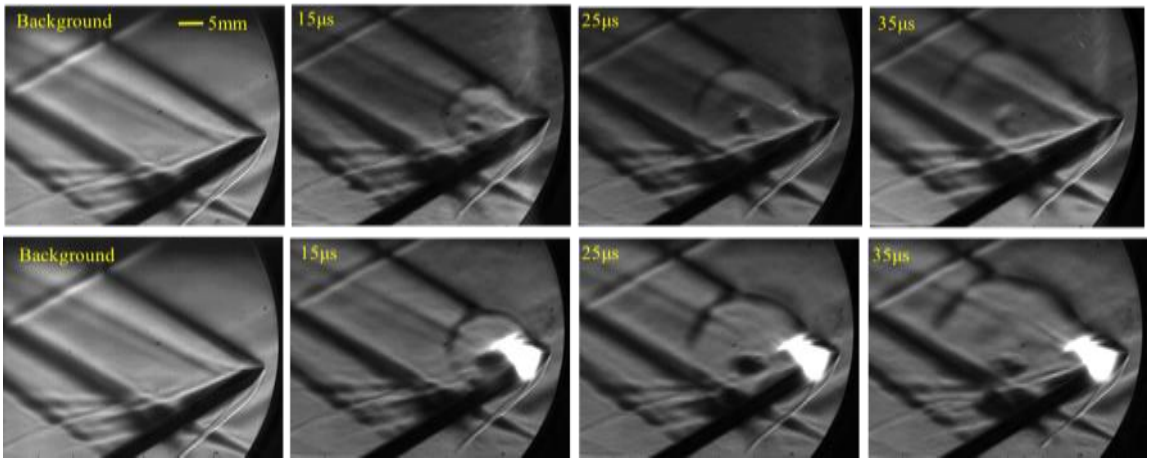

Figure 46. Time evolution of expanding region (averaged images), for C=1,081pF(upper) and C=10,560(lower)

5.2 Thermodynamic Process Model Results

The initial discharge volume calculated in section 5.1.2 along with the static conditions of the SHR test section were used as the initial conditions of state 1 in the process model. The model produces a surface of thermodynamically possible solutions for a given capacitance as a function of efficiency and BER, as shown in figure 32 for C=179pF. The final expanded volume and the BER were used to narrow down the possible solutions. The final expanded volume, calculated from the final expanded area found in section 5.1.3 assuming a constant length, resulted in a line of solutions. The line of solutions on the η vs. BER surface represents a line of constant volume corresponding to the experimental measured final volume. Each point on the constant volume line represent a possible actuator efficiency at a given BER.

Not only was the final expanded area measured from the schlieren images but so was the rate of expansion. This allowed for a maximum and minimum BER to be defined. The maximum BER was defined as the ratio of the final expanded area over the cross-sectional area of the plasma filament, table 3. The minimum BER was defined as the ratio of the final expanded area over the area of the expanding region at the smallest time delay possible ($t_{d,min}$=5.6μs for C=179pF, $t_{d,min}$=10μs for C=1,081 and $t_{d,min}$=15μs for C=10,560pF), table 3. The maximum and minimum BER defined an upper and lower limit, respectively, for the line of solutions.

Table 3. Experimental parameters for process model, from experiment.

Capacitance [pF]	Final Volume [mm^3]	BER_{min}	BER_{max}
179	26	3.8	6.9
1081	38	1.8	26.9
10560	107	2.0	108.0

5.2.1 Model Results for C=100pF

The surface of possible solutions and the line of constant volume limited by the maximum and minimum BER for C=179pF is shown in figure 47. The possible efficiencies for the C=179pF range from 67% to 92%. The solution for larger efficiencies correspond to smaller mixing factors, and vice versa. For the final volume to equal 25.9mm^3 at η_{12}=92%, the mixing factor must equal 1.0 (no mixing). At the opposite end, for η_{12}=67% the mixing factor must equal 1.8 in order for the final volume to equal 25.9mm^3. The efficiency range for C=179pF is well defined because the minimum BER is known at early time delays (t_{delay}<10μs). The minimum BER is not as well defined for C=1,081 and 10,560pF because the schlieren images were obscured by the plasma light and the volume of the expanding region could not be calculated at the early time delays.

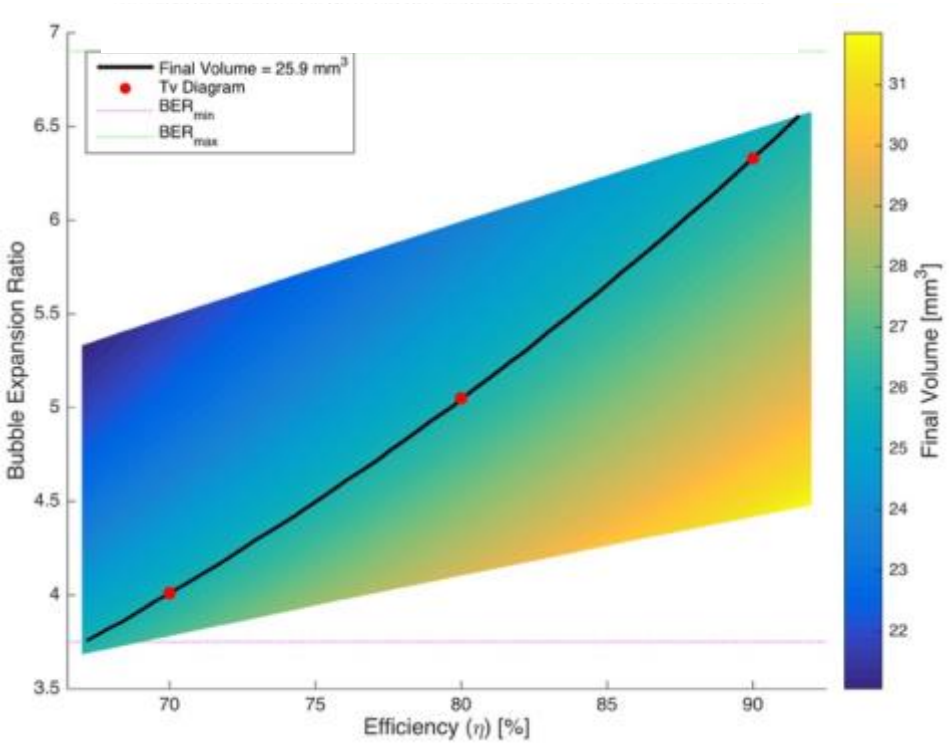

Figure 47. Surface of thermodynamically allowable solutions, with line of constant volume for C=179pF.

Tv diagrams corresponding to solutions at η_{12}=70% and η_{12}=90% for C=179pF are used to investigate the effect the bounding BER has on the range of possible efficiencies. The solution for η_{12}=70% has a BER of 4.0 corresponding to a *k*=1.64, figure 48. This solution reaches a maximum temperature of 1487K and expands to a final density of 0.132 [kg m^{-3}] and temperature of 620K. The BER is on the low side of the experimental range indicating a decent amount of mixing/heat transfer with the ambient air. The solution for η_{12}=90% has a BER of 6.3 corresponding to a *k*=1.02, figure 49. A maximum temperature of 1817K was reached for this solution and expanded to a final density of

0.082 [kg m^{-3}] and temperature of 991K. The BER is on the upper end of the range indicating almost no mixing/heat transfer with the surroundings.

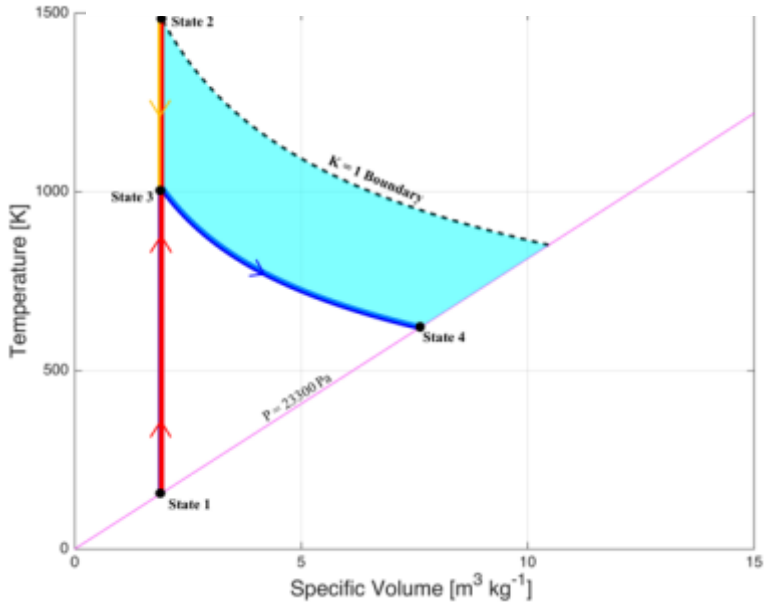

Figure 48. Tv process diagram for C=179pF at η_{12}=70%, *k*=1.64.

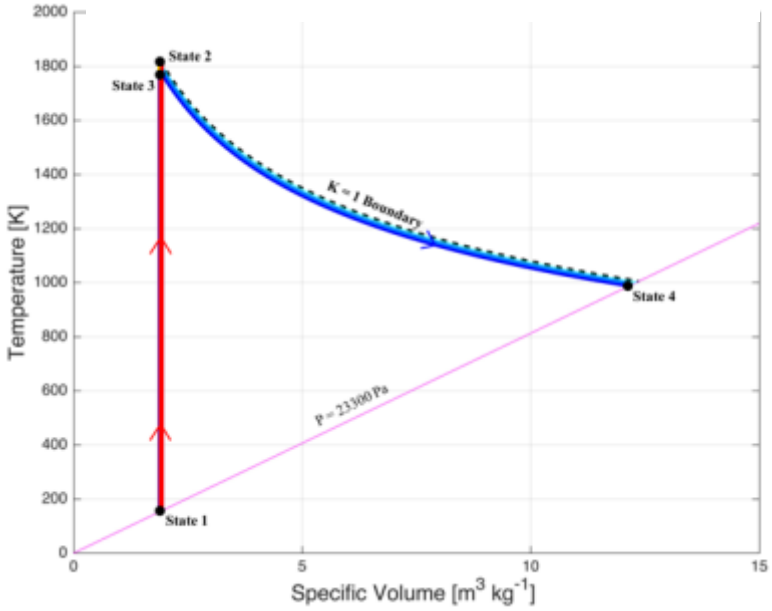

Figure 49. Tv process diagram for C=179pF at η_{12}=90%, *k*=1.02.

These two solutions represent the relative extremes of the possible efficiencies and the actual solution would probably exist somewhere in-between. The solution for η_{12}=80% would be right in the middle with a BER of 5.1 corresponding to a *k*=1.31, figure 50. This median solution reaches a maximum temperature of 1653K and expands to a final density of 0.104 [kg m^{-3}] and temperature of 778K. The state variables are given in table 4.

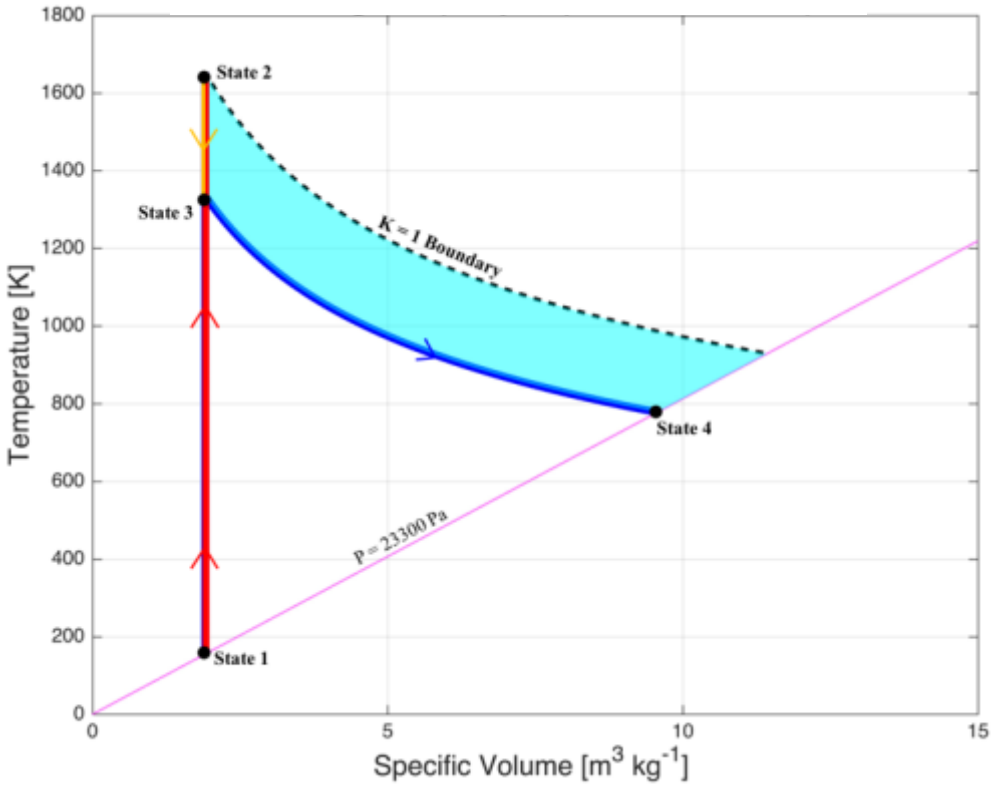

Figure 50. Tv process diagram for C=179pF at η_{12}=80%, *k*=1.31.

Table 4. State variables for C=179pf at η_{12}=80%, *k*=1.31.

State	T [K]	P [kPa]	u [J kg^{-1} K^{-1}]	s [J $kg^{-1}K^{-1}$]	*v* [m^3 kg^{-1}]	R [kJ kg^{-1} K^{-1}]
1	155	23.3	1255	6458	1.91	287
2	1653	248.9	$1.05x10^6$	8305	1.91	287
3	1336	201.0	$7.56 x10^5$	8109	1.91	287
4	778	23.3	$2.76 x10^5$	8109	9.57	287

5.2.2 Model Results for C=1,000pF

The surface of possible solutions and line of constant volume for C=1,081pF is shown in figure 51. The possible efficiencies limited by the max and min BER range from 8.1% to 29.2%. The solution for η_{12}=10% is representative of the lower efficiency limit and has a BER of 2.1 corresponding to a *k*=5.64, figure 52. This solution reaches a maximum temperature of 1,567K and expands to a final density of 0.25 [kg m^{-3}] and temperature of 327K.

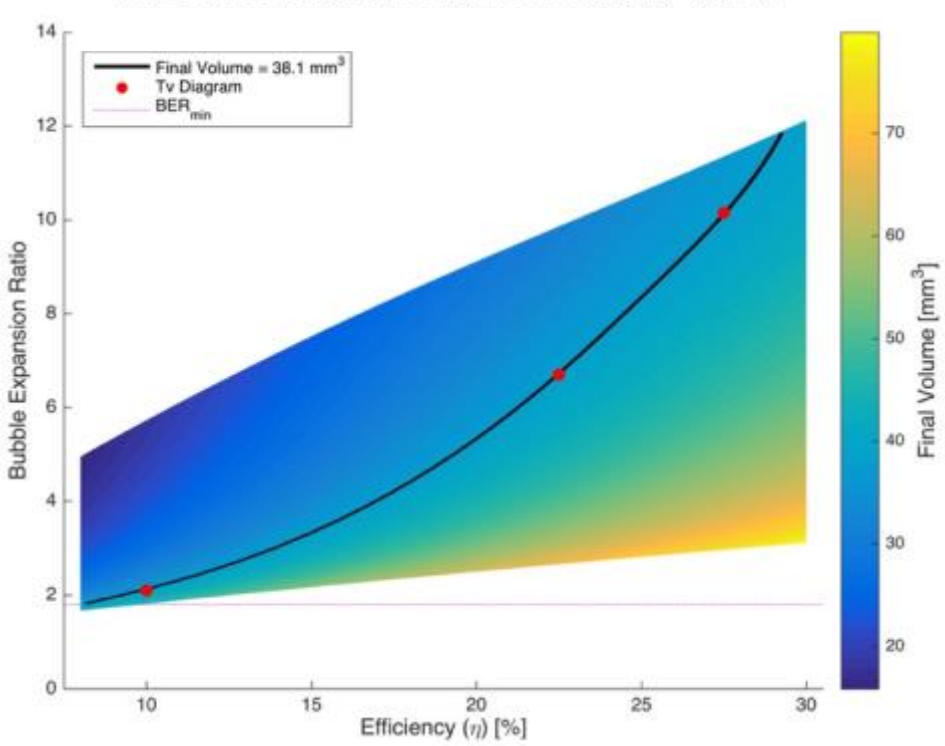

Figure 51. Surface of thermodynamically allowable solutions, with line of constant volume for C=1,081pF.

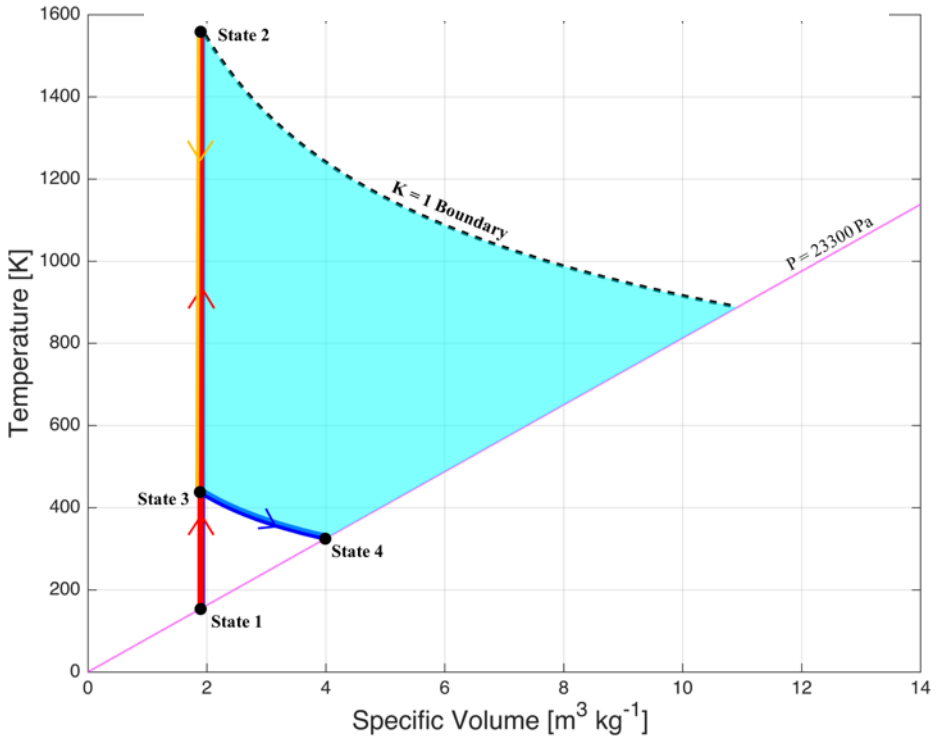

Figure 52. Tv process diagram for C=1,081pF at η_{12}=10%, *k*= 5.64.

On the opposite end of the possible efficiency range the solution for η_{12}=27.5% has a BER of 10.2 corresponding to a *k*=1.18, figure 53. A maximum temperature of 3,168K was reached for this efficiency and it expanded to a final density of 0.052[kg m^{-3}] and temperature of 1,563K. This solution is at the upper end of possible efficiencies and characterized by a low degree of mixing. Even though the BER for this solution is less than half the maximum BER (26.9) it represents the realistic maximum efficiency because the maximum efficiency in this case is not limited by the maximum BER. Instead the maximum efficiency is limited by *k*=1 (simple model with no mixing) which occurs for the solution at η_{12}=29.2%, where the BER is equal to 11.9.

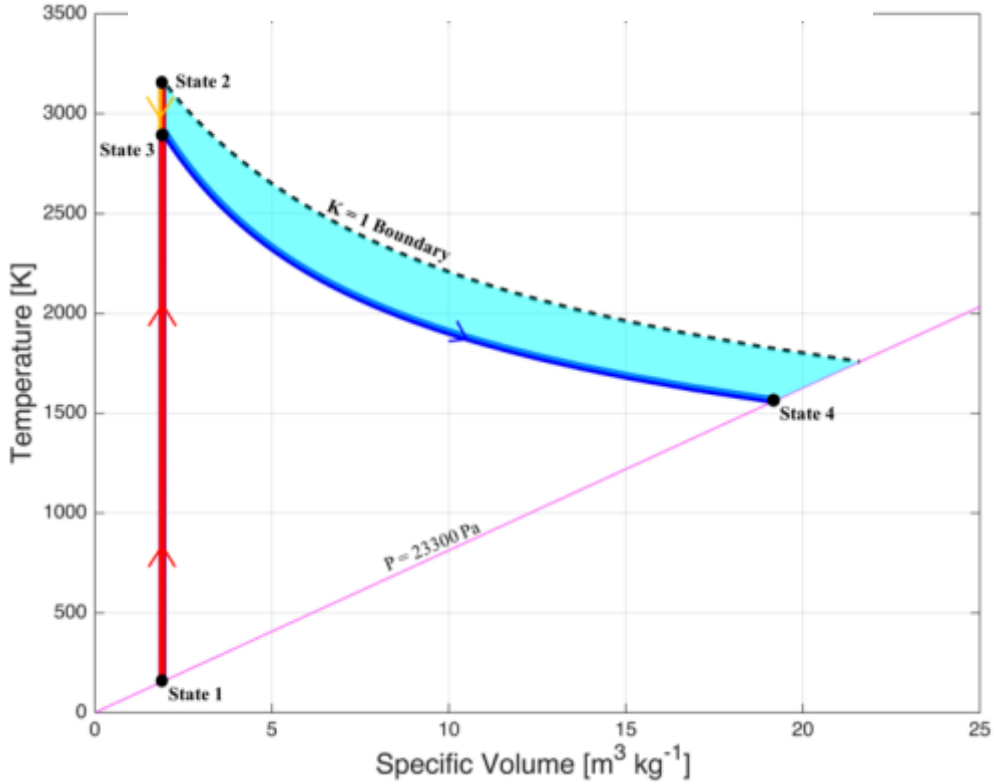

Figure 53. Tv process diagram for C=1,081pF at η_{12}=27.5%, *k*=1.18.

Again, the actual solution would most likely lie in-between these two extremes. However, the solution would not be right in the middle of the two, it would most likely exist in the upper half of the possible efficiency range. Because, the minimum BER is not as well defined for this case as it was for the C=179pF case and the minimum BER would only increase, with more experimental data, shrinking the range of possible efficiencies from the lower end. The solution at η_{12}=22.5% represents a realistic solution in the upper half of the possible efficiency range. The solution for η_{12}=22.5% has a BER of 6.7 corresponding to a *k*=1.76, figure 54. A maximum temperature of 2,876K was reached for

this efficiency and it expanded to a final density of 0.079 [kg m^{-3}] and temperature of 1,046K. The state variables are given in table 5.

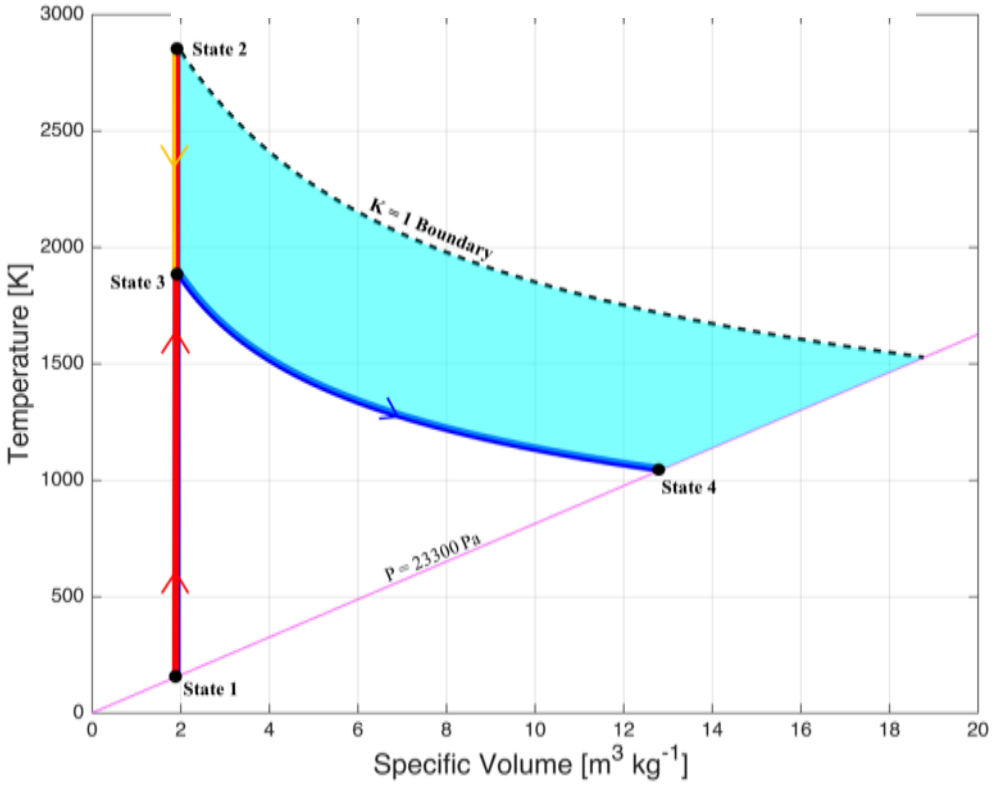

Figure 54. Tv process diagram for C=1,081pF at η_{12}=22.5%, *k*=1.76.

Table 5. State variables for C=1081pF at η_{12}=22.5%, *k*=1.76.

State	T [K]	P [kPa]	u [J kg^{-1} K^{-1}]	s [J $kg^{-1}K^{-1}$]	*v* [m^3 kg^{-1}]	R [kJ kg^{-1} K^{-1}]
1	155	23.3	1255	6458	1.91	287.0
2	2885	438.5	$2.41x10^6$	8885	1.91	289.8
3	1907	287.0	$1.29x10^6$	8440	1.91	287.0
4	1046	23.3	$5.00x10^5$	8440	12.87	287.0

5.2.3 Model Results for C=10,000pF

The surface of thermodynamically possible solutions and line of constant volume for C=10,560pF is shown in figure 55. The possible efficiencies limited by the max and min BER range from 2.7% to 12.6%. The solution for η_{12}=12.5% is representative of the upper efficiency limit and has a BER of 60.8 corresponding to a *k*=1.03, figure 56. This solution reaches a maximum temperature of 8,525K expanding to a final density of 0.009 [kg m^{-3}] and temperature of 6,983K. The line of constant pressure at P=23,330Pa is included in every Tv diagram as given by the ideal gas law. A line of constant pressure is linear with respect to T for a given v at lower temperatures where the specific gas constant is invariant. At temperatures around 2,500K the specific gas constant begins to increase as O_2 dissociation begins causing the line of constant pressure to deviate.

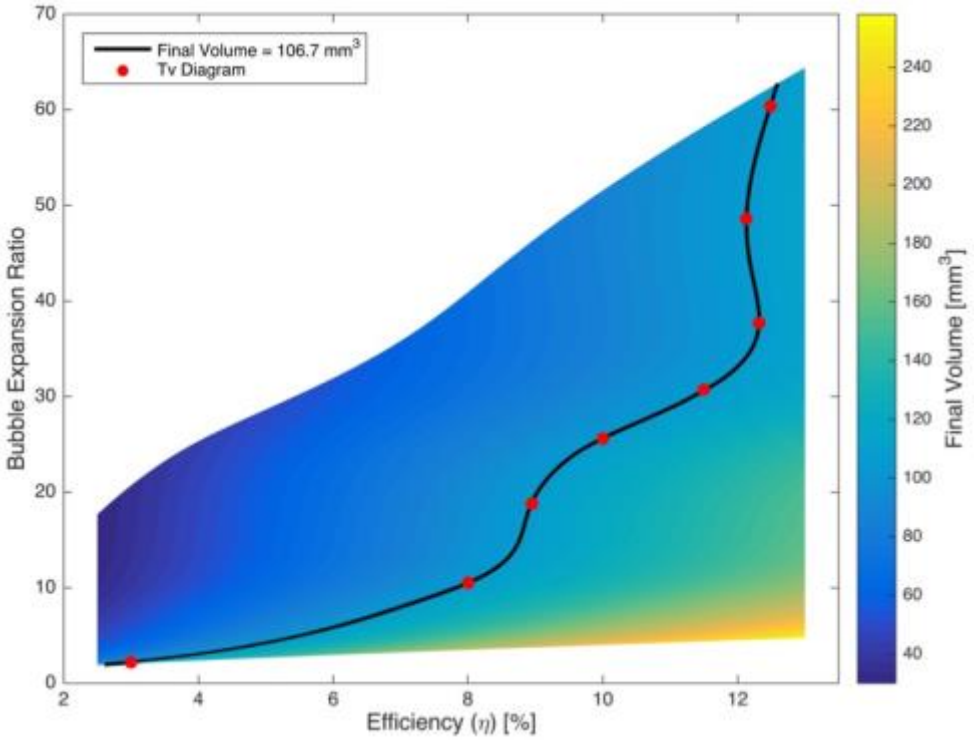

Figure 55. Surface of thermodynamically allowable solutions, with line of constant volume for C=10,560pF.

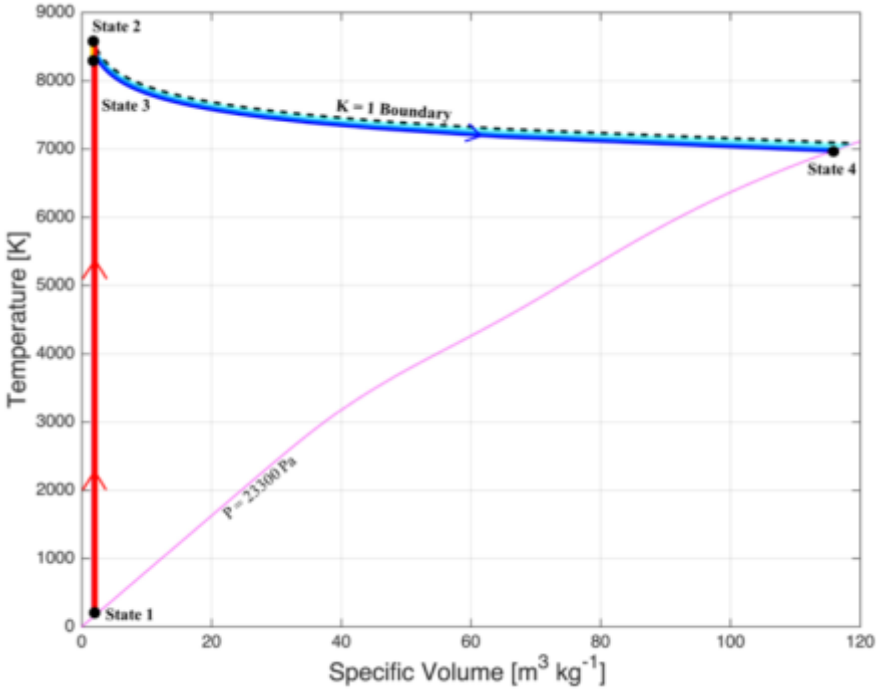

Figure 56. Tv process diagram for C=10,560pF at η_{12}=12.5%, *k*=1.03.

The solution for η_{12}=3% is representative of the lower efficiency limit and has a BER of 2.2 corresponding to a *k*=28.7, figure 57. This solution reaches a maximum temperature of 4,237K and expands to a final density of 0.238 [kg m^{-3}] and temperature of 340K. This solution is near the lower end of possible efficiencies and characterized by a high degree of mixing. The minimum BER for this capacitor is less known than for C=1,081pF, therefore, the lower efficiency limit would likely increase with more experimental data. Due to the uncertainty associated with the minimum BER there was no upper limit placed on the mixing factor when computing the surface of possible solutions in the process model. The amount of ambient air mixed with the high temperature high pressure region was increased until the line of constant final expanded volume crossed the minimum BER, setting the lower limit on possible efficiency. This lead to excessively large mixing factors at the lower end of the possible efficiency range. Excessively large mixing factors are not realistic, as illustrated by figure 57, because:

- The actual mixing is not instantaneous as modeled from state 2 to state 3. The mixing is slow compared to the time scale of energy deposition. Therefore, mixing large amount of ambient air is not possible before the high temperature high pressure region begins to expand.
- The temperature of the final expanded region associated with large mixing factors is unrealistically low.

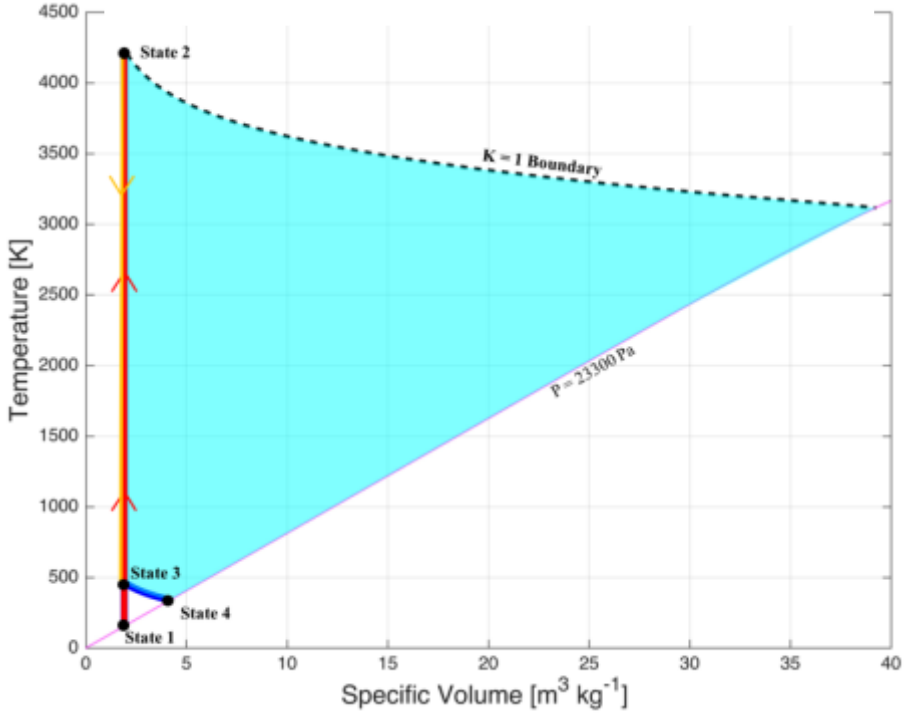

Figure 57. Tv process diagram for C=10,560pF at η_{12}=3%, *k*=28.7.

Therefore, the actual solution would most likely lie in the upper portion of possible efficiencies, between η_{12}=6.0-12.0%. However, two inflection point on the line of constant final volume exists at ~η_{12}=9% and η_{12}=12.1% due to the activation of various energy modes at the higher temperatures achieved for the C=10,560pF case. Therefore, four representative solution around this region are presented in table 6, figures 58-61. The state variables for η_{12}=11.5 are given in table 7.

Table 6. Properties for solutions corresponding to η_{12}=8 - 11.5% for C=10,560pF.

η_{12} [%]	BER	*k*	T_{max} [K]	T_{final} [K]	ρ_{final} [kg m^{-3}]
8.0	10.6	5.90	7343	1640	0.050
9.0	17.9	3.55	7629	2757	0.029
10.0	25.3	2.45	7894	3698	0.021
11.5	30.6	2.00	8099	4150	0.017

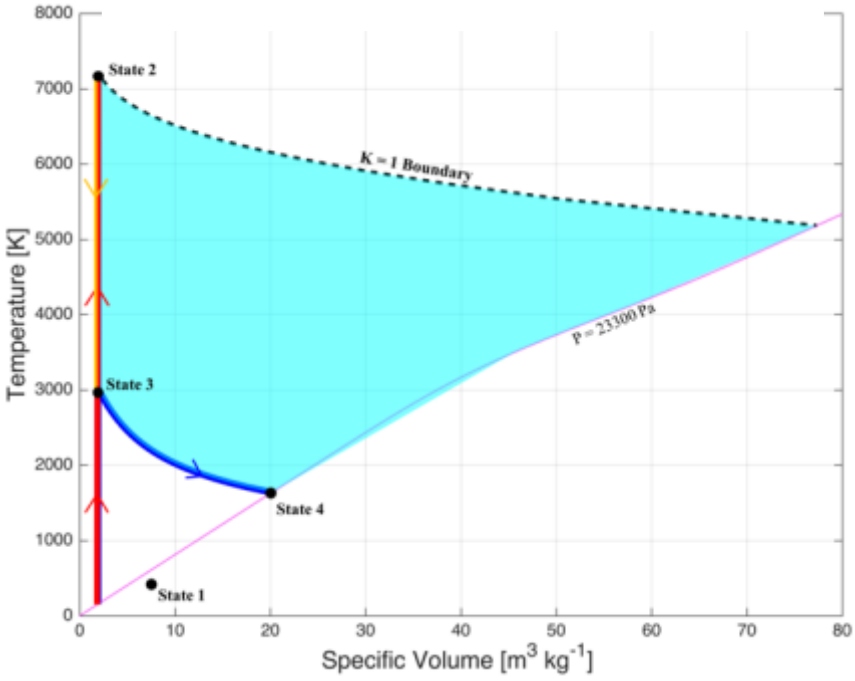

Figure 58. Tv process diagram for C=10,560pF at η=8%, *k*=5.9.

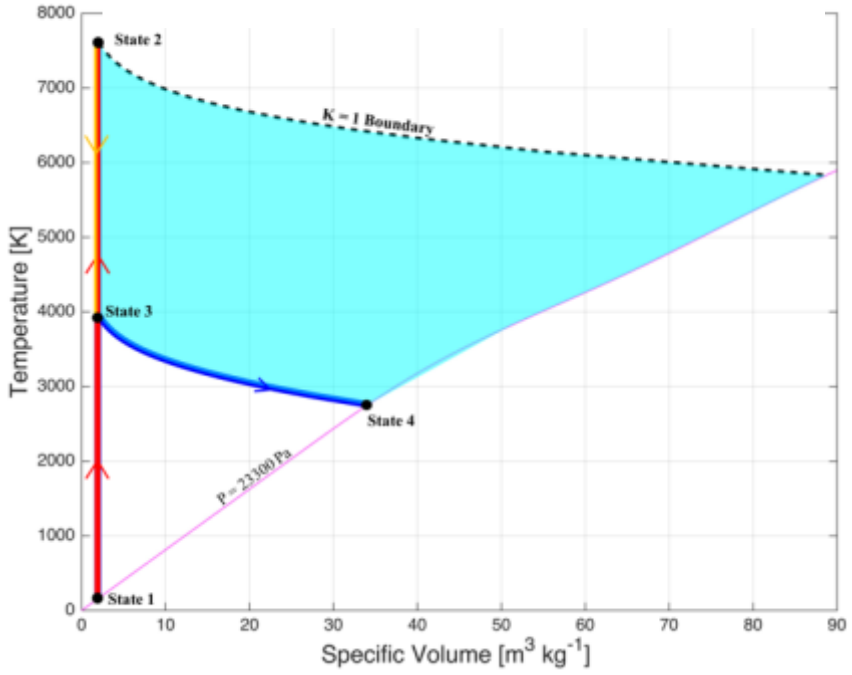

Figure 59. Tv process diagram for C=10,560pF at η=9%, *k*=3.55.

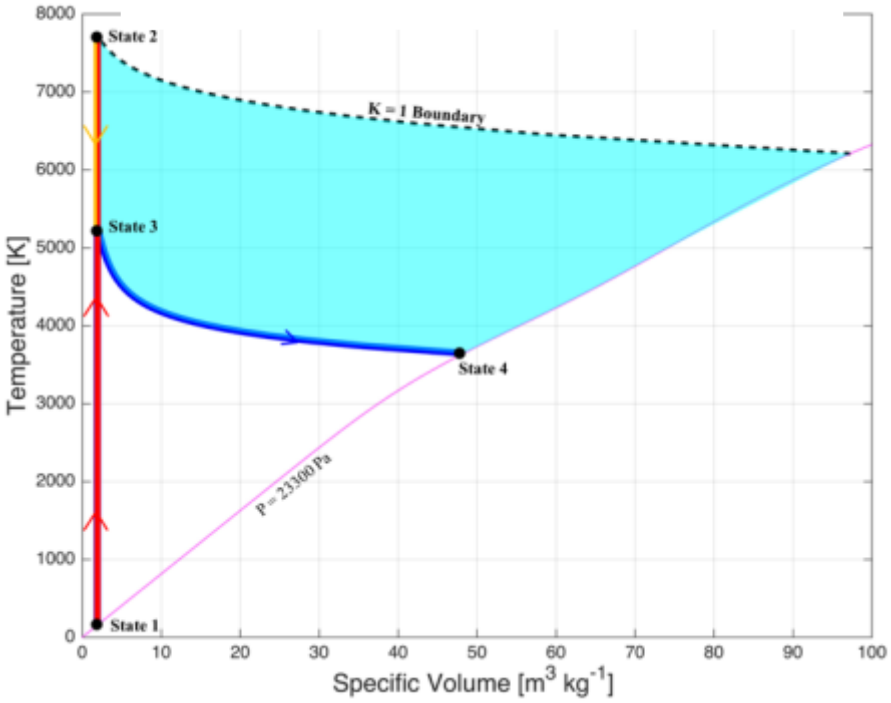

Figure 60. Tv process diagram for C=10,560pF at η=10%, *k*=2.45.

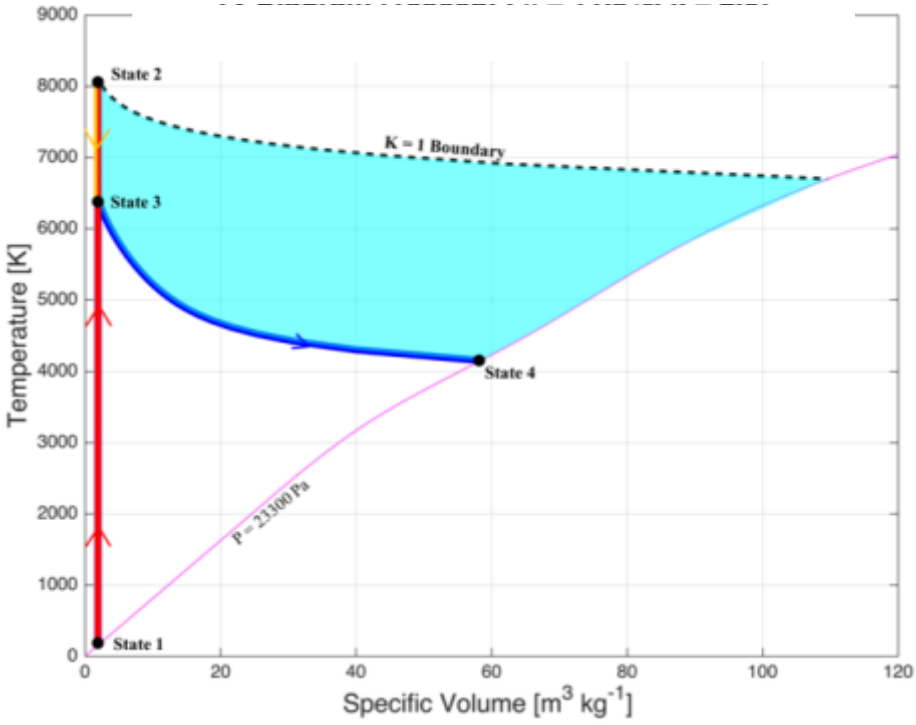

Figure 61. Tv process diagram for C=10,560pF at η=11.5%, *k*=2.0.

Table 7. State variables for C=10,560pF at η_{12}=11.5%, *k*=2.0.

State	T [K]	P [kPa]	u [J kg^{-1} K^{-1}]	s [J kg^{-1}K^{-1}]	*v* [m^3 kg^{-1}]	R [kJ kg^{-1} K^{-1}]
1	155	23.3	1255	6458	1.91	287.0
2	8274	1999	2.41×10^6	12279	1.91	460.7
3	6512	1266	1.29×10^6	10790	1.91	370.6
4	4222	23.3	5.00×10^5	10790	59.24	327.4

5.2.4 Results Overview

Using the justification for increasing the lower efficiency limit given in section 5.2.2 and 5.2.3 the range of possible efficiencies was reduced for C=1,081pF and C=10,560pF. The range of possible efficiencies for C=179pF was not altered, as the max and minimum BER were well defined. The maximum mixing factor for C=1,081pF was reduced from 8 to 4, which increased the lower efficiency limit from 8.1% to 13.9%, figure 62. The maximum mixing factor for C=10,560pF was reduced from 32 to 15, which increased the lower efficiency limit from 2.7% to 5.0%, figure 63.

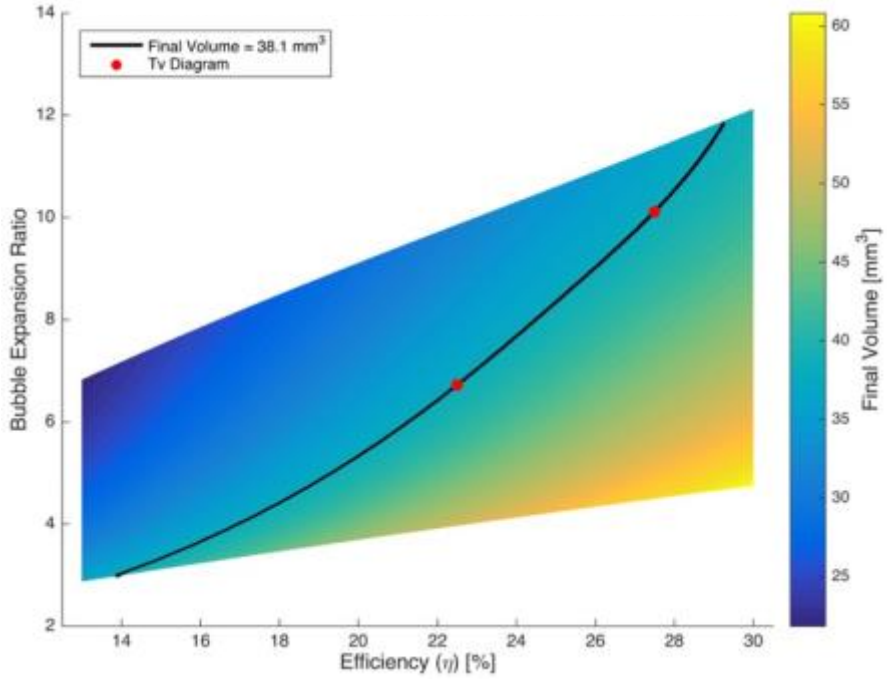

Figure 62. Surface plot with reduced range of possible efficiencies for C=1,081pF.

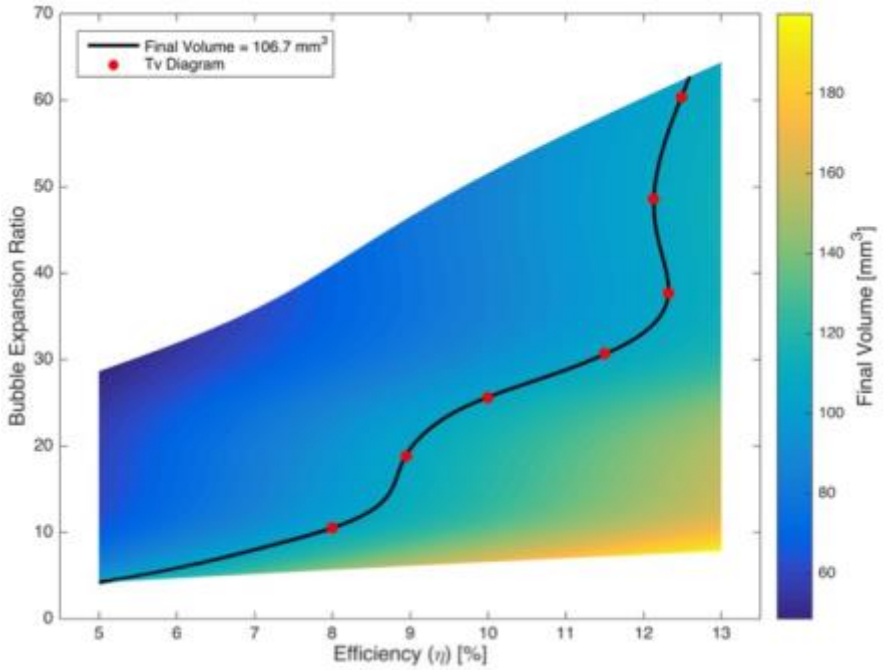

Figure 63. Surface plot with range of possible efficiencies for C=10,560pF.

6. CONCLUSIONS

6.1 Summary of Work Done

The work accomplished throughout this thesis was a combination of both theoretical/computational and experimental research. The experimental portion of the thesis included:

- Design and fabrication of the spark actuator, which included material selection, machining and assembly of the components and installation into the wind tunnel test section.
- Design and assembly of a high voltage pulsing RC circuit that powered the spark actuator.
- Installation of diagnostic probes and transformers to measure the instantaneous voltage across and current through the spark actuator.
- Operation of the Supersonic High Reynolds number wind tunnel and supporting infrastructure.
- Installation of a schlieren imaging system around the SHR tunnel to image the energy deposition process. Schlieren images of the expanding region were taken at 5μs intervals until the effected region was no longer visible. The volume of the expanding region was calculated from the images to determine the final expanded volume and bubble expansion ratio.
- Set up an ICCD camera capable of nanosecond response and shutter time to image the individual plasma filaments. From these images the volume of the discharge

region was calculated for use as the initial condition for the thermodynamic process model.

The theoretical/computational portion of this thesis consisted of the creation of a high temperature thermodynamic model of air used to estimate the efficiency of the spark actuator. The thermodynamic model consisted of two portions:

1. The Thermodynamic Properties Model – This portion of the model uses the NASA PAC database to calculate the thermodynamic properties (enthalpy, entropy, and specific heat) of N_2, O_2, N, O, Ar, then the equilibrium composition of an air mixture valid for temperature between 200-20,000K.
2. The Thermodynamic Process Model – This portion models the energy deposition as a constant volume heating process, creating a high temperature high pressure region of air. This region is then mixed with varying amounts of ambient air to simulate heat diffusion to the surrounding. The mixed region is then isentropically expanded to ambient pressure, where the final expanded volume is calculated for comparison to the experimental images.

The experimental and computational results were compared to bound the efficiency of electrical energy conversion to thermal energy in the flow.

6.2 Summary of Findings

The final expanded volume and, maximum and minimum BER were calculated from the series of schlieren images captured for each capacitor. The initial discharge volume was calculated from the images of the plasma filament. The average energy per

pulse for each capacitor was calculated from the mean breakdown voltage, 6,200±400V, and measured total circuit capacitance. The experimental data is summarized in table 8.

Table 8. Summary of experimental data.

Nominal Capacitance [pF]	Total Capacitance [pF]	Energy [mJ]	Final Volume [mm^3]	BER_{min}	BER_{max}
100	179	3.4	26	3.8	6.9
1000	1081	20.8	38	1.8	26.9
10000	10560	203	107	2.0	108.0

The experimentally determined final volume and bubble expansion ratio were used to limit the range of possible efficiencies calculated by the thermodynamic model, the efficiency ranges determined for each capacitor are given in table 9.

Table 9. Range of possible efficiencies.

Nominal Capacitance [pF]	Total Capacitance [pF]	Energy [mJ]	η Range [%]	K Range	BER Range
100	179	3.4	67.0 - 92.0	1.0 - 1.8	3.8-6.5
1000	1081	20.8	13.9 - 29.2	1.0 - 4.0	3.0-10.2
10000	10560	203	5.0 - 11.8	1.9 - 15	4.2-30.6

It is clear the low energy case (C=179pF) is the most efficient at converting the electrical energy into thermal energy in the flow. The efficiency is not the only important metric in classifying the effectiveness of the spark actuator. The gas temperature and density of the expanded region are other important metrics in determining the overall effectiveness of the spark actuator. These effectiveness parameters for each capacitor for the efficiency ranges listed above are summarized in table 10, figure 64, figure 65. The density ratio is defined as the inverse of the BER and indicates the final density as a percentage of the

initial density. The final temperature and final density follow the same trend because the ideal gas law was assumed and the final pressure was constant (P_s=23,300Pa) for all the cases.

Table 10. Effectiveness parameters.

Capacitor [pF]	Energy [mJ]	Final Temperature [K]	Density Ratio
179	3.4	590 - 1009	0.263 - 0.154
1081	20.8	465 - 1563	0.333 - 0.098
10560	203	649 - 4150	0.238 - 0.033

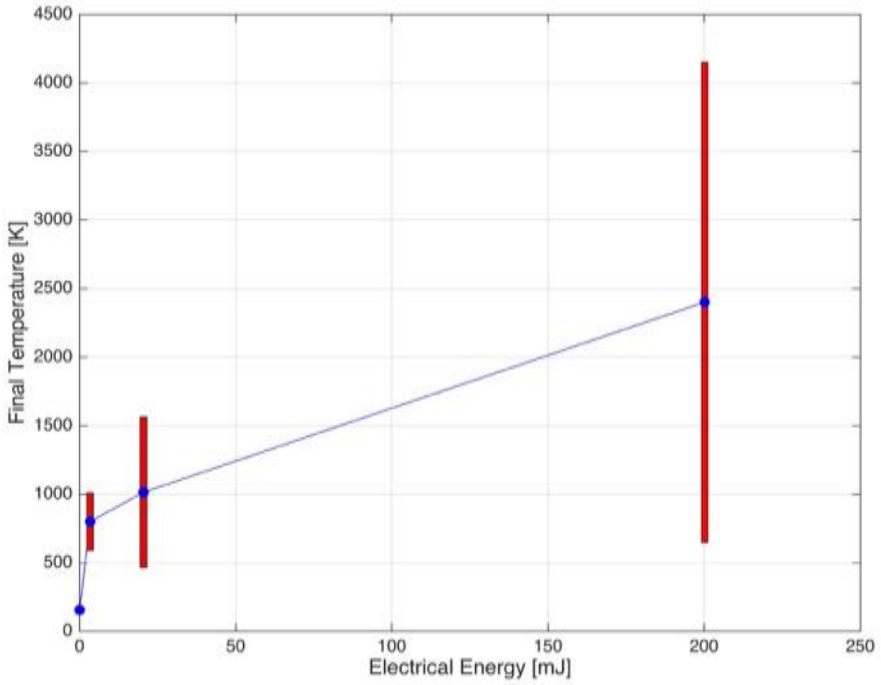

Figure 64. Range of final expanded temperatures for the three input energies.

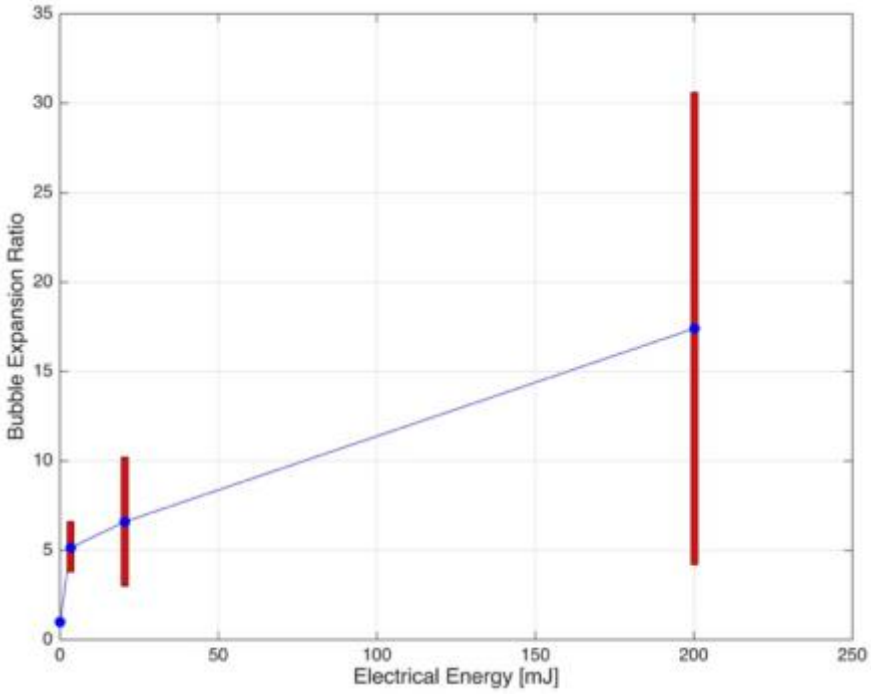

Figure 65. Range of expansion ratios for the three input energies.

6.3 Concluding Remarks

The objective of this research was to measure the conversion efficiency of electrical energy into thermal energy in a supersonic flow field during the energy deposition process. The objective of this research was accomplished but only a possible efficiency range was determined for each input energy, and a few important conclusions were drawn from the data.

The possible efficiencies for C=100pf were much higher than the other two larger energy cases (C=1,000 and 10,000pF). This is due to the activation of the vibrational and electronic energy modes of the molecules or atoms. As the maximum temperature approaches 2,500-3,000K vibrational excitation and dissociation of O_2 begin to absorb energy that would have otherwise be converted to thermal energy. This is the sharp rise

beginning at T≈2,500K in the specific heat curves, figure 24, of the high temperature air mixture. The dissociation can be thought of as a pseudo phase change in that much more energy is required to raise the gas temperature while the O_2 dissociates, similar to the boiling process of any liquid. The second peak in figure 24 corresponds the dissociation of N_2 but is only encountered at the upper portion of the efficiency range for C=10,000pF.

However, throughout the course of this research it was determined that the efficiency is only one of the important parameters in characterizing the total effectiveness of the energy deposition process. The primary mechanism of the drag reduction seen in the reviewed literature is due to the decrease in density of the effected region. While the C=100pF case is more efficient with regards to energy conversion, the C=10,000pF case is more effective with regards to the application of drag reduction.

6.4 Future Work

The results of this research helped to explain some of the underlying mechanisms governing energy deposition in high speed flows. However, additional experimental data would help to narrow down the range of possible efficiencies, including:

- Masking the bandpass filter to block plasma light from blinding the camera at early delays for the two higher energy cases.
- Obtain additional schlieren images at time delays between 1-5μs after discharge.
- Uses different capacitors to vary the input energy, including capacitors within the current range (for example 500, 2,000, 5,000pF) and capacitors larger than 10,000pF.

- Match the inductance to each capacitor to maximize electrical power transfer, because the inductance of the circuit was not changed during the experiment but the capacitance was.
- Run set of experiments where all three capacitors have the same energy density by vary gap distance (breakdown voltage).

The thermodynamic model could be improved by better modeling heat transfer, which would help to limit the maximum mixing ratio, thereby reducing the range of possible efficiencies by increasing the lower limit. Time resolved optical emission spectroscopy could be used to measure the rotational and vibrational temperature of the plasma during the energy deposition process.

The future of energy deposition has the potential to revolutionize the aerospace community because such a wide range of techniques and applications exist. However, more fundamental research into the underlying physics of the energy deposition process are required before these technologies can become reality.

REFERENCES

1. Knight, D., "Survey of Aerodynamic Drag Reduction at High Speed by Energy Deposition", *Journal of Propulsion and Power*, Vol. 24, No. 6, November-December 2008, pp. 1153–1167.
2. Fomin, V., Tretyakov, P., and Taran, J. "Flow Control Using Various Plasma and Aerodynamic Approaches (Short Review)", *Aerospace Science and Technology*, Vol. 8, 2004, pp. 411–421.
3. Riggins, D., Nelson, H., and Johnson, E. "Blunt-Body Wave Drag Reduction Using Focused Energy Deposition", *AIAA Journal*, Vol. 37, No. 4 (1999), pp. 460-467.
4. Kremeyer, K. "Lines of Pulsed Energy for Supersonic/Hypersonic Drag Reduction: Generation and Implementation", *AIAA Paper No.* 2004-984, 2004.
5. Kremeyer, K., Sebastian, K., and Shu, W. "Computational Study of Shock Mitigation and Drag Reduction by Pulsed Energy Lines", *AIAA Journal*, Vol. 44, No. 8, August 2006.
6. Kremeyer, Kevin. Shock Wave Modification Method, Apparatus, and System. Robert P. Swiatek, assignee. Patent US 6,527,221 B1. 4 Mar. 2003. Print.
7. Kolesnichenko, Y., et al. "Basics in Beamed MW Energy Deposition for Flow/Flight Control", *42nd AIAA Aerospace Sciences Meeting and Exhibit*, Reno, Nevada, January 5-8, 2004.

8. Minucci, M., et al. “Laser-Supported Directed-Energy ‘Air Spike’ In Hypersonic Flow”, *Journal of Spacecraft and Rockets*, Vol. 42, No. 1, January – February 2005, pp. 51-57.

9. Kremeyer, K. “Energy Deposition II: Physical Mechanisms Underlying Techniques to Achieve High-Speed Flow Control”, *AIAA Paper No.* 2015-3502, 2015.

10. Kremeyer, K. “Lines of Energy Deposition for Supersonic/Hypersonic Temperature/Drag-Reduction and Vehicle Control”, *AIP Conference Proceedings* Volume 997, Issue 1, pp. 353-366, 2008.

11. Kremeyer, K., Mickelson, P., and Montaño, E. “Energy Deposition to Efficiently Reduce Sonic Boom and Drag, and Increase Control Authority in High-Speed Applications”, *AIAA Paper No.* 2017-2340, 2017.

12. Chen, Francis. *Plasma Physics and Controlled Fusion* Vol 1. New York, Plenum Press, 1984. Print.

13. Anderson, John D., Jr. *Hypersonics and High-Temperature Gas Dynamics* Second Edition. Reston VA, American Institute of Aeronautics and Astronautics Inc., 2006. Print.

14. Raizer, Yu. *Gas Discharge Physics* Second Edition. Berlin, Springer-Verlag, 1991. Print.

15. Roth, Reece. *Industrial Plasma Engineering* Vol. 1. London, IOP Publishing Ltd., 1995. Print.

16. Miles, R. “Plasma Flow Control: Fundamentals, Modeling and Applications”, February 21-24, 2011. Rhode Saint Genèse, Belgium: *Von Karman Institute for Fluid Dynamics*, 2011. Print. Lecture series.

17. Brichkin, D., Kuranov, A., and Sheikin, E. “Use of MHD Systems in Hypersonic Flight Vehicles”, *Perspectives of MHD and Plasma Technologies in Aerospace Applications*, 24 March 1999 - 25 March 1999, Russian Academy of Sciences, 1999.

18. Kremeyer, K., Nazarenko, S., and Newell, A. “The Role of Vorticity in Shock Propagation Through Inhomogeneous Media”, *37th AIAA Aerospace Sciences Meeting and Exhibit*, Reno, Nevada, January 11-14, 1999.

19. Kremeyer, K., Nazarenko, S., and Newell, A. “The Effect of Fore-shock Heating in the Plasma Drag-reduction Problem”, *AIAA Paper No.* 2000-2700, 2000.

20. Kremeyer, K., Nazarenko, S., and Newell, A. “Shock Bowing and Vorticity Dynamics During Propagation into Different Transverse Density Profiles”, *Physica D*, Vol. 163, Issue 3-4, March 2002, pp. 150-165.

21. Leonov, S., Bityurin, V., Savischenko, N., Yuriev, A., and Gromov, V. “Influence of Surface Electrical Discharge on Friction of Plate in Subsonic and Transonic Airflow”, *AIAA Paper No.* 2001-0640, 2001.

22. Leonov, S., Bityurin, V., Savelkin, K., and Yarantsev, D., “Effect of Electrical Discharge on Separation Processes and Shocks Position in Supersonic Airflow”, *AIAA Paper No.* 2002-0355, 2002.

23. Yanji, H., Diankai, W., and Jifei, Y. “Interaction of single-pulse laser energy with bow shock in hypersonic flow”, *Chinese Journal of Aeronautics*, Vol 27, pp. 241-247. 2015.

24. Toro, P., Myrabo, L., and Nagamatsu, H. “Pressure Investigation of the Hypersonic "Directed-Energy Air Spike" Inlet at Mach Number 10 up to 70 kW”, *AIAA Paper No.* 1998-0991, 1998.

25. Tretyakov, P., Garanin, A., Kraynev, V., Tupikin, A. and Yakovlev, V. “Investigation of Local Laser Energy Release Influence on Supersonic Flow by Methods of Aerophysical Experiments”, *Proceedings of the 8th International Conference on Methods in Aerophysical Research*, Institute of Theoretical and Applied Mechanics, Russian Academy of Sciences, Novosibirsk, Russia, 1996, pp 200–204.

26. Adelgren, R., Elliott, G., Knight, D., Zheltovodov, A., and Beutner, T. “Energy Deposition in Supersonic Flows”, *AIAA Paper No.* 2001-0885.

27. Adelgren, R., Elliott, G., Knight, D., Zheltovodov, A., and Buetner, T., “Localized Flow Control in Supersonic Flows by Pulsed Laser Energy Deposition”, *The Third Workshop on Magneto and Plasma Aerodynamics for Aerospace Applications*, Institute for High Temperatures, Moscow, Russia, April 2001.

28. Adelgren, R., Elliott, G., Knight, D., Buetner, T., Ivanov, M., and Zheltovodov, A. “Laser Energy Deposition in Transverse Wall Jets and Intersecting Shocks”,

Workshop on Thermochemical Processes in Plasma Aerodynamics, Hypersonic System Research Institute, St. Petersburg, Russia, September 2001.

29. Kolesnichenko, Y., Brovkin, V., Leonov, S., Krylov, A., Lashkov, V., Mashek, I., Gorynya, A., and Ryvkin, M. "Investigation of AD-Body Interaction with Microwave Discharge in Supersonic Flows," *AIAA Paper No.* 2001-0345, 2001.

30. Kolesnichenko, Y., Brovkin, V., Leonov, S., Krylov, A., Lashkov, V., Mashek, I., Gorynya, A., and Ryvkin, M. "Influence of Differently Organized Microwave Discharge on AD-Body Characteristics in Supersonic Flow," *AIAA Paper No.* 2001-3060, 2001.

31. Kolesnichenko, Y., Brovkin, V., Khmara, D., Lashkov, V., Mashek, I., and Ryvkin, M. "Microwave Discharge Parameters in Supersonic Flow," *AIAA Paper No.* 2002-0356, 2002.

32. Kolesnichenko, Y., Brovkin, V., Azarova, O., Grudnitsky, V., Lashkov, V., and Mashek, I. "MW Energy Deposition for Aerodynamic Application," *AIAA Paper No.* 2003-0361, 2003.

33. Kolesnichenko, Y., Brovkin, V., Khmara, D., Lashkov, V., Mashek, I., and Ryvkin, M. "Fine Structure of MW Discharge: Evolution Scenario," *AIAA Paper No.* 2003-0362, 2003.

34. Kolesnichenko, Y., Azarova, O., Brovkin, D., Khmara, D., Lashkov, V., Mashek, I., and Ryvkin, M. "Basics in Beamed MW Energy Deposition for Flow/Flight Control," *AIAA Paper No.* 2004-0669, 2004.

35. Exton, R., Balla, R., Shirinzadeh, B., Brauckmann, G., Hering, G., Kelliher, W., Fugitt, J., Lazard, C., and Khodataev, K. “On-Board Projection of a Microwave Plasma Upstream of a Mach 6 Bow Shock”, *Physics of Plasmas*, Vol. 8, No. 11, Nov. 2001, pp. 5013–5017.

36. Knight, D. “Survey of Aerodynamic Flow Control at High Speed by Energy Deposition” *AIAA Paper No.* 2003-0525, 2003.

37. Settles, G. S. *Schlieren and Shadowgraph Techniques*. New York: Springer-Verlag, 2001. Print.

38. Ekoto, Isaac W. “Supersonic Turbulent Boundary Layers with Periodic Mechanical Non-Equilibrium” Ph.D. Dissertation, Texas A&M University, 2006.

39. Tichenor, Nathan R. “Characterization of the Influence of a Favorable Pressure Gradient on the Basic Structure of a Mach 5.0 High Reynolds Number Supersonic Turbulent Boundary Layer” Ph.D. Dissertation, Texas A&M University, 2010.

40. John, James E. and Keith, Theo G. *Gas Dynamics* Third Edition. New Jersey: Pearson Education Inc., 2006. Print.

41. Jaffe, R., Schwenke, D., and Chaban, D. “Vibrational and Rotational Excitation and Dissociation in N2-N2 Collisions from Accurate Theoretical Calculations” *AIAA Paper No.* 2010-4517, 2010.

42. McBride, B., Zehe, M., and Gordon, S. “NASA Glenn Coefficients for Calculating Thermodynamic Properties of Individual Species” *NASA Technical Publication:* 2002-211556. Glenn Research Center, Cleveland, Ohio.

43. Gurvich, L., Veyts, I., and Alcock C. *Thermodynamic Properties of Individual Substances, Part One Methods and Computation* Fourth Edition, Vol. 1. New York, Hemisphere Publishing Corporation, 1989.

44. Turns, S. *An Introduction to Combustion Concepts and Applications* Second Edition. Singapore, McGraw Hill Book Co., 2000.

APPENDIX

A.1 MATLAB code

A.1.1. Thermodynamic Properties Code

```
Ru  = 8314.4598;  %[J kmol^-1 K^-1]
P = 23331;  %[Pa]
v = (Ru/28.9651785)*220/P;

% Molecular weights
MN2plus = 28.0128514;  %[kg/k-mol]
MN2 = 28.0134000;
MO2 = 31.9988000;
MN = 14.0061514;
MO = 15.9994000;
MAr = 39.9480000;
M = [MN2, MO2, MN, MO, MAr];

TL = linspace(150, 1000, 20);
TM = linspace(1001, 6000, 199);
TH = linspace(6025, 20000, 400);
Trange = [TM, TH];
T = [TM, TH];

%% NASA Coefficients
aN2plus6 = [-2.845599002E+06, 7.058893030E+03, -2.884886385E+00, 3.068677059E-03, -4.361652310E-07, 2.102514545E-11, 5.411996470E-16, 1.340388483D+05, 5.090897022D+01];
aN2plus20 = [-3.712829770D+08, 3.139287234D+05, -9.603518050D+01, 1.571193286D-02, -1.175065525D-06, 4.144441230D-11, -5.621893090D-16, -2.217361867D+06, 8.436270947D+02];
aNplus20 = [1.646092148D+07, -1.113165218D+04, 4.976986640D+00, -2.005393583D-04, 1.022481356D-08, -2.691430863D-13, 3.539931593D-18, 3.136284696D+05, -1.706646380D+01];

% N2
aN2_1 = [2.210371497D+04, -3.818461820D+02, 6.082738360D+00, -8.530914410D-03, 1.384646189D-05, -9.625793620D-09, 2.519705809D-12, 7.108460860D+02, -1.076003744D+01];
aN2_6 = [5.877124060E+05, -2.239249073E+03, 6.066949220E+00, -6.139685500E-04, 1.491806679E-07, -1.923105485E-11, 1.061954386E-15, 1.283210415D+04, -1.586640027D+01];
aN2_20 = [8.310139160E+08, -6.420733540E+05, 2.020264635E+02, -3.065092046E-02, 2.486903333E-06, -9.705954110E-11, 1.437538881E-15, 4.938707040D+06, -1.672099740D+03];

% O2
aO2_1 = [-3.425563420D+04, 4.847000970D+02, 1.119010961D+00, 4.293889240D-03, -6.836300520D-07, -2.023372700D-09, 1.039040018D-12, -3.391454870D+03, 1.849699470D+01];
aO2_6 = [-1.037939022E+06, 2.344830282E+03, 1.819732036E+00, 1.267847582E-03, -2.188067988E-07, 2.053719572E-11, -8.193467050E-16, -1.689010929D+04, 1.738716506D+01];
aO2_20 = [4.975294300E+08, -2.866106874E+05, 6.690352250E+01, -6.169959020E-03, 3.016396027E-07, -7.421416600E-12, 7.278175770E-17, 2.293554027D+06, -5.530621610D+02];

% N
aN_1 = [0.000000000D+00, 0.000000000D+00, 2.500000000D+00, 0.000000000D+00, 0.000000000D+00, 0.000000000D+00, 0.000000000D+00, 5.610463780D+04, 4.193905036D+00];
aN_6 = [8.876501380E+04, -1.071231500E+02, 2.362188287E+00, 2.916720081E-04, -1.729515100E-07, 4.012657880E-11, -2.677227571E-15, 5.697351330D+04, 4.865231506D+00];
aN_20 = [5.475181050E+08, -3.107574980E+05, 6.916782740E+01, -6.847988130E-03, 3.827572400E-07, -1.098367709E-11, 1.277986024E-16, 2.550585618D+06, -5.848769753D+02];

% O
aO_1 = [-7.953611300D+03, 1.607177787D+02, 1.966226438D+00, 1.013670310D-03, -1.110415423D-06, 6.517507500D-10, -1.584779251D-13, 2.840362437D+04, 8.404241820D+00];
aO_6 = [2.619020262E+05, -7.298722030E+02, 3.317177270E+00, -4.281334360E-04, 1.036104594E-07, -9.438304330E-12, 2.725038297E-16, 3.392428060D+04, -6.679585350D-01];
aO_20 = [1.779004264E+08, -1.082328257E+05, 2.810778365E+01, -2.975232262E-03, 1.854997534E-07, -5.796231540E-12, 7.191720164E-17, 8.890942630D+05, -2.181728151D+02];

% Ar
```

```
aAr_1 = [0.000000000D+00,  0.000000000D+00,  2.500000000D+00,  0.000000000D+00,  0.000000000D+00,  0.000000000D+00,
0.000000000D+00,  -7.453750000D+02,  4.379674910D+00];
aAr_6 = [2.010538475D+01,  -5.992661070D-02,  2.500069401D+00,  -3.992141160D-08,  1.205272140D-11,  -1.819015576D-15,
1.078576636D-19,  -7.449939610D+02,  4.379180110D+00];
aAr_20 = [-9.951265080D+08,  6.458887260D+05,  -1.675894697D+02,  2.319933363D-02,  -1.721080911D-06,  6.531938460D-
11,  -9.740147729D-16,  -5.078300340D+06,  1.465298484D+03];

SpecName = {'N2','O2','N','O','Ar'};
LowTCoef = [aN2_1; aO2_1; aN_1; aO_1; aAr_1];
midTCoef = [aN2_6; aO2_6; aN_6; aO_6; aAr_6];
HighTCoef = [aN2_20; aO2_20; aN_20; aO_20; aAr_20];

%Enthalpy calculated from 2002 NASA thermo properties
for ii = 1:length(SpecName)
    hM = hfunct(midTCoef(ii,:), TM);
    hH = hfunct(HighTCoef(ii,:), TH);
    h(ii,:) = [hM, hH];  %[J/kmol]
end

% Entropy calculated from 2002 NASA thermo properties
for ii = 1:length(SpecName)
    sM = sfunct(midTCoef(ii,:), TM, P);
    sH = sfunct(HighTCoef(ii,:), TH, P);
    so(ii,:) = [sM, sH];  %[J/kmol K]
end

% specific heat at constant pressure calculated from 2002 NASA thermo properties
for ii = 1:length(SpecName)
    cpM = cpfunct(midTCoef(ii,:), TM);
    cpH = cpfunct(HighTCoef(ii,:), TH);
    cp(ii,:) = [cpM, cpH];
end

% Gibbs Energy
for ii = 1:length(T)
   for iii = 1:length(SpecName)
    g(iii,ii) = h(iii,ii)-T(ii)*so(iii,ii);
    end
end

%% Equilibrium calacuation
sz = size(T);
Aa = zeros(sz);
Aa(1) = 0.78;
Bb = zeros(sz);
Bb(1) = 0.21;
Cc = zeros(sz);
Dd = zeros(sz);

for ii = 1:length(T)
   [MoleFracts1(:,ii), Aa(ii+1), Bb(ii+1), Cc(ii+1), Dd(ii+1)] = equifunctFormula(T(ii), v, g, Aa(ii), Bb(ii), Cc(ii), Dd(ii), Trange);
end

%% Properties from 200-1000K
for ii = 1:length(SpecName)
    hL(ii,:) = hfunct(LowTCoef(ii,:), TL);
end
h = [hL, h];
for ii = 1:length(SpecName)
    sL(ii,:) = sfunct(LowTCoef(ii,:), TL, P);
end
so = [sL, so];
for ii = 1:length(TL)
   initialMoles(:,ii) = MoleFracts1(:, 1);
end
MoleFracts1 = [initialMoles, MoleFracts1];
for ii = 1:length(SpecName)
    cpL(ii,:) = cpfunct(LowTCoef(ii,:), TL);
end
cp = [cpL, cp];
```

```
T = [TL, T];

%% Mixture Properties
% Mixture Molecular Weight
for ii = 1:length(T)
    M_weighted(ii) = sum(M.*MoleFracts1(:,ii));
end

% Enthalpy
h_contribution = h.*MoleFracts1;
h_weighted = sum(h_contribution,1);

% Calculating cp from Enthalpy (dh/dT)P = Cp
cp_weighted = derivative(T,h_weighted);

% Entropy
so_contribution = so.*MoleFracts1;
so_weighted = sum(so_contribution,1);

% Cp
cp_contribution = cp.*MoleFracts1;
cp_weighted1 = sum(cp_contribution,1);

%% Functions

hfunct
sfunct
cpfunct
equifunct For mula

function [ h1 ] = hfunct(a1,T)
Ru = 8314.4598; %[J kmol^-1 K^-1]
h1 = Ru.*T.*(-a1(1).*T.^-2+a1(2).*log(T)./T+a1(3)+a1(4)/2.*T+a1(5)./3.*T.^2+a1(6)./4.*T.^3+a1(7)./5.*T.^4+a1(8)./T);
end

function [ so ] = sfunct(a1,T)
Ru = 8314.4598; %[J kmol^-1 K^-1]
so = Ru.*(-a1(1)./2.*T.^-2-a1(2).*T.^-1+a1(3).*log(T)+a1(4).*T+a1(5)./2.*T.^2+a1(6)./3.*T.^3+a1(7)./4.*T.^4+a1(9));
end

function [ cp1 ] = cpfunct(a1,T1)
Ru = 8314.4598; %[J kmol^-1 K^-1]
cp1 = Ru.*(a1(1).*T1.^-2+a1(2).*T1.^-1+a1(3)+a1(4).*T1+a1(5).*T1.^2+a1(6).*T1.^3+a1(7).*T1.^4);
end

function [MF, A, B, C, D] = equifunct For mula(T,v,g,E,F,G,H,Tv)
% SpecName = {'N2','O2','N','O','Ar'};

Ru = 8314.4598; %[J kmol^-1 K^-1]
Po = 100e3; %reference Pressure [Pa]
kmoleN2i = 0.78;
kmoleO2i = 0.21;
kmoleAri = 0.01;
e = kmoleAri;

MN2 = 28.0134000;
MO2 = 31.9988000;
MN = 14.0061514;
MO = 15.9994000;
MAr = 39.9480000;
M = [MN2, MO2, MN, MO, MAr];

XN2fi = E/(E+F+G+H+e);
XO2fi = F/(E+F+G+H+e);
XNfi = G/(E+F+G+H+e);
XOfi = H/(E+F+G+H+e);
XArfi = e/(E+F+G+H+e);

Mmix = (XN2fi*M(1)+XO2fi*M(2)+XNfi*M(3)+XOfi*M(4)+XArfi*M(5));
Rmix = Ru/Mmix;
```

```
P = Rmix*T/v;  % EOS

gN2 = g(1,:);
gO2 = g(2,:);
gN = g(3,:);
gO = g(4,:);

ind = find(Tv==T);
gN2T = gN2(ind);
gO2T = gO2(ind);
gNT = gN(ind);
gOT = gO(ind);

syms a b c d
XN2 = a/(a+b+c+d+e);
XO2 = b/(a+b+c+d+e);
XN = c/(a+b+c+d+e);
XO = d/(a+b+c+d+e);

[Y1, Y2, Y3, Y4] = vpasolve([2*kmoleN2i ==2*a+c, 2*kmoleO2i ==2*b+d, (XN2*P/Po)^-1*(XN*P/Po)^2 == exp(-((-
1)*gN2T+2*gNT)/(Ru*T)), (XO2*P/Po)^-1*(XO*P/Po)^2 == exp(-((-1)*gO2T+2*gOT)/(Ru*T))],[a, b, c, d]);

% (XN2*P/Po)^-1*(XN*P/Po)^2 == exp(-((-1)*gN2+2*gN)/(Ru*T))
% (XO2*P/Po)^-1*(XO*P/Po)^2 == exp(-((-1)*gO2+2*gO)/(Ru*T))

A = double(Y1);
A = A(A>=0 & A<=E);
A = mean(A);
B = double(Y2);
B = B(B>=0 & B<=F);
B = mean(B);
C = double(Y3);
C = C(C>=G & C<=(2*kmoleN2i));
C = mean(C);
D = double(Y4);
D = D(D>=H & D<=(2*kmoleO2i));
D = mean(D);
XN2f = A/(A+B+C+D+e);
XO2f = B/(A+B+C+D+e);
XNf = C/(A+B+C+D+e);
XOf = D/(A+B+C+D+e);
XArf = e/(A+B+C+D+e);
MF = [XN2f, XO2f, XNf, XOf, XArf];
end
```

A.1.2. Thermodynamic Properties Code

```
load('HotAir_150K.mat')

close all
clc
clearvars -except T MoleFracts1 h_weighted so_weighted M_weighted cp_weighted cp_weighted1 so h

SavePlot = 0;
plotThermoProp = 0;
Cap = 1000;

%% Units
% Length - meters [m]
% time - seconds [s]
% Temperature - Kelvin [K]
% Mass - kilogram [kg]
% Pressure - Pascal [Pa]
```

```
% Energy - Joule [J]
% Molar - kilomoles [kmole]

%% Overall Properties
Ru = 8314.4598;  %[J kmol^-1 K^-1]
Po = 100e3;  %[Pa]
P = 23331;  %[Pa]

% Mixture Specific Gas Constant
Rmix = Ru./M_weighted;  %[J kg^-1 K^-1]

% Ehtnalpy, Entropy and Specific Heat on a per kg basis
h_weighted_kg = h_weighted./M_weighted;  %[J kg^-1]
so_weighted_kg = so_weighted./M_weighted;  %[J kg^-1 K^-1]
cp_weighted_kg = cp_weighted./M_weighted;  %[J kg^-1 K^-1]
cp_weighted_NASA_kg = cp_weighted1./M_weighted;  %[J kg^-1 K^-1]

% Internal Energy
u_weighted = h_weighted - Ru.*T;  %[J kg^-1]
u_weighted_kg = h_weighted_kg - Rmix.*T;  %[J kg^-1]

% Specific Heat constant volume
cv_weighted = cp_weighted-Ru;
cv_weighted_kg = cv_weighted./M_weighted;
cv_weighted_NASA = cp_weighted1-Ru;
cv_weighted_NASA_kg = cv_weighted_NASA./M_weighted;

%% If statement for different Caps
if Cap == 100
    capTitle = '100pF';
    C = 179e-12;
   finalExpandedArea = 3.4e-6;  %[m^2]
    FilamentVolume = 3.95e-9;  %[m^3]
    maxTotalExpansionRatio = 6.9;  %Area final / A discharge
    minBubbleExpansionRatio = 3.75;  %Area final / Area earlier (5.6us)

    k = linspace(1,1.8,299);  %100pF
    eta = linspace(0.67,0.92,300);  %100pF

    xloc = [70,80,90];  %100pF
    yloc = [4.01,5.05,6.33];
    zloc = [26.05,26,26];
end
if Cap == 1000
    capTitle = '1000pF';
    C = 1078e-12;
   finalExpandedArea = 5e-6;  %[m^2]
    FilamentVolume = 3.2e-9;  %[m^3]
    maxTotalExpansionRatio = 26.9;  %Area final / A discharge
    minBubbleExpansionRatio = 1.8;  %Area final / Area earlier (15us)

%     k = linspace(1,8,299);
%     eta = linspace(0.08,0.30,300);  %

    k = linspace(1,4,299);  %reduced k range
    eta = linspace(0.13,0.30,300);  %reduced k range

    xloc = [10,22.5,27.5];  %1000pF final Vol = 38.1mm3
    yloc = [2.1,6.72,10.11];
    zloc = [50,38.6,38.6];
end
if Cap == 10000
    capTitle = '10000pF';
    C = 10550e-12;
   finalExpandedArea = 14e-6;  %[m^2]
    FilamentVolume = 1.7e-9;  %[m^3]

    maxTotalExpansionRatio = 108;  %Area final / A discharge
    minBubbleExpansionRatio = 2.0;  %Area final / Area earlier (15us)
%
```

```
%     k = linspace(1.8,32,299); %2 to 32
%     eta = linspace(0.025, 0.118, 300); %10000pF

    k = linspace(1.9,15,299);   %reduced k range
    eta = linspace(0.05, 0.118, 300); %reduced k range

    xloc = [3, 8, 8.95, 10, 11.5]; %10000pF final Vol = 106.7mm3
    yloc = [2.2 10.5, 18.8, 25.6, 30.7];
    zloc = [110, 110, 110, 110, 108];
end

% L1 will expand too but assuming constant
L1 = 0.3; %[in]
L1 = L1*0.0254; %convert to [m]
finalExpandedVolume = finalExpandedArea*L1; %[m^3]

%% Energy Input
Ec = 0.5*C*6000^2;
Ein = Ec*eta;

%% State Properties
% State 1: Ambient Tunnel Conditions
    V_1 = FilamentVolume; %[m^3]
    P_1 = 23331; %[Pa]
    T_1 = 155; %[K]
    R_1 = interp1(T,Rmix,T_1); %[J kg^-1 K^-1]
    v_1 = R_1*T_1/P_1; %[m^3 kg^-1]
    m_1 = FilamentVolume/v_1; %[kg]
   rho_1 = 1/v_1; %[kg m^-3]

    h_1 = interp1(T,h_weighted_kg,T_1); %[J kg^-1]
    so_1 = interp1(T,so_weighted_kg,T_1); %[J kg^-1 K^-1]
    s_1 = so_1-R_1*log(P_1/Po); %[J kg^-1 K^-1]
    u_1 = interp1(T,u_weighted_kg,T_1); %[J kg^-1]

    % State 2: Hot Bubble
    v_2 = v_1; %[m^3 kg^-1]
    m_2 = m_1; %[kg]
for ii=1:length(eta);

    u_2(ii) = u_1+Ein(ii)/m_1; % Energy balance (constant volume heating from state 1) [J kg^-1]
    T_2(ii) = interp1(u_weighted_kg,T,u_2(ii));
    R_2(ii) = interp1(T,Rmix,T_2(ii)); %[J kg^-1 K^-1]
    P_2(ii) = R_2(ii).*T_2(ii)./v_2; %[Pa]
   rho_2 = 1/v_2; %[kg m^-3]

    h_2(ii) = interp1(T,h_weighted_kg,T_2(ii)); %[J kg^-1]
    so_2(ii) = interp1(T,so_weighted_kg,T_2(ii)); %[J kg^-1 K^-1]
    s_2(ii) = so_2(ii)-R_2(ii).*log(P_2(ii)/Po); %[J kg^-1 K^-1]

    u_m = u_1;
    h_m = h_1;
    s_m = s_1;
    v_m = v_1;
    T_m = T_1;
    P_m = P_1;
   for iii=1:length(k)
       % Mass to be mixed (ambient conditions)
       m_m(iii) = (k(iii)-1) * m_2;

       % State 3: Mixed hot state
       m_3(iii) = k(iii)*m_2; %[kg]
       u_3(iii,ii) = (m_2*u_2(ii) + m_m(iii)*u_m)/m_3(iii); %first law, assume: no W or Q [J kg^-1]

       %assumeing mixing occurs without a specific volume change [m^3 kg^-1]
       v_3(iii,ii) = (m_2*v_2 + m_m(iii)*v_m)/m_3(iii);
       T_3(iii,ii) = interp1(u_weighted_kg,T,u_3(iii,ii)); %[K]
       R_3(iii,ii) = interp1(T,Rmix,T_3(iii,ii)); %[J kg^-1 K^-1]
       P_3(iii,ii) = R_3(iii,ii)*T_3(iii,ii)/v_3(iii,ii); %[Pa]
      rho_3(iii,ii) = 1/v_3(iii,ii); %[kg m^-3]
```

```
        h_3(iii,ii) = interp1(T, h_weighted_kg, T_3(iii,ii));  %[J kg^-1]
        so_3(iii,ii) = interp1(T, so_weighted_kg, T_3(iii,ii));  %[J kg^-1 K^-1]
        s_3(iii,ii) = so_3(iii,ii)- R_3(iii,ii)*log(P_3(iii,ii)/Po);  %[J kg^-1 K^-1]

        %State 4: Isentropic expansion to ambeient pressure
        P_4 = P_1;
        s_4 = s_3;  %Isentropic assumption
        m_4 = m_3;

        so_4(iii,ii) = so_3(iii,ii)+R_3(iii,ii)*log(P_4/P_3(iii,ii));  %[J kg^-1 K^-1]
        T_4(iii,ii) = interp1(so_weighted_kg, T, so_4(iii,ii));  %[K]
        R_4(iii,ii) = interp1(T, Rmix, T_4(iii,ii));
        %Iteration on T_4 because R_4 is dependent on T_4 but needed to calculate T_4
        rem = 10;
        while rem > 1
            T_temp = T_4(iii,ii);
            so_4(iii,ii) = so_3(iii,ii)+R_4(iii,ii)*log(P_4/P_3(iii,ii));  %[J kg^-1 K^-1]
            T_4(iii,ii) = interp1(so_weighted_kg, T, so_4(iii,ii));  %[K]
            R_4(iii,ii) = interp1(T, Rmix, T_4(iii,ii));  %[J kg^-1 K^-1]
            rem = abs(T_4(iii,ii)- T_temp);
        end
        v_4(iii,ii) = R_4(iii,ii)*T_4(iii,ii)/P_4;  %[m^3 kg^-1]
        rho_4(iii,ii) = 1/v_4(iii,ii);  %[kg m^-3]
        BubbleExpansionRatio(iii,ii) = v_4(iii,ii)/v_3(iii,ii);
        final_density_ratio(iii,ii) = rho_4(iii,ii)/rho_1;
        DensityPrecentage(iii,ii) = rho_1/rho_4(iii,ii);
    end
end

k_m = k'*ones(1,length(eta));
TotalExpansionRatio = k_m*BubbleExpansionRatio;

m_4m = m_4'*ones(1,length(eta));  %[kg]
Vol_4 = v_4.*m_4m;  %[m^3]
volumeRatio = Vol_4/Filament Volume;

%% Plots

if plotThermoProp
    if SavePlot
        oldcdir=cd;  % Don't change
        datadir='/Users/ngawloski/Documents/Grad School _Thesis/Thermo Model/Matlab Results';
        cd(datadir)  % Changes the current directory
    end

    SpecName = {'N2','CO2','N','O','Ar'};
    % Mole Fraction Plot
    figure
    plot(T, MoleFracts1(1,:), T, MoleFracts1(2,:), T, MoleFracts1(3,:), T, MoleFracts1(4,:), T, MoleFracts1(5,:),'LineWidth',2)
    grid on
    xtik=get(gca,'xtick');
    s=sprintf('%d',xtik(1));
    for i=2:length(xtik)
        s=strvcat(s,sprintf('%d',xtik(i)));
    end
    set(gca,'xticklabel',s)
    title('Mole Fraction of High Temperature Air (N_2, O_2, N, O, Ar)','FontSize',16)
    xlabel('Temperature [K]','FontSize',14)
    ylabel('Mole Fraction','FontSize',14)
    Leg = {SpecName{:}};
    legend(Leg)
    set(gcf,'Position', get(0,'Screensize'));  % Maximize figure.
    if SavePlot
        print(gcf,'-r600','-djpeg95',['MoleFractions_150K.jpg'])
    end

    %Enthalpy Plot
    figure
    plot(T,h_weighted_kg,'LineWidth',2)
```

```
grid on
xtik=get(gca,'xtick');
s=sprintf('%d',xtik(1));
for i=2:length(xtik)
    s=strvcat(s,sprintf('%d',xtik(i)));
end
set(gca,'xticklabel',s)
title('Enthalpy of High Temperature Air (N_2, O_2, N, O, Ar)','FontSize',16)
xlabel('Temperature [K]','FontSize',14)
ylabel('Enthalpy [J/kg]','FontSize',14)
set(gcf,'Position',get(0,'Screensize'));  % Maximize figure.
if SavePlot
    print(gcf,'-r600','-djpeg95',['Enthalpy_150K.jpg'])
end

figure
plot(T,h/1000,T,h_weighted/1000,'x-','LineWidth',2)
grid on
ylim([0 11e5])
xtik=get(gca,'xtick');
s=sprintf('%d',xtik(1));
for i=2:length(xtik)
    s=strvcat(s,sprintf('%d',xtik(i)));
end
set(gca,'xticklabel',s)
title('Molar Enthalpy of High Temperature Air','FontSize',16)
xlabel('Temperature [K]','FontSize',14)
ylabel('Enthalpy [kJ/kmole]','FontSize',14)
Leg = {SpecName{:},'High Temp Air Mixture'};
legend(Leg,'Location','northwest')
set(gcf,'Position',get(0,'Screensize'));  % Maximize figure.
if SavePlot
    print(gcf,'-r600','-djpeg95',['Molar Enthalpy_150K.jpg'])
end


%Entropy Plot
figure
plot(T,so_weighted_kg,'LineWidth',2)
grid on
xtik=get(gca,'xtick');
s=sprintf('%d',xtik(1));
for i=2:length(xtik)
    s=strvcat(s,sprintf('%d',xtik(i)));
end
set(gca,'xticklabel',s)
title('Entropy of High Temperature Air (N_2, O_2, N, O, Ar)','FontSize',16)
xlabel('Temperature [K]','FontSize',14)
ylabel('Entropy [J/kg K]','FontSize',14)
set(gcf,'Position',get(0,'Screensize'));  % Maximize figure.
if SavePlot
    print(gcf,'-r600','-djpeg95',['Entropy_150K.jpg'])
end

figure
plot(T,so/1000,T,so_weighted/1000,'x-','LineWidth',2)
grid on
xtik=get(gca,'xtick');
s=sprintf('%d',xtik(1));
for i=2:length(xtik)
    s=strvcat(s,sprintf('%d',xtik(i)));
end
set(gca,'xticklabel',s)
title('Molar Entropy (at Po = 100kPa)','FontSize',16)
xlabel('Temperature [K]','FontSize',14)
ylabel('Entropy [kJ/kmole K]','FontSize',14)
Leg = {SpecName{:},'High Temp Air Mixture'};
legend(Leg,'Location','northwest')
set(gcf,'Position',get(0,'Screensize'));  % Maximize figure.
if SavePlot
```

```
        print(gcf,'-r600','-djpeg95',['Molar Entropy_150K.jpg'])
    end


    %Specific Heat
    figure
    plot(T,cp_weighted_kg/1000,T,cv_weighted_kg/1000,T,cp_weighted_NASA_kg/1000,T,cv_weighted_NASA_kg/1000,'LineWid
th',2)
    grid on
    xtik=get(gca,'xtick');
    s=sprintf('%d',xtik(1));
    for i=2:length(xtik)
        s=strvcat(s,sprintf('%d',xtik(i)));
    end
    set(gca,'xticklabel',s)
    title('Specific Heats of High Temperature Air','FontSize',16)
    xlabel('Temperature [K]','FontSize',14)
    ylabel('Specific Heat [kJ/kg K]','FontSize',14)
    Leg = {'Cp (Diff of Enthalpy)','Cv (Diff of Enthalpy)','Cp (No Dissociation)','Cv (No Dissociation)'};
    legend(Leg)
    set(gcf,'Position',get(0,'Screensize'));  %Maximize figure.
    if SavePlot
        print(gcf,'-r600','-djpeg95',['SpecificHeats_150K.jpg'])
    end

    %Gamma
    gamma = cp_weighted_kg./cv_weighted_kg;
    figure
    plot(T,gamma,'LineWidth',2)
    grid on
    xtik=get(gca,'xtick');
    s=sprintf('%d',xtik(1));
    for i=2:length(xtik)
        s=strvcat(s,sprintf('%d',xtik(i)));
    end
    set(gca,'xticklabel',s)
    title('Ratio of Spacific Heats (Gamma)','FontSize',16)
    xlabel('Temperature [K]','FontSize',14)
    ylabel('Gamma','FontSize',14)
    set(gcf,'Position',get(0,'Screensize'));  %Maximize figure.
    if SavePlot
        print(gcf,'-r600','-djpeg95',['Gamma_150K.jpg'])
    end

    %Specific Gas Constant
    figure
    plot(T,Rmix,'LineWidth',2)
    grid on
    xtik=get(gca,'xtick');
    s=sprintf('%d',xtik(1));
    for i=2:length(xtik)
        s=strvcat(s,sprintf('%d',xtik(i)));
    end
    set(gca,'xticklabel',s)
    title('Specific Gas Constant of High Temp Air Mixture','FontSize',16)
    xlabel('Temperature [K]','FontSize',14)
    ylabel('Gas Constant [J/kg K]','FontSize',14)
    set(gcf,'Position',get(0,'Screensize'));  %Maximize figure.
    if SavePlot
        print(gcf,'-r600','-djpeg95',['GasConstant_150K.jpg'])
    end

    if SavePlot
        cd(olddir) %changes back to old directory where this function is located
    end
end


%% Surface Plotting
% Using Expansion Ratio
```

```
% States
% State 1: Ambient Tunnel Conditions
% State 2: Hot Bubble
% State 3: Mixed hot state
% State 4: Isentropic expansion to ambient pressure

% K-Factor = quantifies the amount of mass to be mixed: m_3 = k(iii)*m_2;

%finalExpandedVolume = Known value for each cap = Final Area measured from schlieren pics multiplied by electrode gap
% BubbleExpansionRatio = final specific volume divided by mixed hot state specific volume = v_4 / v_3
% TotalExpansionRatiob = Bubble expansion ratio multiplied by k factor  = k_m*BubbleExpansionRatio;

for ii =1:length(eta)
    BER_matchExp(ii) = interp1(Vol4(:,ii), BubbleExpansionRatio(:,ii),finalExpandedVolume);  %vector
    TER_matchExp(ii) = interp1(Vol4(:,ii), TotalExpansionRatio(:,ii),finalExpandedVolume);  %
    FEV_matchExp(ii) = finalExpandedVolume;  % Vector the size of eta of finalExpandedVolume that will be NaNed
end

%
FEV_matchExp(TER_matchExp>maxTotalExpansionRatio|BER_matchExp<minBubbleExpansionRatio|isnan(BER_matchExp))
= NaN;  %exceed the max expansion ratio

minBERx = [eta(1)*70, eta(end)*110];
minBERy = [minBubbleExpansionRatio, minBubbleExpansionRatio];
minBERz = [finalExpandedVolume*1.1,finalExpandedVolume*1.1];
maxBERx = [eta(1)*70, eta(end)*110];
maxBERy = [maxTotalExpansionRatio, maxTotalExpansionRatio];
maxBERz = [finalExpandedVolume*1.1,finalExpandedVolume*1.1];
s = [45];

% Plot for creating surface
figure
plot3(eta*100, BER_matchExp, FEV_matchExp*1000^3,'k','LineWidth',2);
hold on
scatter3(xloc,yloc,zloc,s,'r','filled')
% hold on
% plot3(minBERx, minBERy, minBERz,'--m')
% plot3(maxBERx, maxBERy, maxBERz,'--g')
volLeg = ['Final Volume = ',num2str(round(finalExpandedVolume*1000^3,1)),' mm^3'];
Leg = {volLeg,'Tv Diagram'};  %'BER_{min}','BER_{max}'};
legend(Leg,'Location','northwest')
view(0,90)
hold on
surf(eta*100,BubbleExpansionRatio,Vol4*1000^3)
xlim([(min(eta)*100-0.5) (max(eta)*100+0.5)])
view(0,90)
shading flat
c = colorbar;
ylabel(c,'Final Volume [mm^3]','FontSize',12)
xlabel('Efficiency (\eta) [%]','FontSize',12)
ylabel('Bubble Expansion Ratio','FontSize',12)
zlabel('Final Volume [mm^3]','FontSize',12)
plotTitle = ['Reduced Surface of Possible Solutions: \eta vs BER (C = 1081pF)'];
title(plotTitle,'FontSize',12)
set(gcf,'Position', get(0,'Screensize'));  % Maximize figure.


if SavePlot
    olddir=cd;  % Don't change
    datadir=['/Users/ngawloski/Documents/Grad School _Thesis/Thermo Model/Matlab Results/',capTitle];
    cd(datadir) % Changes the current directory
    print(gcf,'-r600','-djpeg95',['TotalDischargeEfficiency_surfacePlot_mm3_Reduced.jpg'])
    cd(olddir)
end

%% Combined Energy Plot

BERp = [0.5, 6.7, 25.3];
```

```
Effx = [0, 178, 1081, 10560];
Effx = Effx*1e-12*0.5*6158^2*1000;

figure
plot(Effx, BERp)
r1 = rectangle('position',[Effx(2)*.7, 4.0, 2, 2.4])
set(r1,'facecolor','r')
r2 = rectangle('position',[Effx(3)*.95, 5.3, 2, 3.1])
set(r2,'facecolor','r')
r3 = rectangle('position',[Effx(4)*.995, 10.6, 2, 20])
set(r3,'facecolor','r')
hold on
scatter(Effx, BERp,'b','filled')
grid on
xlabel('Electrical Energy [mJ]','FontSize',12)
ylabel('Bubble Expansion Ratio','FontSize',12)
title('Input Energy vs. Bubble Expansion Ratio','FontSize',12)
set(gcf, 'Position', get(0,'Screensize')); % Maximize figure.

if SavePlot
    olddir=cd; % Don't change
    datadir=['/Users/ngawlowski/Documents/Grad School _ Thesis/Thermo Model/Matlab Results'];
    cd(datadir) % Changes the current directory
    print(gcf,'-r600','-djpeg95',['EnergyVsBER.jpg'])
    cd(olddir)
end
```

A.2. Schlieren images

A.2.1. Images for C=100pF

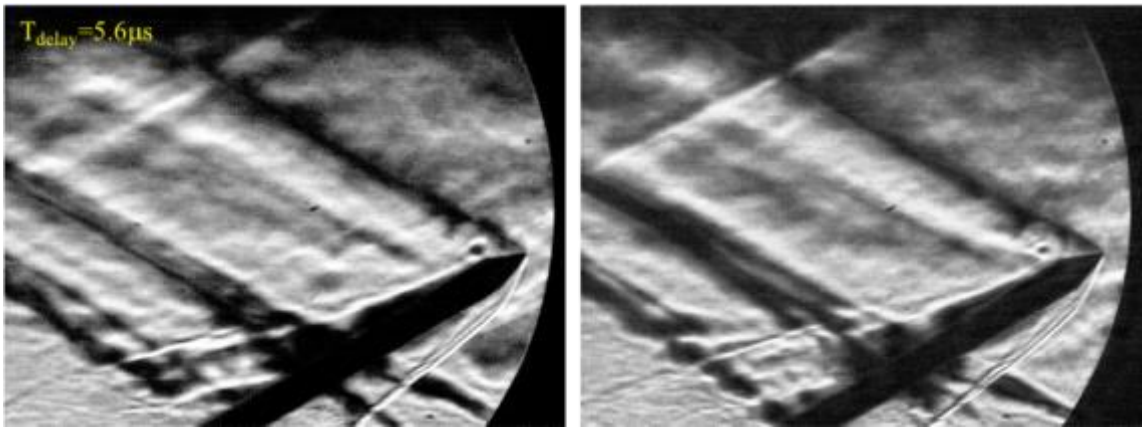

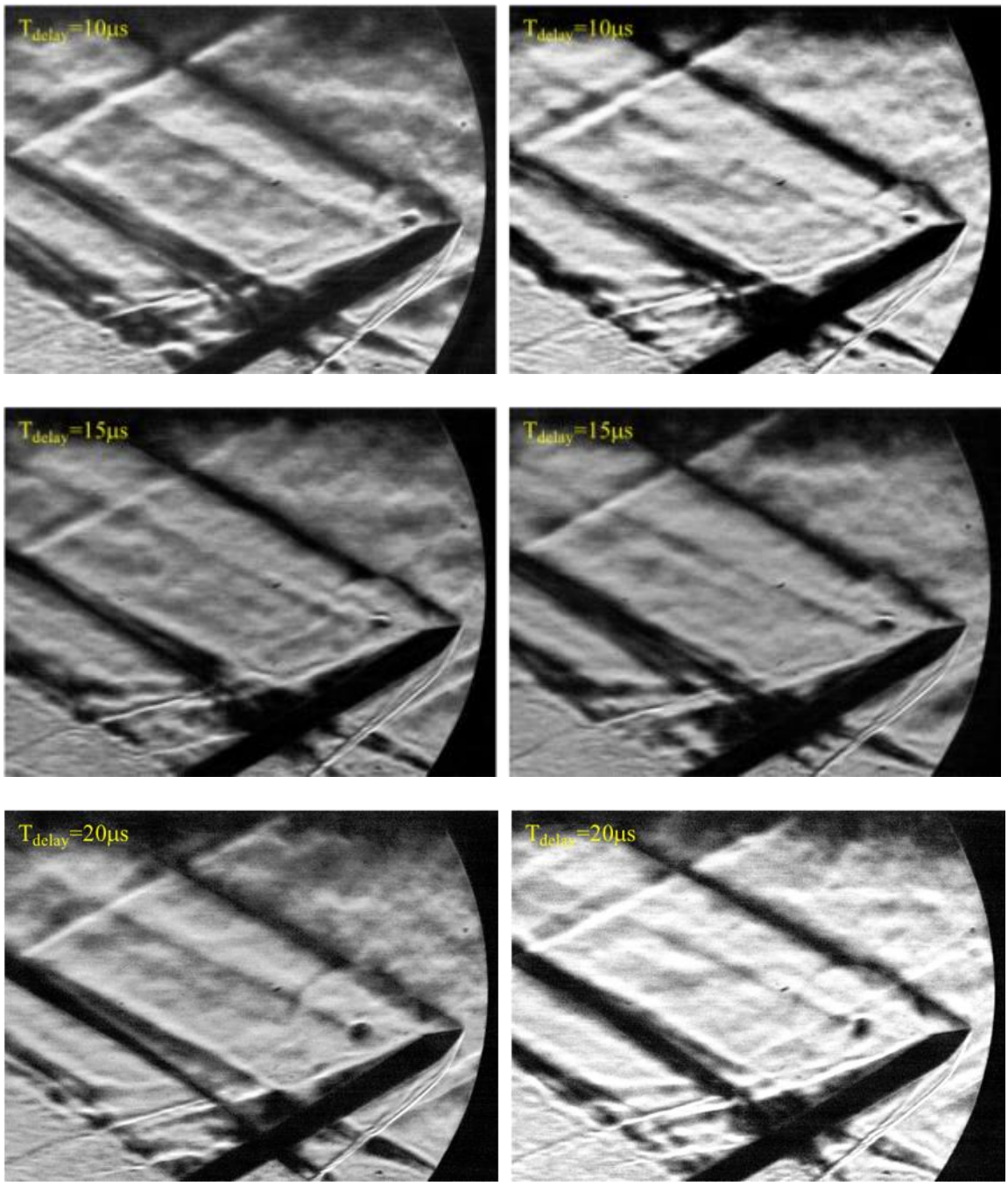
T_{delay}=10μs
T_{delay}=10μs
T_{delay}=15μs
T_{delay}=15μs
T_{delay}=20μs
T_{delay}=20μs

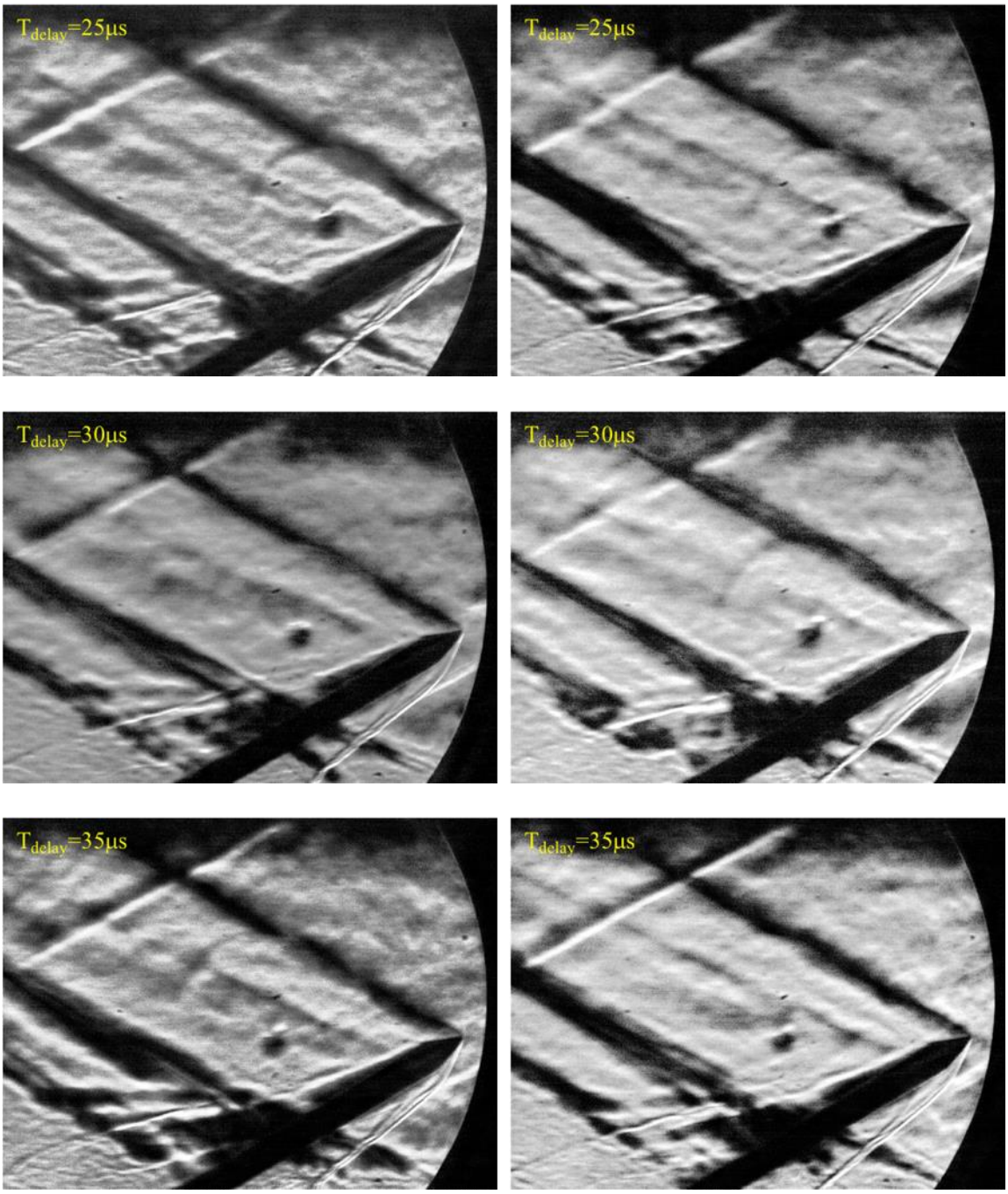
T_{delay}=25μs
T_{delay}=25μs
T_{delay}=30μs
T_{delay}=30μs
T_{delay}=35μs
T_{delay}=35μs

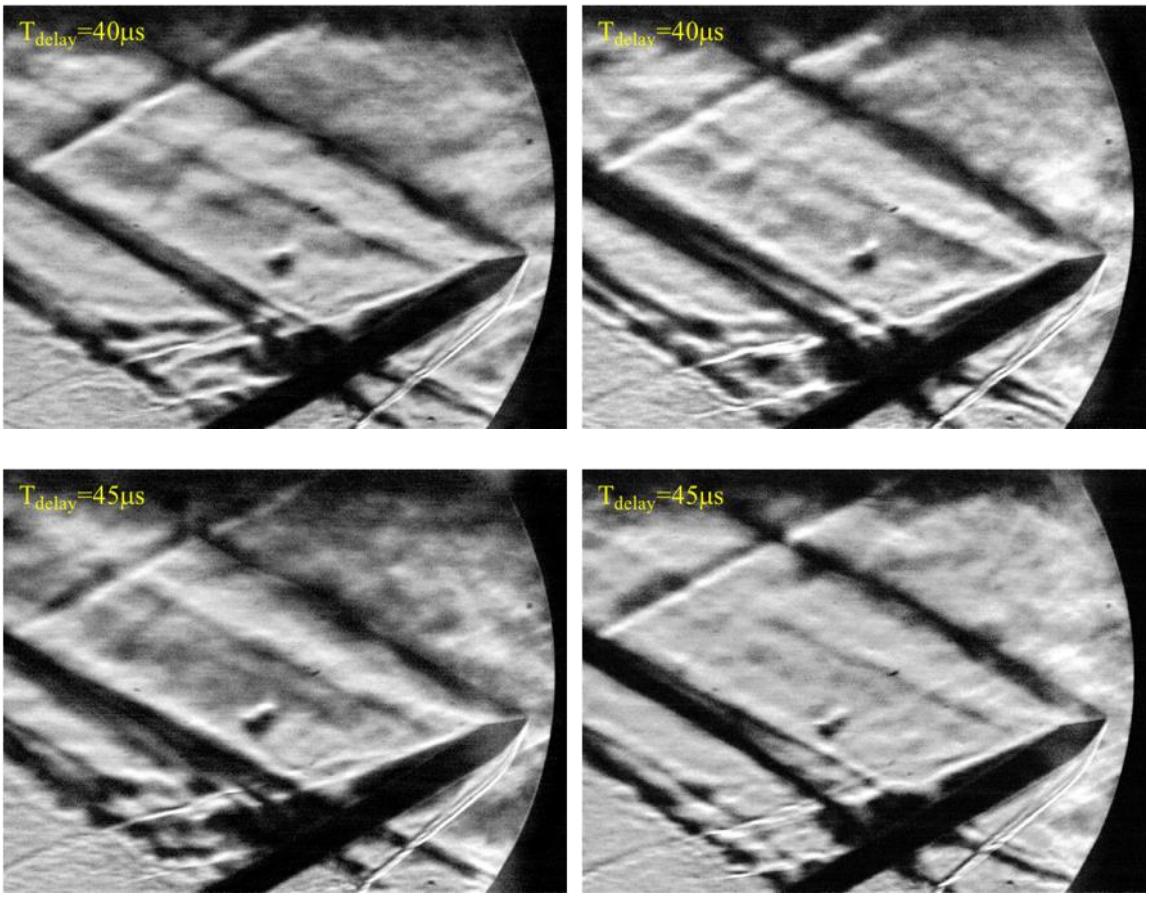

A.2.2. Images for C=1000pF

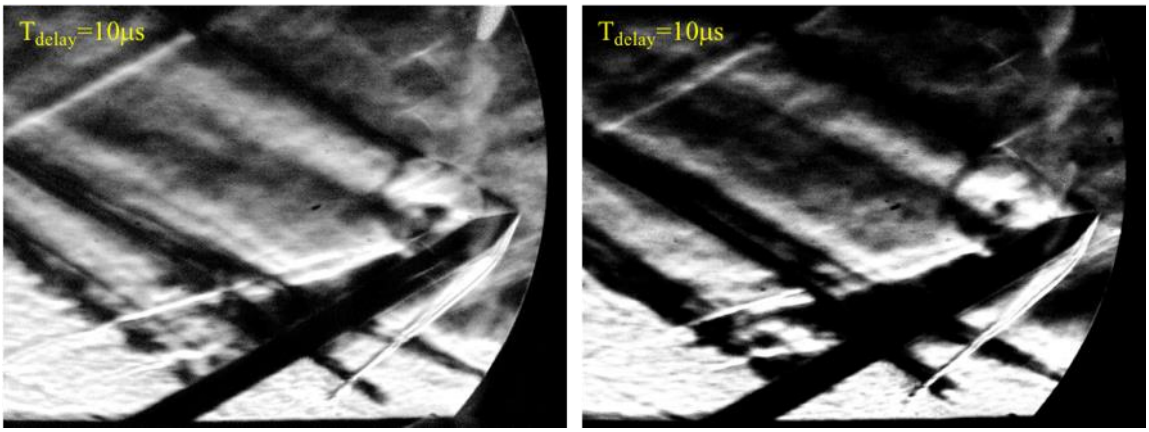

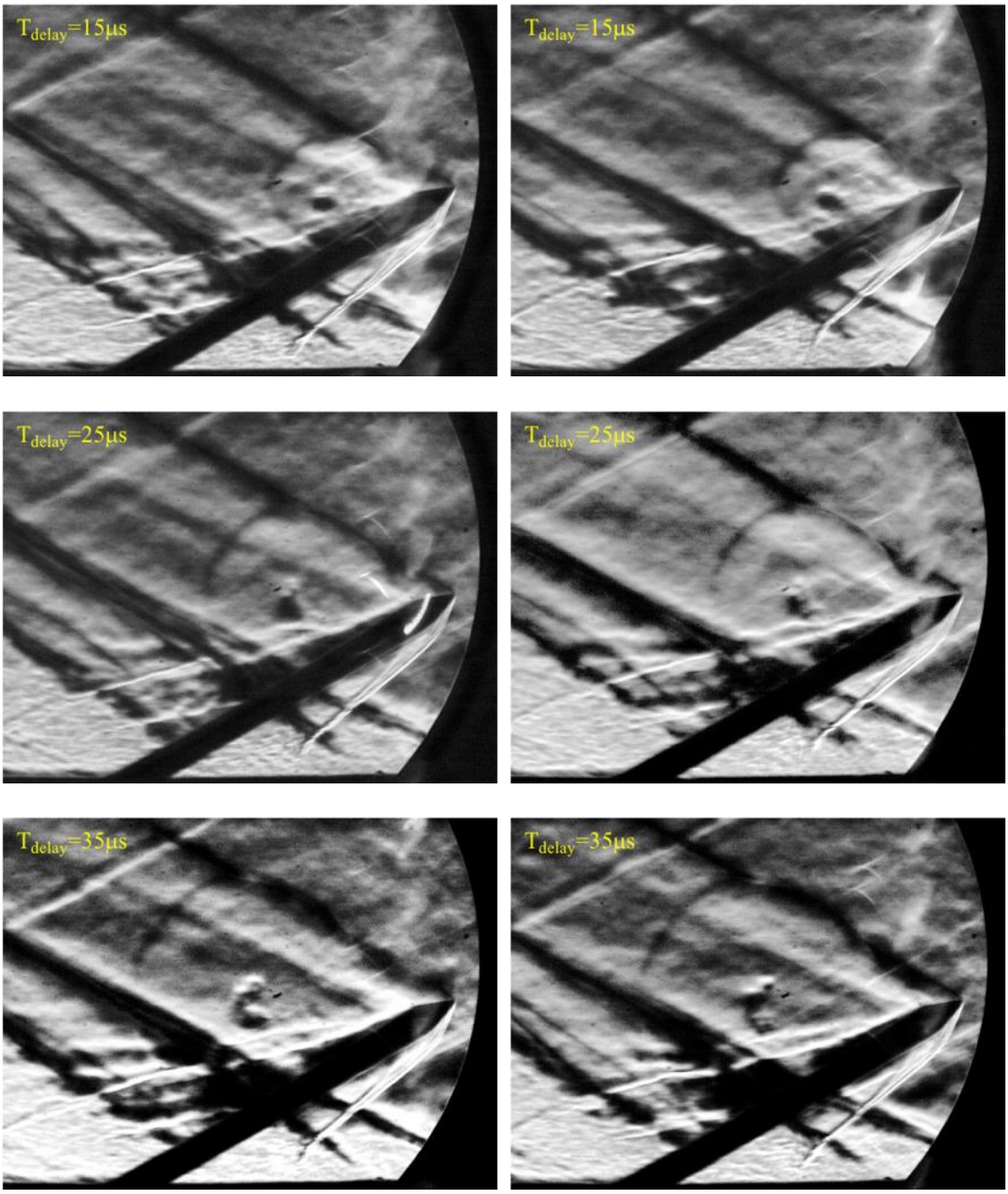

A.2.3. Images for C=10000pF

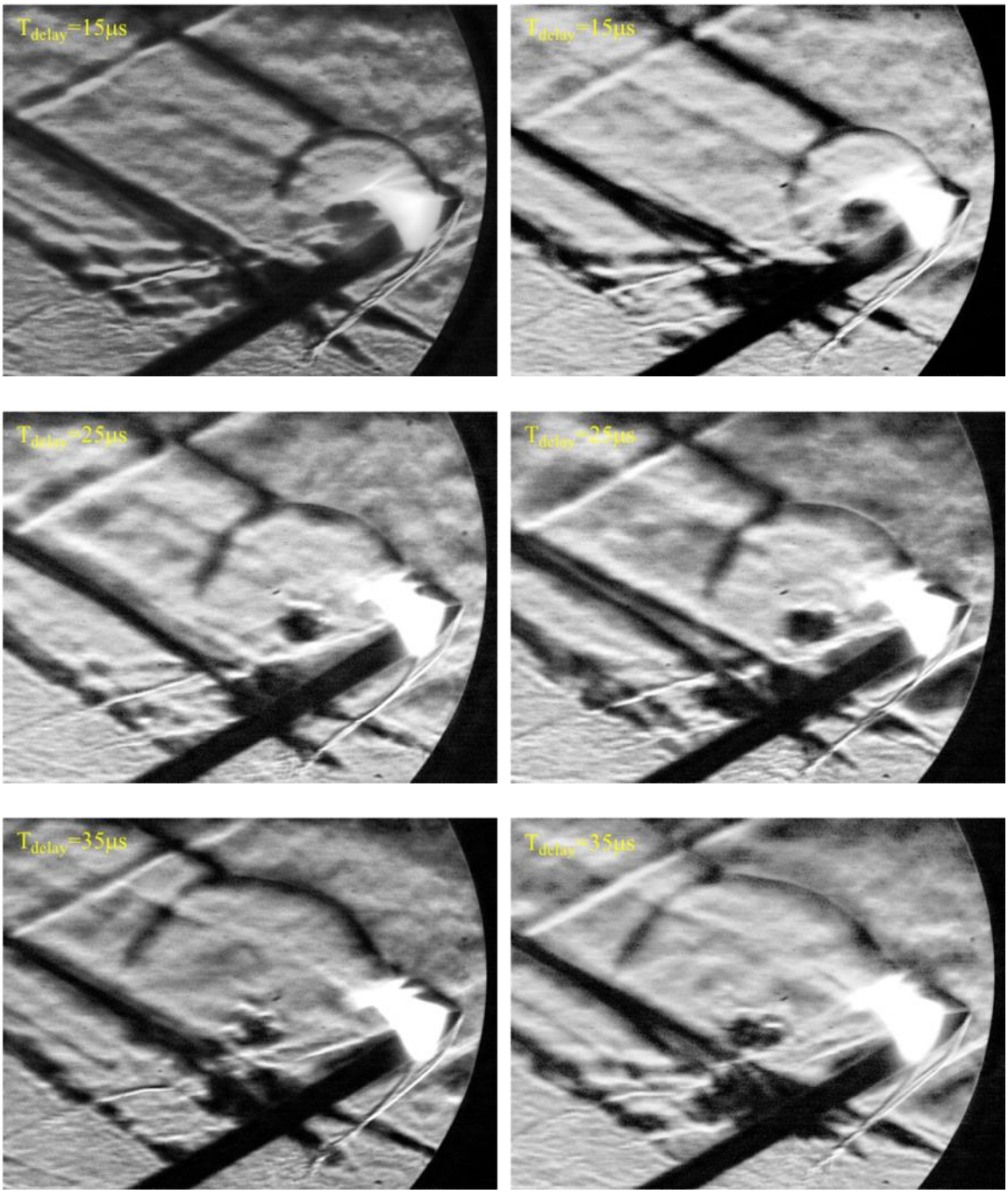
T_{delay}=15μs
T_{delay}=15μs
T_{delay}=25μs
T_{delay}=25μs
T_{delay}=35μs
T_{delay}=35μs